Title
Spark Erosion as a Novel Method of Producing Bimodal Structured 316L Stainless Steel

Author
McElfresh, Cameron

Publication Date
2018

UNIVERSTY OF CALIFORNIA SAN DIEGO

Spark Erosion as a Novel Method of Producing Bimodal Structured 316L Stainless Steel

A Thesis submitted in partial satisfaction of the requirements
for the degree Master of Science

in

NanoEngineering

by

Cameron McElfresh

Committee in charge:

Professor Kenneth Vecchio, Chair
Professor Donald Sirbuly
Professor George Tynan

2018

The Thesis of Cameron McElfresh is approved, and it is acceptable in quality and form for publication on microfilm and electronically:

Chair

University of California San Diego

2018

DEDICATION

For my parents and brothers,

Without your unwavering support, love, council, and curiosity none of this would have been possible.

EPIGRAPH

Any road followed precisely to its end leads precisely nowhere.

Bill Waterson

TABLE OF CONTENTS

Signature Page iii
Dedication iv
Epigraph v
Table of Contents vi
List of Figures viii
List of Tables x
Acknowledgements xi
Abstract of Thesis xiii
Purpose and Structure of Work xv
Part 1 – Application of a Novel New Multispectral Nanoparticle Tracking Technique 1
  1.1 Introduction 1
    1.1.1 Description of New Technology 6
    1.1.2 Theory of Operation 7
    1.1.3 Evolution of m-PTA from Traditional PTA 11
    1.1.4 Operation of m-PTA 13
    1.1.5 Operation of DLS 14
  1.2 Materials and Methods 15
  1.3 Results and Discussion 19
    1.3.1 Monomodal Analysis (Au, PS) 19
    1.3.2 Multimodal Analysis (Au, PS) 23
    1.3.3 Particle Sinking Analysis 25
    1.3.4 Polydisperse 316L Steel 26
  1.4 Conclusion 32
  1.5 Acknowledgements 33
  1.6 References 33
Part 2 – Spark Erosion as a High-throughput Method for Producing Bimodal Nanostructured 316L Stainless Steel Powder 37
  2.1 Introduction 37
  2.2 Materials and Methods 39
    2.2.1 Target Morphology Study 41

2.2.2 Effect of Power Parameters and Liquid Dielectric on Powder Production 41
2.2.3 Powder Characterization 42
2.3 Results and Discussion 45
2.3.1 Effect of Target Morphology on Erosion Rate 45
2.3.2 Effect of Capacitance Settings on Production Rate 46
2.3.3 Powder Microscopy 51
2.3.4 XRD Analysis 54
2.3.5 Dynamic Light Scattering 55
2.3.6 Powder Bimodality Analysis 56
2.3.7 Multispectral Advanced Nanoparticle Tracking Analysis 58
2.3.8 Spark Discharge Modeling 60
2.4 Conclusion 64
2.5 Acknowledgements 65
2.6 References 65
Part 3 – Investigation of Liquid Spark Erosion Nanoparticle Fabrication Using High-Speed Imaging and Emission Spectroscopy 70
3.1 Introduction 70
3.2 Materials and Methods 73
3.2.1 Shock Wave Analysis 74
3.2.2 Spectroscopy-Temperature Analysis 75
3.3 Results and Discussion 77
3.3.1 Shock Wave Analysis Results 77
3.3.2 Spectroscopy-Temperature Results 83
3.3.3 Visualization of Plume 87
3.3.4 Discussion of Variation in Measured Temperature 90
3.3.5 Discussion of Discharge Parameters on Nanoparticle Formation 91
3.4 Conclusion 100
3.5 Acknowledgements 100
3.6 References 101

LIST OF FIGURES

Figure 1.1. Illustration of the basic set up for multispectral particle size analysis 9

Figure 1.2. Raw captured scattering profiles extracted from m-PTA on 800nm particle using (a) blue (450nm) (b) green (520nm) and (c) red (650nm) light 9

Figure 1.3. High-angle annular dark field (HAADF) transmission scanning electron microscopy images of the (a) 250nm, (b) 150nm, and (c) 50nm gold colloid nanoparticles..19

Figure 1.4. DLS and m-PTA size analysis of monomodal gold samples 20

Figure 1.5. DLS and m-PTA size analysis of monomodal polystyrene latex samples 20

Figure 1.6. DLS and m-PTA size analysis of multimodal gold samples..................................22

Figure 1.7. DLS and m-PTA size analysis of multimodal polystyrene samples 23

Figure 1.8. m-PTA measurement of monomodal and bimodal borosilicate particles 26

Figure 1.9. SEM evaluation of spark eroded 316L powder to emphasize spherical and polydisperse particles 27

Figure 1.10. Plots of 316L particle size analysis using DLS and m-PTA at varying capacitance 28

Figure 1.11. Plot of density of particle size distribution versus particle size 30

Figure 1.12. Tracking the non-Brownian motion of a 316L steel particle 32

Figure 2.1. Schematic diagram of the “shaker-pot” spark erosion apparatus............................40

Figure 2.2. Image of the platelet, rectangular, and spherical targets used for spark erosion......41

Figure 2.3. Plot of the spark erosion rate as a function of time for a 60-minute run using different target morphologies...46

Figure 2.4. Plot of the spark erosion rate as a function of time for a 160-minute run at different capacitances 47

Figure 2.5. Plot of spark time, maximum spark voltage, and resultant spark energy with respect to varying capacitance and dielectric 49

Figure 2.6. SEM evaluation of spark eroded target surface...51

Figure 2.7. SEM and HAADF t-SEM evaluation of 316L particles produced by spark erosion 53

Figure 2.8. XRD patterns of commercial powder and spark eroded powder 55

Figure 2.9. Comparative illustration of particle size distribution profiles found by both DLS and MANTA, performed on the same solution of 316L nanoparticles...................56

Figure 2.10. A comparison of the particle size distribution plotted as (a) the relative number fraction and (b) the relative volume fraction to demonstrate the bimodality of the powder..57

Figure 2.11. Plots of 316L spark erosion particle size distributions found with MANTA using varying capacitances and either ethanol or liquid nitrogen 59

Figure 2.12. Simulated radial depth of vaporization for the 316L targets with varying capacitance settings, and (b) the average measured nanoparticle size for 316L spark erosion run at varying capacitances, for either liquid nitrogen or ethanol 63

Figure 3.1. Schematic of high-through shaker-pot spark erosion technique 71

Figure 3.2. 3D illustration of the experimental spark discharge setup with the front plate removed 72

Figure 3.3. Nanoparticle size distributions of 316L particles fabricated by high-throughput spark erosion in (a) ethanol and (b) liquid nitrogen 73

Figure 3.4. Imaging of discharges in ethanol at varied capacitance. Taken at 1000000fps and 500ns exposure 80

Figure 3.5. Imaging of discharges in ethanol at varied capacitance. Taken at 1000000fps and 500ns exposure 81

Figure 3.6. Radial shock wave propagation from discharges in (a) ethanol and (b) liquid nitrogen. Experimental data was fit with the Taylor-Sedov expansion model 82

Figure 3.7. Calculated results of the Rankine-Hugoniot shock front boundary pressure in (a) ethanol and (b) liquid nitrogen 82

Figure 3.8. Typical results of optical emission spectroscopy of discharges in (a) ethanol and (b) liquid nitrogen. Spectroscopy taken with a 10ms integration time. Capacitance was 100μF for these spectra 83

Figure 3.9. Saha-Boltzmann plots of Fe (I) emission species in liquid nitrogen discharges at varied capacitance 84

Figure 3.10. Results of temperature approximations for ethanol and liquid nitrogen discharges at varied capacitance levels 86

Figure 3.11. Imaging of ethanol discharges at varied capacitance levels. Images taken at 1000000fps and 500ns exposure with a 25% neutral density transmission filter 88

Figure 3.12. Imaging of liquid nitrogen discharges at varied capacitance levels. Images taken at 1000000fps and 500ns exposure with a 25% neutral density transmission filter 89

LIST OF TABLES

Table 1.1. List of commonly used particle size analysis techniques for general properties, focusing on methods with applications towards metallic powders and nanopowders ..4

Table 1.2. Summary of the tested samples. Volume percentage indicates the number of particles per unit volume of each size of particle 17

Table 1.3. Summary of data from multimodal particle size analysis...25

Table 1.4. Data extracted from the m-PTA and DLS analysis particle size analysis techniques of the 60μF, 100μF, and 120μF spark eroded nanopowders 29

Table 2.1. Composition of the as received rectangular bar stock and spherical bearing materials prior to spark erosion. Obtained from EDS analysis at 20kV 40

Table 2.2. Composition of the powder products following spark erosion. Obtained from EDS analysis at 20kV 52

Table 3.1. Fe (I) emission peaks used for construction of Saha-Boltzmann plots........................77

ACKNOWLEDGEMENTS

I would like to acknowledge Professor Kenneth Vecchio as my advisor and committee chair. You have been incredibly influential in my development as a scientist and engineer. There are no words that can fully express my gratitude for the time, energy, and expertise you have shared with me over the last few years.

I would also like to acknowledge Tyler Harrington as my mentor and unofficial research advisor. Your guidance, support, and ability to put up with my tireless questioning has been invaluable to helping me reach where I am today. Thank you for always pushing me and never letting me take the easy way out.

I would also like to acknowledge Lucas Brorowski, Olivia Dippo, Kevin Kaufmann, Eduardo Martin, and the rest of the Vecchio Group student researchers who contributed to daily scientific discussion and banter.

I would also like to acknowledge the staff of the NanoEngineering Materials Research Center: Sabine Faulhaber, Steve Horvath, and particularly Wayne Neilson. Your assistance, patience, and continuation as an active resource has been vital to both my research and growth as a scientist.

Part 1, is a modified reprint of material that appears in Measurement Science and Technology, 2018, McElfresh, Cameron; Harrington, Tyler; Vecchio, Kenneth. The thesis author was the primary investigator and author of this material.

Part 2, is a modified reprint of material that appears in Powder Technology, 2018, Harrington, Tyler; McElfresh, Cameron; Vecchio, Kenneth. The thesis author was the primary investigator and author of this material.

Part 3, in part is currently being prepared for submission for publication of the material. McElfresh, Cameron; Mellor, William, Thakur, Saikat; Kaufmann, Kevin; Harrington, Tyler; Elliason, Veronica; Tynan, George; Vecchio, Kenneth. The thesis author was the primary investigator and author of this material.

ABSTRACT OF THE THESIS

Spark Erosion as a Novel Method of Producing Bimodal Structured 316L Stainless Steel

by

Cameron McElfresh

Master of Science in NanoEngineering

University of California San Diego, 2018

Professor Kenneth Vecchio, Chair

The process of spark erosion employs an electric discharge to break down bulk materials into fine powders and has been developed to produce nanostructured powders of metallic, ceramic, and semiconducting materials. This work demonstrates the optimization of charge morphology, energy parameters, and liquid dielectric of a “shaker-pot” spark erosion process to produce maximum yields and size-specific nanopowders. Efforts were taken to evaluate a new multispectral advanced nanoparticle tracking analysis (MANTA) technique that was vital in assessment of the spark erosion-fabricated nanopowders. Additional studies were performed to evaluate the new MANTA technique and its performance capabilities and limitations for application in fast and accurate particle size analysis of complex distributions. Along with the MANTA technique, spark eroded nanopowders were also assessed using x-ray diffraction (XRD), scanning electron microscopy (SEM), transmission scanning electron microscopy (t-SEM), dynamic light scattering (DLS). Material properties and characteristics are discussed with respect to the relevant production mechanisms. A single-spark apparatus was also constructed to evaluate the discharge mechanics relevant to nanoparticle formation. High-speed imaging and spectroscopy were used to investigate the characteristic plasma arc, shock wave, and plume evolution in a submerged capacitive discharge system. The effects of varying both the capacitance and liquid dielectric (liquid nitrogen/ethanol) are evaluated. Discharge features such as plume temperature and time are discussed with respect to previous findings and active particle formation mechanisms that influence size-tunability of the spark erosion technique.

PURPOSE AND STRUCTURE OF WORK

The future of nanotechnology relies on the utilization and development of controllable and versatile nanoparticle synthesis techniques. The purpose of this body of work is to better understand submerged spark erosion technology and its optimization for application as a manufacturing and research tool. Part 1 investigates a new and exciting nanoparticle tracking tool used to accurately evaluate nanoparticle size distributions. Part 2 is application of the spark erosion technique and demonstrates the tunability and reliability of the process. The technique demonstrated in Part 1 is applied in Part 2. Part 3 is an extension of Part 2 and examines characteristic elements of the spark discharge and their relation to relevant particle formation mechanisms. Each of the three parts provide the relevant introduction and background such that they stand as self-contained chapters.

Part 1

Application of a Novel New Multispectral Nanoparticle Tracking Technique

1.1 Introduction

Nanoparticle-based technologies are steadily advancing in areas such as plasmonic biosensing, microstructural engineering, solar cells, strength-enhanced nanocomposites, and a variety of other high-performance applications. The essence of these technologies often relies on unique nanoscale material properties derived from small particle sizes or specific particle size distributions. Quantum confinement, for instance, occurs when at least one physical dimension of a material is equivalent in size, or smaller, than the wavelength of incident photons [1,2]. Quantum confinement can be used to alter the optical and electronic properties of dispersions of particles and is thus becoming widely used in nano-optics and nanoelectronics engineering applications. Size-based phenomenon often rely on precise control over the size and distribution in order for the quantum-based effects to be exploited. Thus, following the development of an ever-increasing number of particle synthesis techniques, the accurate measurement of particle sizes and distributions is becoming increasingly important.

For instance, in microstructural engineering of metals and alloys, it has been well demonstrated that when a multimodal powder distribution is sintered into a bulk material, the resulting grain structure remains with the modal distribution of the starting powder. These multimodal grained materials can offer many unique and desirable attributes such as enhanced strength and high ductility [3,4]. These property enhancements are dependent on the exact distribution of the specific grain sizes within the final bulk material and are even tunable through manipulation of the size distribution. It is therefore useful to engineer the powder with the correct size and distribution of particles prior to sintering into a bulk specimen. Recent efforts at the fabrication of bimodal materials have employed the technique of spark erosion, which can produce a bimodal powder dispersion from bulk pieces of any conductive material [5–7]. The exact size and modal distribution of the particles can vary greatly with the erosion parameters and characterization of the distribution of the powders has been a difficult task [7].

Table 1.1 lists common tools used to analyze particle size distributions and the known limitations of each method. The standard characterization method for particle size analysis remains dynamic light scattering (DLS), and it has been demonstrated that DLS does not provide accurate information regarding complex particle distributions. It is demonstrated here that the application of a multispectral particle tracking technology is effective in characterizing the average size and distribution of complex multimodal particle solutions.

Single particle methods usually include scanning electron microscopy (SEM), transmission electron microscopy (TEM), and nanoparticle tracking analysis (NTA), while ensemble methods typically include dynamic light scattering (DLS), ultra-violet/visible spectroscopy (UV-VIS), X-Ray Diffraction (XRD), and many others [8]. Microscopy-driven single particle counting methods, such as SEM or TEM, offer a much higher spatial resolution than their ensemble counterparts [8]. However, especially when considering bimodal and polydisperse particle size distributions, extracting sufficient data to be statistically robust, through microscopy methods, can be time-consuming, costly, and often impractical [8]. Although techniques such as Tunable Resistive Pulse Sensing (TRPS) offer extremely efficient single particle measurements, they are often only applied in biological and pharmaceutical settings. Ensemble methods can offer a quick, cheap, and high-volume alternative. Differential centrifugal sedimentation has shown to be a reliable and high-resolution technique for analyzing complex particle size distributions across a wide range of sizes.

However, many ensemble scattering techniques do not have the accuracy needed to provide complete descriptions of polydisperse or bimodal samples, and are not capable of measuring particle concentrations. Varying light scattering properties of particles based on size or composition introduces errors in ensemble techniques such as DLS [10, 11, 15]. When the particle diameter is below 10% of the wavelength of the incident light, the source of these errors can be understood through examination of Rayleigh scattering theory, which dictates that the intensity of light scattered is approximately proportional to r^6 – suggesting that in the Rayleigh scattering range, there is a significant bias towards large particles. However, scattering cross-sections of particles with diameters above 10% the wavelength of light are much better predicted using Mie scattering theory [11]. In this study, 670nm light was used for DLS and the majority of the particles analyzed were above 70nm, therefore Mie scattering was assumed and the subsequent equations were used to normalize size-induced scatter effects.

Table 1.1. List of commonly used particle size analysis techniques for general properties, focusing on methods with applications towards metallic powders and nanopowders.

Technique	Ensemble or Single	Resolution (Cost)	Accessible Particle Size Range	Limitations	Real-Time Video Analysis
DLS	Ensemble	10nm (Low)	10nm-1μm	- Inaccurate for polydisperse and bimodal samples - Small particles or trace constituents undetectable in presence of large particles	No
SEM	Single	5nm (High)	5nm-50μm+	- Hard to collect enough data to be statistically reliable - Overlapping particles are often impossible to resolve apart and lead to misrepresentation of large particles - Slow	Yes
TEM	Single	0.2nm (Very High)	0.2nm-200nm	- Hard to collect enough data to be statistically reliable - Slow - Results dependent on competence of operator	Yes
UV-VIS	Ensemble	Dependent on Material (Low)	Dependent on Material	- Unable to accurately resolve polydisperse or bimodal samples - Peak separation/shifts may not provide particle size information - Standard curve often needed for size analysis	No
X-Ray Diffraction	Ensemble	Dependent on Material (Low)	0.5-200nm	- Cannot measure polydisperse or bimodal samples - Can only be used to calculate smallest particle size present	No
Tunable Resistive Pulse Sensing	Single	5nm (Low)	40nm-10μm	- Optimized primarily for biomaterials	No
Differential Centrifugal Sedimentation	Ensemble	5nm (Low)	3nm-50μm	- Dependent on knowledge of solution viscosity and density so is best suited for homogenous samples - Brownian diffusion induces error for small particles	No
PTA	Single	10nm (Low)	10nm-2μm	- Inaccuracies due to varying scattering intensities by different particle sizes - Visualization may include false artifacts - Requires knowledge of sample material	Yes
m-PTA	Single	5nm (Low)	10nm-2μm	- Particles in suspension must be in the proper range of concentrations for accurate results - Requires knowledge of sample material	Yes

As described above, the influence of particle size on light scattering intensity indicates that, when analyzing certain sizes of particles, there is the possibility for the weak scattering signal of small particles (typically 5-50nm) to be overwhelmed by the strong scattering signal of large particles (typically >50nm), ultimately misconstruing the measured particle size distribution [8–10,12,13]. This scattering distortion effect was highlighted in recent work by Mahl *et al*. [14], in which gold and silver nanoparticles of varying sizes were mixed and analyzed via DLS. Upon analysis, the two nanoscale particle size modes were indistinguishable, and a significant portion of small particles went undetected [14]. There are some applications in polydisperse DLS analysis methods that use multi-exponential autocorrelation functions for deconvolution, but there is still limited information given about the particle size distribution profile [8] in such cases. It should be noted that recent applications of DLS analysis at multiple scattering angles have provided more accurate analysis of polydisperse samples, but at present the technique is not widely standardized or applied [13]. Alternatively, XRD is a popular choice for determining crystallite sizes for particles smaller than 200nm. However, the versatility of the FWHM approximation is mainly limited to monodisperse, nanoscale and single-crystal particles. Results from the mathematical crystallite size determination via peak broadening in a laboratory diffractometer are not considered accurate for crystals larger than ~200nm diameter, as the broadening due to crystallite size becomes infinitesimally small when compared to the broadening from other factors including instrumentation. This limits XRD from being a reliable tool to evaluate unknown or polydisperse compositions, since it could induce significant errors. Furthermore, UV-VIS spectroscopy has been an attractive candidate for analyzing suspensions of both organic and inorganic nanoparticles due to the ease of use and versatility [10, 15]. However, it has been found that UV-VIS analysis is much less reliable as the sample becomes more polydisperse due to peak broadening and non-specific peak shifts that cannot be easily correlated with particle sizes [9]. The use of standardized curves for deconvolution of UV-VIS data is a simplified approach to analyzing particle distributions of a known composition. However, the technique is still severely limited in its ability to evaluate solutions of unknown composition or polydispersity. Nanoparticle tracking analysis (NTA) is another analysis technique, which has gained much attention in the recent years, due to the capacity to probe polydisperse and complex particle size distributions [12]. Certain variants of NTA have the ability to provide video feedback of particles in solution, which can give insight to biological and kinetic particle evolution and interaction processes [12]. NTA is a valuable and versatile tool, but is still limited in its analysis of polydispersity, size resolution, and reliability [12, 14]. It has been found that any concentration of small particles (5-50nm) will go undetected due to the high scattering intensity from large particles overwhelming the scattering signal from the small particles [12, 14]. NTA has also been shown to be extremely sensitive to the influence of user settings such as: gain, brightness, blur size, detection threshold, etc., such that resulting particle size distributions may be heavily perturbed by inexperienced users [12, 14]. Among the previously available commercial particle size analysis techniques, there appears to be no singular technique that is fast, accurate, cost-effective, operator independent, and capable of analyzing monomodal, bimodal, and complex particle size distributions.

1.1.1 Description of New Technology

This study focuses on the overview and application of a new technique developed by MANTA Instruments, Inc. that utilizes multispectral illumination and detection for improved nanoparticle tracking and single particle counting for particle size and concentration analysis. As previously discussed, the use of monochromatic light has led to small particle detection failure caused by inherent scattering intensity differences due to particle size. Traditional monochromatic scattering techniques, such as DLS, have resulted in underexposed or undetected small nanoparticles due to the low scattering intensities [10, 11, 14, 15]. Overexposure of large particles and underexposure of small particles leads to erroneous distribution estimations and remains an inherent drawback to monochromatic analysis techniques. With this in mind, the multispectral advanced nanoparticle tracking analysis (MANTA), abbreviated as m-PTA, method used in the commercially avaliable ViewSizer™ 3000 product, intends to offer an alternative approach that enables measurements across a range of particle sizes, improving detection, overall accuracy, and reliability.

1.1.2 Theory of Operation

The following outlines the setup and practical methodology for the MANTA technology, which is illustrated in Figure 1.1 [16]. Light of various wavelengths is emitted from each of three sources (red, green, and blue) and is reflected towards an optical combining component. Thus, three separate light beams are combined into a single multispectral light sheet. The light sheet passes through a polarizer to eliminate horizontal polarization of the light that would not have been scattered in the direction of the detector and as such only contributes unwanted thermal energy to the sample. The light is focused by the objective lens and then sent to probe the sample. Incident light is scattered upon interaction with the particulate sample. Scattered light is captured at approximately 75 to 105 degrees from the incident axis and focused by the long working distance (LWD) objective on a camera sensor. Photons are sorted by wavelengths using a Bayer filter and detected by an extremely sensitive photodetector (charge coupled device – CCD), such that red, green, and blue signal components are simultaneously recorded on different pixels of the CCD. The red, green, and blue components are separated to form grey-scale images representative of the intensity of the recorded signal – portraying the nanoparticles as bright white features (blobs).

Missing pixels, created by the “sorting” of the light due to the Bayer filter, are backfilled with a moving average created from the available values. The spatial evolution of these images over time illustrates the movement of nanoparticles in the solution (Brownian motion). Each particle, at this point, is represented as a ‘spot’ or ‘blurred object’ on each of the red, green, and blue scattering profiles. Image analysis is then performed to evaluate which profile provides the optimal representation of each particle. This process removes false particle features and ensures that the best possible image of each particle is used. To emphasize this point, scattering profiles of the same 800nm diameter particles captured using the m-PTA technique are illustrated in Figure 1.2 [16]. The blue (450nm) and green (520nm) wavelengths both produce noisy and misshapen images, while the red (650nm) light clearly produces the best, unperturbed image of the nanoparticle. In this case, digital image evaluation by the software would optimize the particle tracking mechanism by selecting the 650nm wavelength to represent this particle.

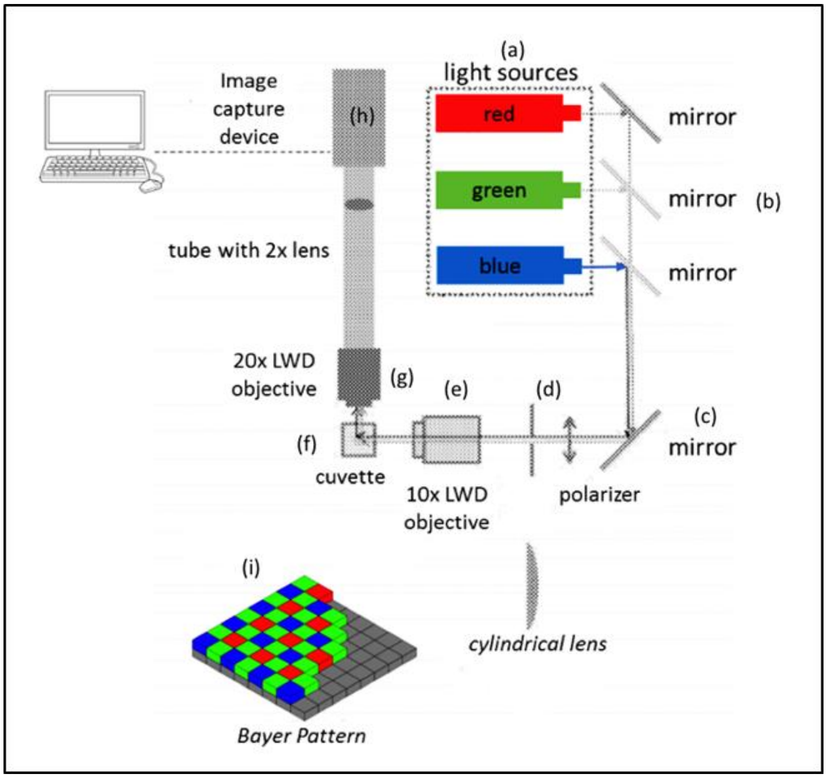

Figure 1.1. Illustration of the basic set up for multispectral particle size analysis that requires: (a) 3 individual light sources, each with power level adjustment, (b) recombining mirrors to create a single light sheet, (c) mirror, (d) horizontal polarizer, (e) objective lens, (f) sample cuvette, (g) objective lens and Bayer pattern filter, (h) highly sensitive image capturing device, and (i) Bayer pattern.

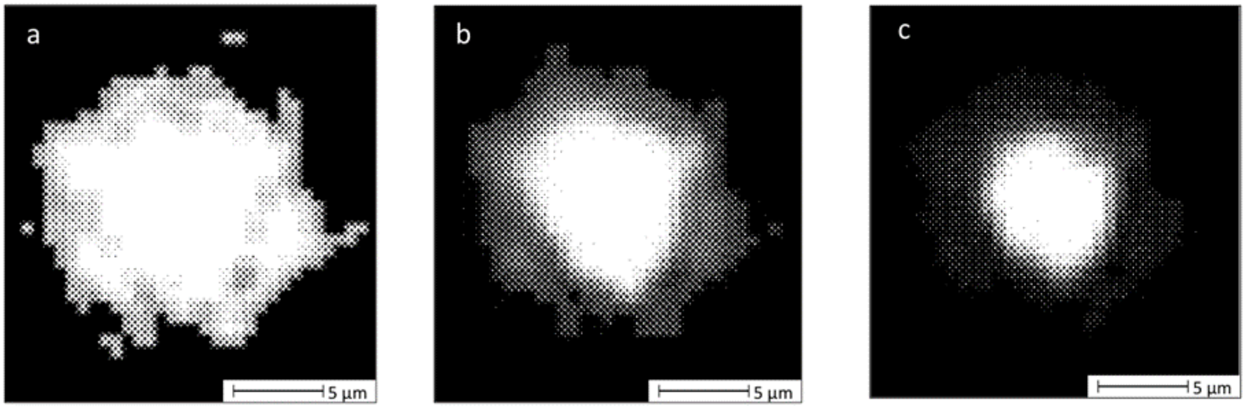

Figure 1.2. Raw captured scattering profiles extracted from m-PTA on 800nm particle using (a) blue (450nm) (b) green (520nm) and (c) red (650nm) light. Note how the particle representation appears to be optimized with the red light profile.

ViewSizer™ software is used to facilitate particle tracking analysis of recorded videos frame-by-frame with a modified form of the "*Particle Pretracking and Tracking, and 2D Feature Finding*" algorithm developed by *Maria L. Kilfoil*; more information about this tracking algorithm and recent applications can be found in references [18, 19]. The software allows for refinement of the computational tracking process and includes the removal of particle drift on a particle-by-particle basis, intensity and size thresholding, and false features detection. The theory of nanoparticle tracking analysis is well known and based on the Brownian motion exhibited by small particles from random collisions with surrounding water molecules. If particle positions x_i and y_i are recorded on a 2D x-y plane for N steps, the mean-squared displacement can be calculated with respect to $n = 1, 2, \ldots, N-1$ as given by Equation (1):

$$MSD(n) = \frac{1}{\mathrm{N-n}} \sum_{i=1}^{N-n} (x_{i+n} - x_i)^2 + (y_{i+n} - y_i)^2 \tag{1}$$

Using the time delay between frames Δt, the two-dimensional diffusion coefficient D can be fitted by Equation (2):

$$MSD(n) = (4\Delta tD)n \tag{2}$$

The *Einstein-Langevin* expression then provides a simple formula for finding hydrodynamic particle diameter, d, as expressed in Equation (3):

$$d = \frac{k_B T}{3\pi\eta D} \tag{3}$$

Here T is absolute temperature, k_B is the Boltzmann constant, and η is the dynamic viscosity of the solvent.

1.1.3 Evolution of m-PTA from Traditional PTA

Particle tracking analysis (PTA) has become a popular and reliable technique for evaluating particle size distributions and absolute concentration in both organic and inorganic suspensions [12,18–25]. Fast, cheap, non-destructive, and accurate analysis of suspensions has made PTA ideal for applications in biology, food testing, sedimentation evaluation, and nanoparticle analysis. The non-destructive nature of PTA and the ability to continually reevaluate particle size distributions has also enabled it to capture time-dependent kinetic evolutions such as aggregation [23]. Popularity of PTA has in part been due to its single particle counting mechanism that is less subject to scattering overexpression of large particles that may skew DLS analysis [22–25]. However, because PTA is dependent on small-particle scattering events from a single wavelength of incident light, it is also prone to scattering induced errors from polydisperse samples [18–21,26]. To increase versatility, many PTA systems have been equipped with multiple light sources to select from or employ a single tunable light source. In addition, PTA is now typically equipped with auto-optimization capabilities that probe the suspension to select ideal measurement parameters. These adjustments have made PTA operation more accessible and accurate for ideal analysis of weakly disperse systems, but have not solved the issue of scattering-induced error in highly polydisperse systems. Filipe *et al.* [26] found that sub 100nm polymer and protein samples were under-expressed in solution with larger constituents. A recent study by Tian *et al.* [21] demonstrated that 100nm polystyrene beads were hardly detectable in the presence of an equal volume of 300nm polystyrene beads. Additional studies that found similar overexpression errors in PTA are provided in the references [18–20,27].

Since PTA relies on scattering profiles from individual particles to track their Brownian motion, it is paramount that these profiles are accurate. However, scattering power differs greatly for particles on the 1-2000nm scale – indicating that probing a polydisperse system with one wavelength of light will inherently induce bias to the measurement correlating to the scattering ability of the particles in question. Selecting a long wavelength (~650nm) red light source may be ideal for profiles of larger particles, but small (<60nm) particles may be undetectable due to weak scattering of red light. Conversely, selecting a short wavelength (~450nm) blue light source may be ideal for illuminating small particles in solution, but profiles of larger particles would be oversaturated and overexpressed – ultimately limiting the resolution of size determination. Figure 1.2(a) illustrates the latter example of a poor quality scattering profile for a large particle due to low wavelength light selection.

The m-PTA technique attempts to overcome this natural shortfall of PTA by adding the simultaneous multispectral illumination and analysis component. By simultaneously probing the sample with three different wavelengths of light each particle creates three different scattering profiles, which are individually captured through the Bayer filter, as is shown illustrated in Figure 1.2(a-c). One of the scattering profiles will likely hold the sharpest and least saturated image of the particle, as in Figure 1.2(c) for the earlier example, and computational evaluation parameters will select the scattering profile created by that wavelength of light to represent that individual particle. Due to this, it is possible that m-PTA may be less subject to size-induced scattering errors because large particles will be represented by long wavelength scattering profiles, while small particles will be simultaneously represented by short wavelength scattering profiles. In addition, m-PTA technology in the ViewSizer™ 3000 also has the ability to image in the vertical direction permitting sedimentation size analysis. The physics of sinking spherical particles in solution is well understood and can be expressed using Stokes equation as in Equation (4):

$$d = \sqrt{\frac{18v\eta}{g(\rho - \rho_0)}} \tag{4}$$

Here, v is the velocity of the particle, g the gravitational constant, ρ is the density of the particle, ρ_0 is the density of the solution, and η is the dynamic viscosity of the solution.

1.1.4 Operation of m-PTA

The m-PTA technique is performed as follows: a powdered or otherwise pure sample is suspended in a cuvette filled with pure liquid diluent (0.3 mL minimum) of known viscosity. The ideal concentration to optimize the number of particles counted per video, while also limiting the number of overlapping particle trajectories, is approximately $5\text{x}10^7$ particles/mL. However, accurate analysis can be performed on concentrations in the range of $4\text{x}10^6$ to $2\text{x}10^8$ particles/mL. If the concentration of the solution is unknown or unattainable, m-PTA can provide an estimate by analyzing the suspension. Once the correct dilution is attained, and the cuvette containing the sample has been placed in the chamber, real-time video feedback of the particles in solution is displayed by the ViewSizer™ software. The image must be focused to its ideal position, and afterwards the user can define the desired laser power (with respect to each laser), frame rate, exposure, video length (in frames), the number of videos, as well as other parameters, which can be tuned if needed for the specific application. The complete set of parameters is logged and recorded in a file and can be easily accessed for use with similar samples in the future. A typical analysis takes less than 10 minutes to record 25 videos for tracking 4000 or more particles, depending on the concentration. Longer tests can be run to collect more statistically robust data. Upon completion, the software provides all particle size and concentration data presented in a variety of binned formats. Additionally, all videos recorded during the experiment are available to observe dynamic events such as non-Brownian movement of larger particles (sinking), agglomeration, dissolution, and growth.

1.1.5 Operation of DLS

Dynamic light scattering was conducted on a ZetaPlus Particle Sizer (Brookhaven Instruments Corporation, USA). Incident light is scattered from particles in solution to a detector and the resulting signal intensity is captured. As particles experience Brownian motion, the captured signal fluctuates relative to their mobility in suspension. The fluctuating signal for monodisperse suspensions is processed through the autocorrelation function given by Equation (5):

$$C(t) = Ae^{-2\Gamma t} + B \tag{5}$$

In this relation *C(t)* is the autocorrelation function, *A* is an optical constant from instrumental design, *t* is the time delay, *B* is a constant background term, and Γ corresponds to the relaxation of the fluctuations written as Equation (6):

$$\Gamma = Dq^2 \tag{6}$$

Here *D* is the diffusion coefficient as previously described. The parameter *q* then relates these quantities in Equation (7) using the wavelength of incident light (λ_0), the index of refraction (*n*) of the suspending liquid, and the scattering angle θ :

$$q = \frac{2\pi n}{\lambda_0} 2\sin(\frac{\theta}{2}) \tag{7}$$

For solutions with a more broad distribution of sizes, Equation (7) must be modified. Since each individually sized particle contributes its own exponential, the expression changes to Equation (8):

$$g(t) = \int G(\Gamma) e^{-\Gamma t} d\Gamma \tag{8}$$

In this expression *g(t)* is the captured data, the background term *B* has already been subtracted, and the square root of the remainder was taken. The solution to this Laplace transform is nontrivial and a method of cumulants is utilized.

1.2 Methods and Materials

The initial evaluation of the m-PTA technique was performed on monodisperse samples of gold nanoparticles (Ted Pella, Inc.) and monodisperse samples of polystyrene latex nanoparticles (Ted Pella, Inc.). Accuracy of peak locations and relative intensities provide insight to the sensitivity and versatility of the technique in detecting specific particle size presence and relative concentration. Monomodal and bimodal solutions of gold (Au) and polystyrene latex (PS) nanoparticles were prepared in volume ratios as listed in Table 1.2. Dilutions were in the range of 5.7×10^6 – 5.0×10^7 particles/mL of solution. Solutions were prepared with Xzero Type-1 reference water (XZERO, Sweden) and thoroughly vortexed prior to analysis. m-PTA was performed with 30 videos per trial, with automated stirring between each video to minimize double counting of particles. Measurement was conducted with laser powers of 210mW, 12mW, and 8mW for the 450nm, 520nm, and 650nm light sources, respectively. Dynamic light scattering was also performed under the same conditions. DLS was conducted on a ZetaPlus Particle Sizer (Brookhaven Instruments Corporation, USA) using 90Plus Particles Sizing Software Version 4.20. Experiments were performed with a 90 degree collection angle using 670nm light and 10 trials of 1 minute each. To directly compare the m-PTA and DLS results, all DLS intensity data in this study was converted to relative number intensity form through BHMIE analysis [28]. TSEM at 30kV was performed on the gold solutions for particle size confirmation. All TSEM and SEM in this study was performed on an FEI Apreo scanning electron microscope with transmission SEM (TSEM) capability.

Additionally, the technique is evaluated using a polydisperse 316L steel nanopowder. The measurement of the 316L nanopowder is aimed to gauge the ability of the m-PTA technique in assessing a broad size distribution with a single mode.

Sinking detection capabilites of the MANTA ViewSizer™ 3000 were tested on solutions of 2000nm and 8300nm borosilicate (BS) glass particles (Thermo Scientific, USA). Mixtures were preapred in Xzero Type-1 reference water as described in Table 1.2. Density of commercial borosilicate partiles was 2.55g/cm^3. m-PTA was performed with 12mW 650nm light.

Table 1.2. Summary of the tested samples. Volume percentage indicates the number of particles per unit volume of each size of particle.

	Volume Composition [%]							
Sample	50nm Au	150nm Au	250nm Au	80nm PS	173nm PS	262nm PS	1900nm BS	8300nm BS
1	100	--	--	--	--	--	--	--
2	--	100	--	--	--	--	--	--
3	--	--	100	--	--	--	--	--
4	30	70	--	--	--	--	--	--
5	55	--	45	--	--	--	--	--
6	35	40	25	--	--	--	--	--
7	--	--	--	100	--	--	--	--
8	--	--	--	--	100	--	--	--
9	--	--	--	--	--	100	--	--
10	--	--	--	45	55	--	--	--
11	--	--	--	40	35	25	--	--
12	--	--	--	--	--	--	100	--
13	--	--	--	--	--	--	--	100
14	--	--	--	--	--	--	33	67

To assess the performance of the m-PTA method on wide distribution, non-standard samples, tests were run with a polydisperse 316L steel nanopowder produced by the spark erosion method. The powder of interest was synthesized via shaker pot spark-erosion, a process developed in 1998 by *Berkowitz et al.* [29–31], which has proven successful as a high-throughput method of producing spherical, ultrafine, polydisperse powders. An electric discharge cell, completely submerged in a liquid dielectric, shakes until there is a finite gap between charges, which can facilitate a dielectric breakdown, at which point a high-temperature plasma arc is created. Large portions of material on the surface of the arc liquefy, and the liquid is ejected and immediately quenched in the dielectric – resulting in spherical particles on the order of 3µm and above. Meanwhile, areas of the charge in the highest temperature of the arc are vaporized and subsequently condensed – resulting in particle diameters smaller than 1µm. Temperatures in the arc can reach over 10,000K, and thus the liquid dielectric is vaporized in the area local to the spark, creating a gaseous pocket around the plasma channel, which mediates the different stages of nanoparticle formation [21, 22]. Much like electrical discharge machining (EDM), spark and powder production qualities can be dictated by the parameters of the spark erosion apparatus. Higher energy sparks leads to deepened non-uniform surface heating, which should subsequently lead to larger ejected particles with an increasingly polydisperse size distribution [32]. To further assess the detection limits of m-PTA, powder was collected from spark erosion trials run at low (60µF), moderate (100µF), and high capacitance (120µF) levels.

All solutions were ultra-sonically stirred to minimize agglomerated particles. Dilutions were allowed to settle before sampling from the top – to avoid a high population of oversized (>1 µm) particles. Powder dilutions were prepared and analyzed in XZERO reference water under the same parameters as the gold solutions. All trials were of pure powder without combinations. SEM and TSEM confirmation of powders polydispersity was performed. Dynamic light scattering was also performed under the same conditions.

1.3 Results and Discussion

1.3.1 Monomodal Analysis (Au,PS)

TSEM analysis of the as-received gold colloids is featured in Figure 1.3. Individual particles were counted and measured to be an average of 50.2±3nm, 151.6±3.6nm, and 253.5±8.5nm for the 50nm, 150nm, and 250nm samples, respectively. All samples were observed to be monodisperse. The results of monomodal gold particle size analysis for both DLS and m-PTA are shown in Figure 1.4. All m-PTA data has been normalized in terms of relative count intensity to be comparable to the DLS data. The DLS mode-average was found to be 52.2nm, 151.4nm, and 255.7nm for samples 1, 2, and 3, respectively. m-PTA detected mode-averages at 54.3nm, 162.2nm, and 271.2nm, for samples 1, 2, and 3, respectively.

Results of monomodal polystyrene latex particle size analysis for both DLS and m-PTA are presented in Figure 1.5. DLS measurement resulted in mode-averages of 80.1nm, 174.3nm, and 263.2nm for samples 7, 8, and 9, respectively. m-PTA detected mode-averages at 84.5nm, 178nm, and 263.5nm, for samples 7, 8, and 9, respectively.

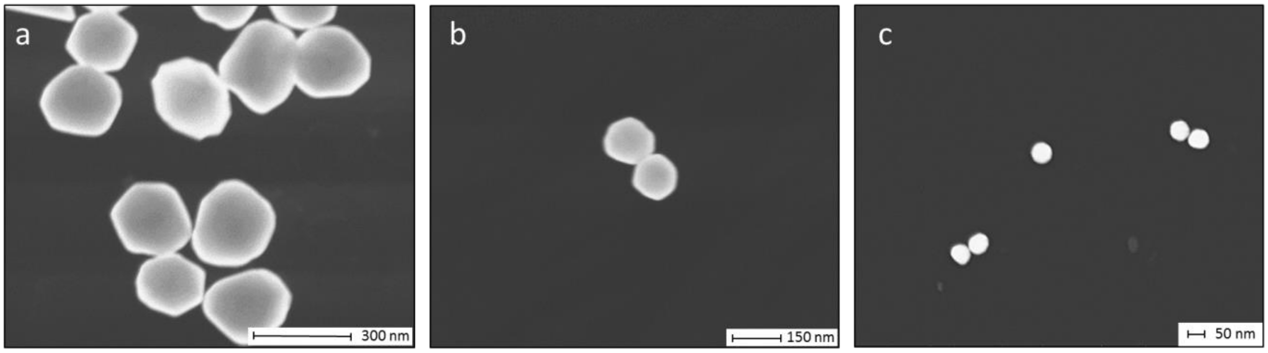

Figure 1.3. High-angle annular dark field (HAADF) transmission scanning electron microscopy images of the (a) 250nm, (b) 150nm, and (c) 50nm gold colloid nanoparticles.

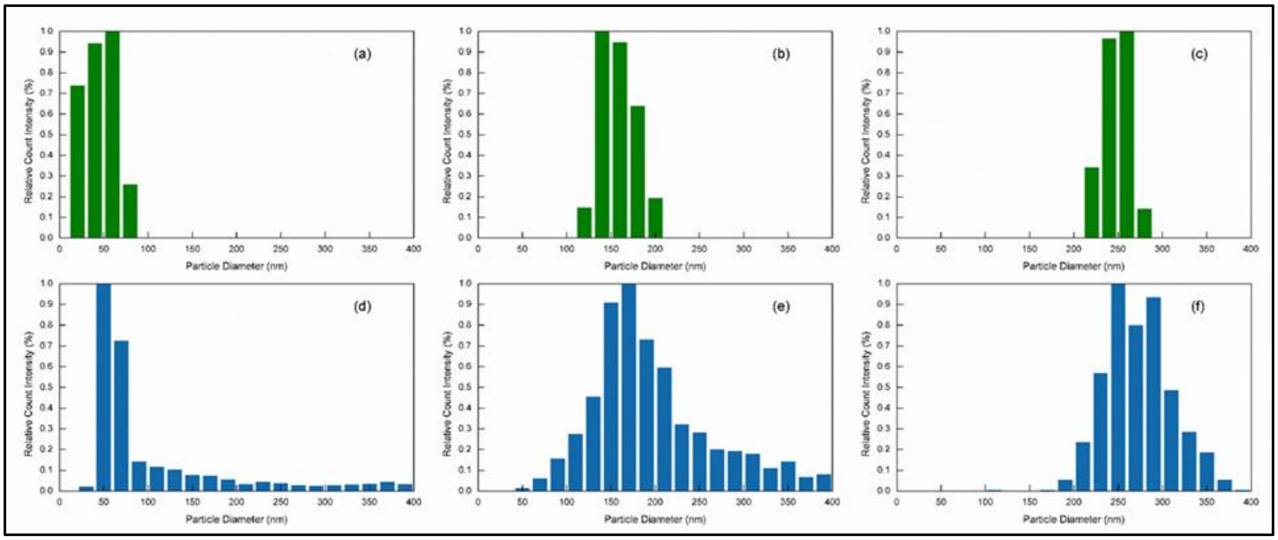

Figure 1.4. DLS (green) and m-PTA (blue) size analysis performed on the monomodal gold samples. DLS particle size distributions of the (a) 50nm, (b) 150nm, and (c) 250nm gold nanoparticles. m-PTA of the same (d) 50nm, (e) 150nm, and (f) 250nm monomodal gold solutions.

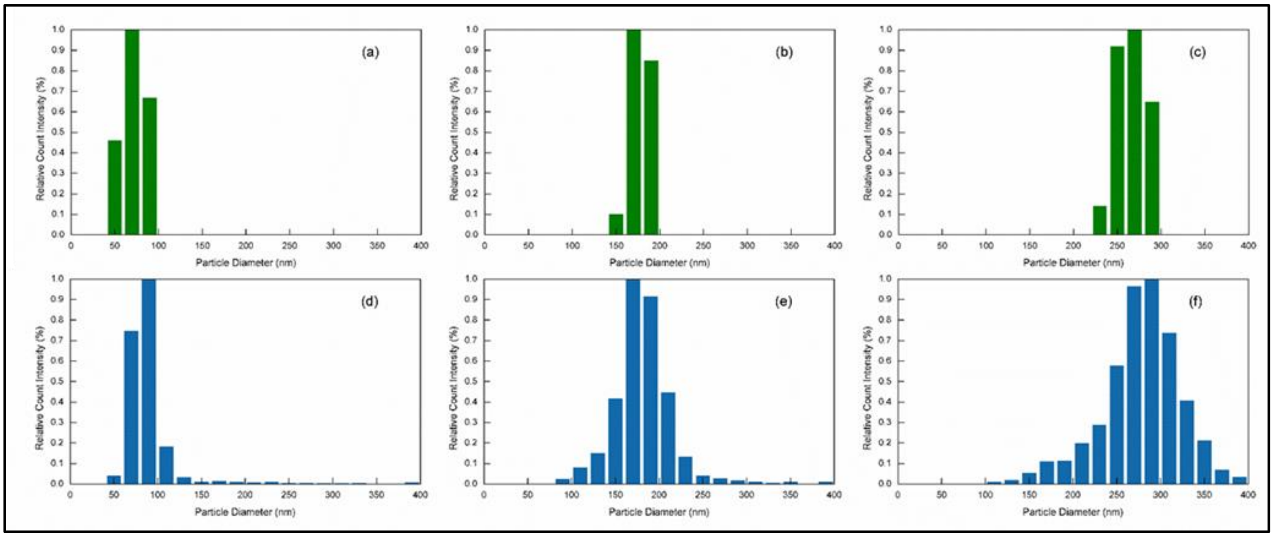

Figure 1.5. DLS (green) and m-PTA (blue) size analysis performed on the monomodal polystyrene latex samples. DLS particle size distributions of the (a) 80nm, (b) 173nm, and (c) 262nm PS nanoparticles. m-PTA of the same (d) 80nm, (e) 173nm, and (f) 262nm monomodal PS solutions.

The monomodal particle size detection capabilities of DLS and m-PTA performed similarly for the evaluation of both the monomodal gold and monomodal polystyrene. Both DLS and m-PTA use the speed of spherical particle diffusion in solution to find the corresponding theoretical hydrodynamic diameters of the nanoparticles present. It is important to note the difference between hydrodynamic radius and the true radius of the metallic core because various factors can influence the speed of particles in solution and therefore alter the measured particle size. Any form of surface monolayer, contaminant surface adsorption, or the electrical double layer, which is dictated by the colloid material and substances present in the solvent, can slow particle speed and thereby increase measured hydrodynamic radius. To further complicate matters, chemically-based nanoparticle synthesis techniques often rely on precursor materials and capping or stabilizing agents that are extremely difficult to separate from the formed particles - resulting in solutions with unwanted leftover materials. Consequentially, the particle size measured in the monomodal solutions is often larger than the microscopically measured particle size. This does not diminish the significance of measuring the hydrodynamic radius, per say, but rather it indicates that one must take careful consideration of the particle’s composition and environment when there is a difference in particle size from different measurement techniques.

It must also be noted that m-PTA analysis performed on the 50nm and 150nm monomodal Au samples and 80nm and 173nm latex samples found low counts of particles with sizes significantly larger (>200nm) than the expected peak. These populations are likely nanoparticles that have formed agglomerates with other nanoparticles or substances in the solution. The intrinsically high surface area to volume ratio of nanoparticles typically leads to colloids with high surface energy that are instable and reactive compared to their bulk counterparts. To minimize increases in surface energy, colloid nanoparticles often flocculate in solution regardless of the use of reagents that are designed to prevent this. It is sensible, then, that the effects of particle flocculation are less prominent in the monomodal 250nm Au and 262nm PS solutions because the surface area to volume (surface energy) relation for a sphere is driven by a 1/r relationship. DLS was unable to observe the low concentrations of these larger particles/agglomerates. m-PTA measurement of the 150nm gold and 262nm polystyrene solutions also detected low counts of particles considerably smaller (<100nm) than the expected peak. These populations of particles are likely due to natural size deviation occurring during nanoparticle synthesis, but may also include surfactants or capping agents that were not removed through purification or by the detection software. DLS did not detect the low concentrations of smaller particles, which may have been in part due to signal intensity screening by the larger particles. The ability of the m-PTA technique to measure trace concentrations is evidently one of its strengths, however, it does suggest that distribution analysis must be carefully examined to discern meaningful results from foreign objects or contamination.

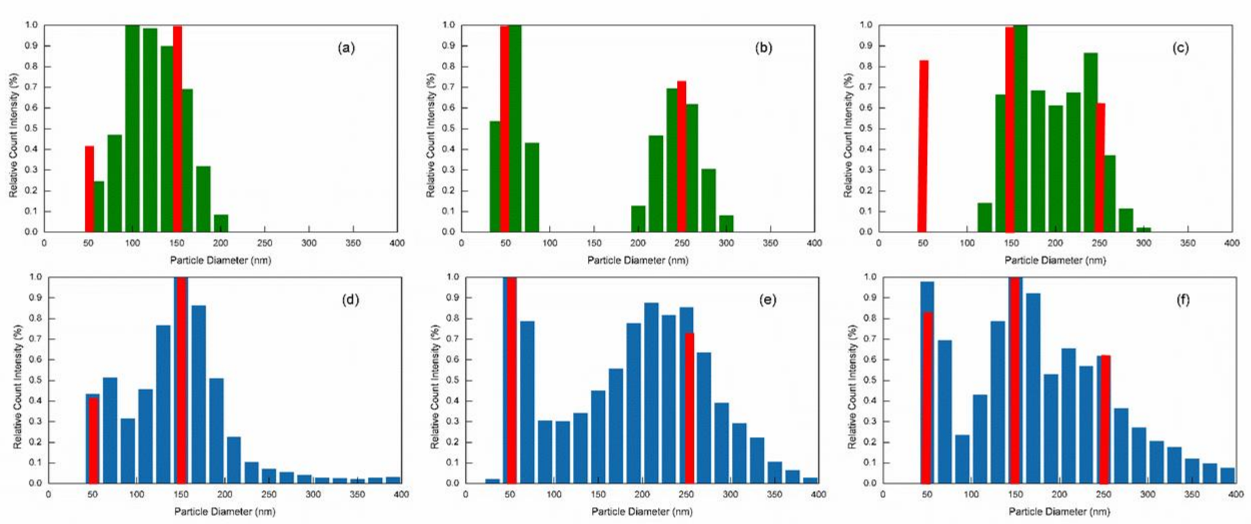

Figure 1.6. DLS (green) and m-PTA (blue) size analysis performed on the multimodal gold samples. DLS particle size distributions of the (a) sample 4, (b) sample 5, and (c) sample 6 gold nanoparticles. m-PTA size analysis of the same (d) sample 4, (e) sample 5, and (f) sample 6 multimodal gold solutions. The red bars on the histogram represent the expected relative intensities of the respective 50nm, 150nm, and 250nm peaks.

1.3.2 Multimodal Analysis (Au, PS)

The results of multimodal particle size analysis for gold and polystyrene samples are shown in Figure 1.6 and Figure 1.7, respectively. Analysis of the multimodal particle size distributions is summarized in Table 1.3. The detected volume percentage compositions were calculated using the ratios of peaks from the corresponding DLS and m-PTA particle size distributions. The multimodal particle size combinations were chosen in order to test the sensitivity of either technique in correctly identifying the peak positions and peak ratios in complex mixtures.

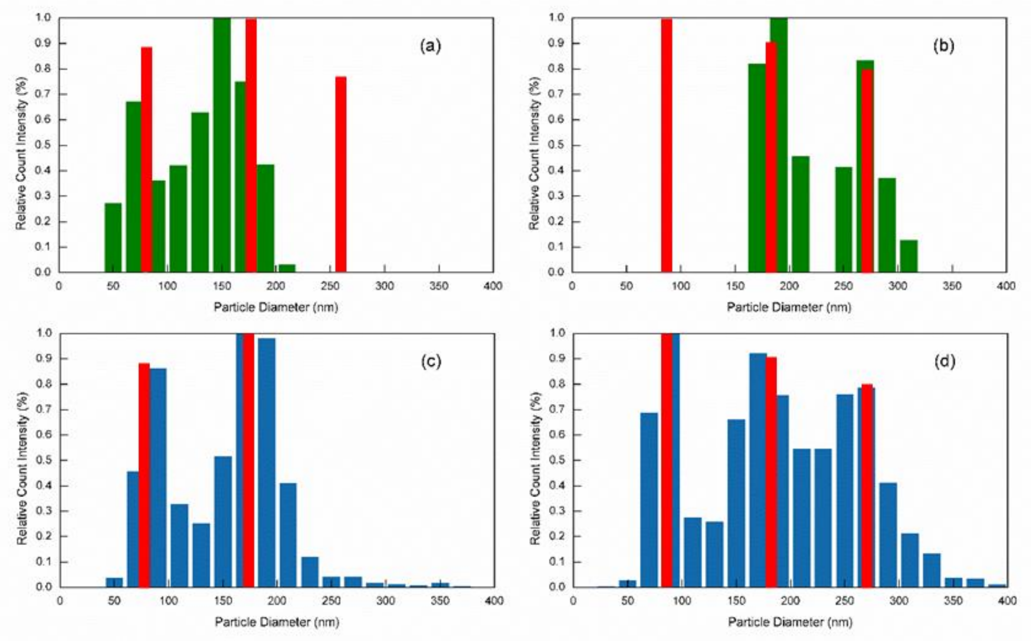

Figure 1.7. DLS (green) and m-PTA (blue) size analysis performed on the multimodal polystyrene samples. DLS particle size distributions of the (a) sample 10 and (b) sample 11 latex nanoparticles. m-PTA size analysis of the same (c) sample 10 and (d) sample 11 solutions. The red bars on the histogram represent the expected relative intensities of the respective 80nm, 173nm, and 262nm peaks.

Analysis of complex solutions with particles across a range of sizes has been shown to be difficult with DLS due to variable influence of particle size on light scattering intensity – resulting in many of the smaller particles being concealed or expressed at a diminished level. It can be seen that these size effects played a large role in DLS measurements of the trimodal gold sample 6, where the 50nm peak disappears completely due to the increased signal from the 150nm and

250nm particles, despite consisting of 35% volume of the mixture. DLS measurement of trimodal polystyrene sample 10 illustrates the same type of error in concealment of the 40% volume 80nm particles likely owed to the presence of 172nm and 262nm particles.

A similar error occurs in DLS measurement of gold sample 4, which results in the bimodal particle size distribution wrongly reducing to a single peak centered at 105nm. While it is possible that a 50nm peak is contained in the left tail of the particle size distribution, it could not be observed due to limited separation. DLS analysis of bimodal polystyrene sample 10 successfully discerned the individual 80nm and 173nm peaks, but resulted in a 12.5% under-expression of the smaller particles.

m-PTA characterization was largely unaffected by the presence of multiple modes of particle sizes. All peaks in both the bimodal and trimodal distributions were identified correctly despite overlapping data in the tails of the individual modes, which can be observed in Figure 1.4(d-f) and Figure 1.5(d-f). Additionally, the m-PTA technique was significantly more successful in evaluating the correct peak ratios and, therefore, sample volumetric particle concentration. Characterization of sample 5 detected the correct relative particle concentrations within 2% of the expected concentration regardless of the significant volume of large (250nm) particles present in the bimodal distribution. m-PTA measurement of polystyrene sample 11, in particular, exhibited the multimodal detection capabilities of the technique. All three peaks were identified with ample separation despite inherently overlapping distributions, and the relative concentrations were correctly identified within a 4% error of the expected values for all three constituents of the mixture.

Table 1.3. Summary of data from multimodal particle size analysis.

	Number Of Peaks			Volume Percentage Composition [% Vol. 50nm Au , % Vol. 150nm Au : % Vol. 250nm Au] [% Vol. 80nm PS , % Vol. 173nm PS : % Vol. 262nm PS] [% Vol. 2 μm BS: % Vol. 8μm BS]		
Sample	Expected	m-PTA Detected	DLS Detected	Expected	m-PTA Detected	DLS Detected
4	2	2	1	30, 70, 0	34, 66, 0	0, 100, 0
5	2	2	2	55, 0, 45	53, 0, 47	17, 0, 83
6	3	3	1	35, 40, 25	37, 38, 24	0, 0, 100
10	2	2	2	44, 55, 0	46, 53, 0	40, 60, 0
11	3	3	2	40, 35, 25	40, 34, 26	45, 55, 0

1.3.3 Particle Sinking Analysis

Results from sinking particle size analysis on monomodal borosilicate are presented in Figure 1.8(a,b). m-PTA measurement detected mode-averages of 1850nm and 8330nm for monomodal samples 12 and 13. The mode-average size of the larger 8300nm sample was within 1% of the expected value, while measurement of the smaller 2000nm sample resulted in a mode-average roughly 8% lower than the expected value. It is possible that this discrepancy is due to the increasing influence of Brownian motion relative to gravitational forces as particle size decreases. A relative increase in Brownian motion may limit the accuracy of measurement for smaller (~2000nm) particles because random directional fluctuations could inhibit reliable determination of vertical gravitational movement. Results from m-PTA sinking analysis of the bimodal borosilicate solutions are featured in Figure 1.8(c). The relative concentration of the 2000nm and 8330nm particles was detected within 2% of the expected value. To the best of the authors knowledge, there is no similar technique to evaluate particle size due to the vertical gravitational movement. Typical PTA systems have an upper limit of ~2μm due to limited Brownian motion of larger particles. The sinking analysis embedded in the ViewSizer™ 3000 (MANTA Instruments, USA) could potentially enable measurement of particles above this 2µm regime within the same technique – essentially extending the range of detectable particle sizes.

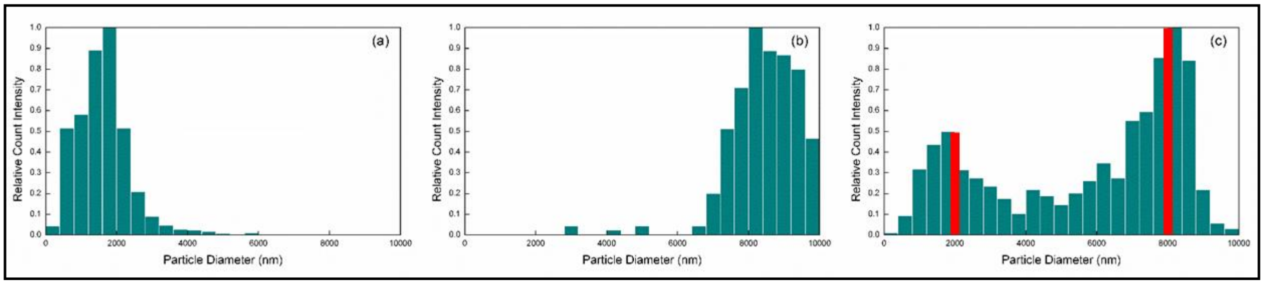

Figure 1.8. m-PTA measurement of monomodal (a) 8µm borosilicate, (b) 2µm borosilicate, and (c) a bimodal mixture of 8µm and 2µm borosilicate particles. The red bars on the histogram represent the expected relative intensities of the 8µm and 2µm peaks.

1.3.4 Polydisperse 316L Steel

While it is imperative to understand the reliability and accuracy of a technique in evaluating monomodal and multimodal standard solutions, naturally occurring particle formation mechanisms such as atmospheric nucleation, combustion, sedimentation, and solidification often have wide, sometimes directionally skewed, particle size distributions. Efficient particle size analysis must therefore be able to simultaneously measure large ranges of particles to capture a complete understanding of the distribution of interest. Moreover, the width and shape of certain particle size distributions can be used to trace the origins of the particles as is commonly done with atmospherically formed particles, in which the slope of the power-law distribution provides an indication to specific formation conditions like temperature. Likewise, shifts in particle size peak position can be used to distinguish changes in production mechanisms as with higher power settings in spark erosion leading to increased surface heating and larger average particle sizes. Considering this, the 316L nanopowder in use follows a natural production method of gas condensation and liquid solidification, which should provide naturally wide size distributions.

Figure 1.9 shows the results of SEM and TSEM imaging on the 316L nanopowder of interest. SEM observation found spherical polydisperse particles across 50nm - 10µm diameter range. These results agree well with what has been previously found in spark erosion literature [20, 22]. TSEM imaging found particle sizes 20nm and above, which also agrees with current literature.

The 316L particle size distributions produced by both DLS and m-PTA are illustrated in Figure 1.10 as (a-c) and (d-f), respectively. Table 1.4 lists the relevant quantities associated with each trial including mode-average, range, and full width at half maximum (FWHM). Figure 1.11 provides a log-log plot of the density of particle size distribution obtained by the m-PTA. An illustration of tracking results from the m-PTA real-time video feedback is featured in Figure 1.12. Post processing particle tracking through the m-PTA videos found low counts of particles ranging from 2 to 7µm (sinking).

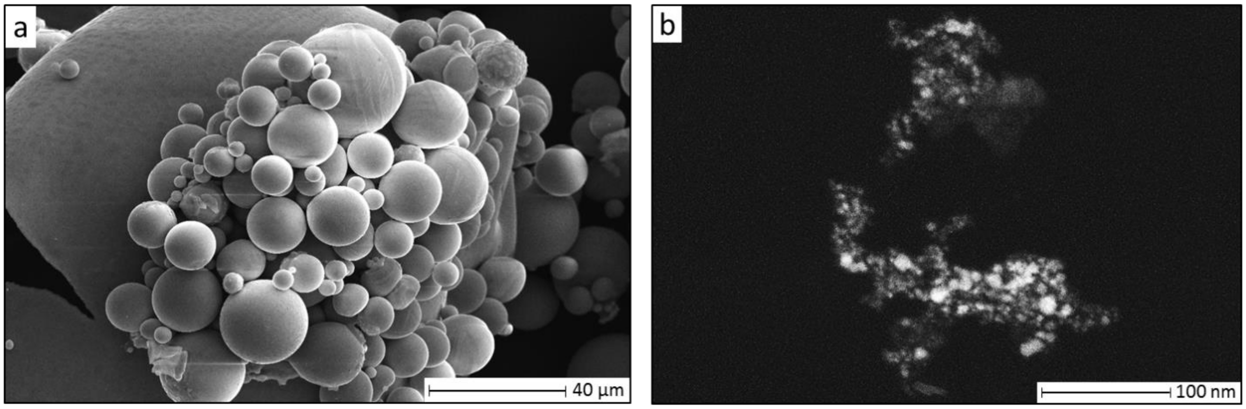

Figure 1.9. (a) Scanning electron microscopy of spark eroded 316L powder that shows spherical and polydispersely sized particles and (b) transmission scanning electron microscopy of the submicron sized 316L nanopowder.

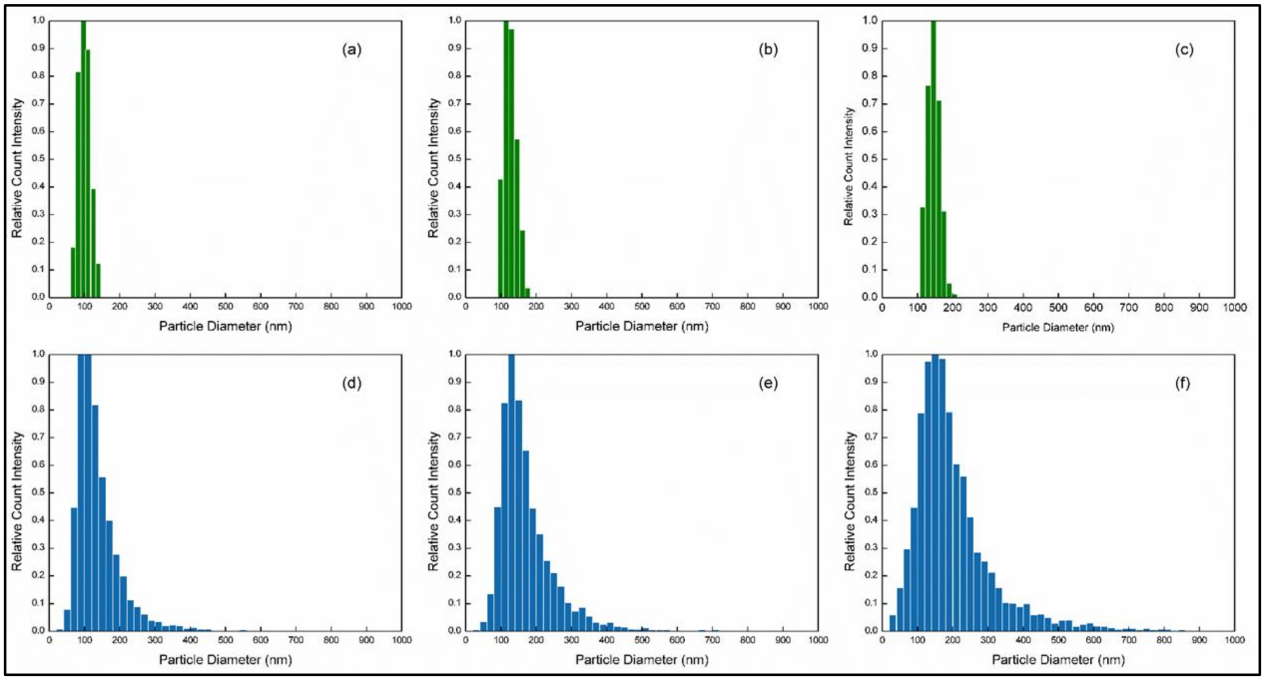

Figure 1.10. Plots of the 316L particle size analysis using (a-c) dynamic light scattering (DLS), and (d-f) m-PTA. Powders were synthesized from spark erosion trials at (a,d) low, (b,e) moderate, and (c,f) high capacitance values of 60μF, 100μF, and 120μF, respectively.

Table 1.4. Data extracted from the m-PTA and DLS analysis particle size analysis techniques of the 60μF, 100μF, and 120μF spark eroded nanopowders.

Spark Erosion Capacitance	Statistical Property	m-PTA	DLS
60μF	Mode-Average Radius (Particles Counted)	100nm (4013)	97nm
	Detected Range	30-910nm	67-139nm
	FWHM	74nm	43nm
100μF	Mode-Average Radius (Particles Counted)	129nm (4269)	122nm
	Detected Range	30-970nm	98-160nm
	FWHM	88nm	57nm
120μF	Mode-Average Radius (Particles Counted)	150nm (5197)	147nm
	Detected Range	10-930nm	115-235nm
	FWHM	133nm	59nm

Mode-average particle size analysis of the polydisperse 316L steel appears to be similar for m-PTA and DLS. The two techniques differed by only 3nm, 7nm, and 3nm, for the 60μF, 100μF, and 120μF trials, respectively. Likewise, both m-PTA and DLS detected slight increases in size average as the capacitance value increased, which quantitatively reflects the expected physical phenomenon of higher energy sparks producing larger average particles. These results agree with what was previously observed with comparable evaluation of the monomodal gold solutions.

The degree of variability between the shapes of the particle size distributions of either technique substantially increased as spark erosion capacitance was raised. The m-PTA FWHM values steadily grew with each step in capacitance, while the DLS FWHM values increased between 60µF and 100µF interval, but remained relatively constant between 100µF and 120µF, suggesting that the sensitivity of the DLS was unable to discern the increase in polydispersity between the 100µF and 120µF settings. The low concentration/counts of particles in the 300-500nm range were possibly lost through poor-fitting that may occur in the autocorrelation function in mathematical interpretation of the DLS data. The concealment of low concentrations of 300-500nm 316L particles mirrors the previously observed inability of the DLS to detect the >100nm gold nanoparticles in the 50nm monomodal gold solution (Figure 1.4(a)).

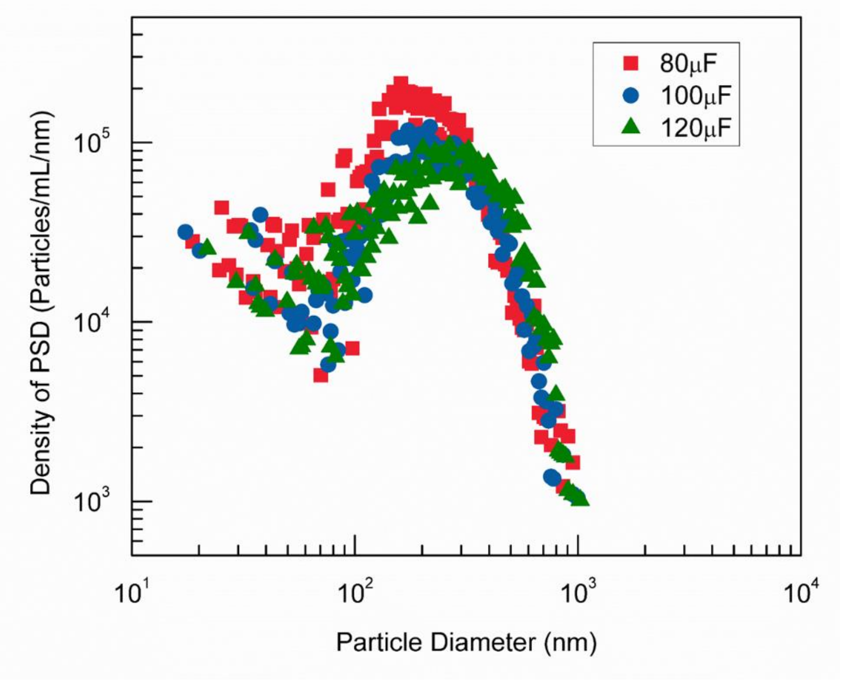

Figure 1.11. Plot of density of particle size distribution versus particle size.

Since particle formation in spark erosion involves liquid and gas aggregates mediated in a gaseous pocket, a parallel can be drawn to the formation of spherical atmospheric aerosol particles. Both processes are driven by homogeneous nucleation and aggregation, and are strongly influenced by local surrounding factors. As is common practice with aerosol particle size analysis, the number density size distribution and power-law fit can provide information regarding the production mechanism [33–35]. The log-log form of the density of particle size vs. particle diameter featured in Figure 1.8 clearly illustrates the similarity of the near-linear descent of the particle size number density as particle sizes increase across all three samples. Despite the increase in capacitance setting, the identical PSD slopes indicate that the ratio of small particles to large particles remains steady. Further increases in capacitance may result in flattening of the slope corresponding to an increase in relative concentration of large particles. The amount of noise in the 20nm-80nm region does not give a good indication of the size distribution mechanics in that range. The low signal to noise ratio could possibly be improved by increasing the number of videos analyzed for each trial.

Video feedback post-processing was performed to detect micron-sized 316L particles that remained after filtering. Figure 1.12 provides a sequence of images revealing the steady ‘sinking’ of a large particle in the solution outlined in red. For the online version of this study, the video feedback is shown in Figure 1.12 in which the larger particles can be observed as slow, vertically moving objects, while the smaller particles are the fast moving (Brownian) objects. The low count of large particles (<50 particles/sample) found during kinetic post-processing suggests that the sedimentation filtration was successful in selecting predominately small particles of interest. Other than sedimentation, no other noteworthy dynamic processes were observed.

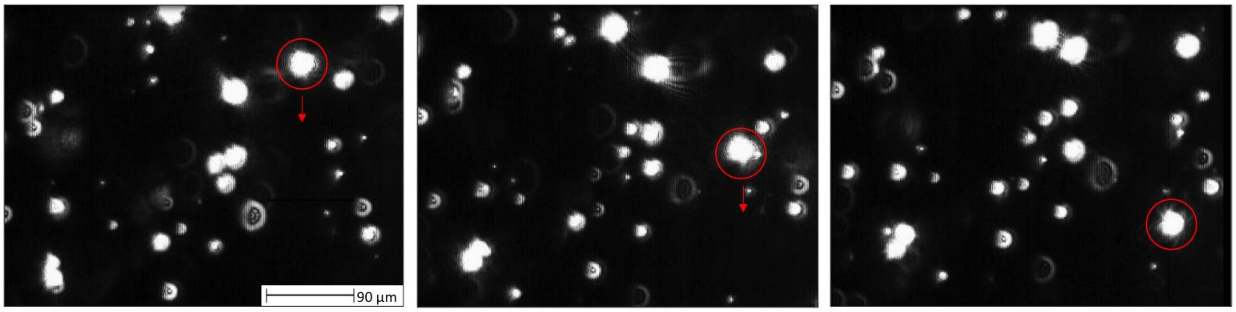

Figure 1.12. Tracking the non-Brownian motion of the circled 316L steel particle found it has a 4µm hydrodynamic diameter. Frame progression is left to right and each frame progresses by approximately one second.

1.4 Conclusions

The m-PTA embedded in the ViewSizer™ 3000 proved to be a powerful tool for evaluating monomodal, multimodal, and polydisperse mixtures of gold and polystyrene nanoparticles. The accuracy of relative concentration measurement, within 2-5% for all trials, dramatically outperformed its DLS counterpart and indicates that this technique may be a reliable tool for quantitative evaluation. The observed sensitivity to low concentrations of particles is evidently one strength of this technique, however, it does suggest that care must be taken to discern data of interest from foreign objects or particles with larger hydrodynamic radii due to absorption or coagulation. The ability to analyze particle size through gravitational sedimentation was shown be successful and may have potential to extend the upper limit of tradition PTA, however, further testing of this capability is suggested to better understand possible limitations. The simplicity, low-cost, and reliability of DLS assures its future as a useful and effective tool in particle size analysis, nevertheless, the evident strengths of this multispectral particle tracking technique could place it in the forefront of future nanoparticle analysis technologies where existing technologies fall short.

The authors suggest that future work with this technique considers evaluating mixtures of particles with sizes above and below the 2µm regime to assess m-PTA capability of simultaneously discerning motion of Brownian and non-Brownian particles. According to Stoke's Law for settling particles, terminal velocity is proportional to the squared radius of the particle and difference in density between the solution and material of interest. With this in mind, the authors suggest future work testing the upper limit of the sinking analysis capabilities, which may be influenced by the material and diluent of choice. In addition, the authors suggest future work evaluating the effect of periodic stirring and measurement time delay to understand the role of evanescent turbulent flow in sinking measurements.

1.5 Acknowledgements

Part 1, is a modified reprint of material that appears in Measurement Science and Technology, 2018, McElfresh, Cameron; Harrington, Tyler; Vecchio, Kenneth. The thesis author was the primary investigator and author of this material. Special thanks to Dr. Kuba Tatarkiewicz, Rick Cooper, Cindy Rosal and the MANTA Instruments, Inc. team for assistance with experiments and useful scientific discussion.

1.6 References

[1] I.W. Andrew, N. Shipway, E. Katz, Nanoparticle Arrays on Surfaces for Electronic, Optical, and Sensor Applications, ChemPhysChem. **1** (2000) 18–52. doi:10.1002/1439-7641.

[2] P.S.V. Mocherla, C. Karthik, R. Ubic, M.S. Ramachandra Rao, C. Sudakar, Tunable bandgap in BiFeO3 nanoparticles: The role of microstrain and oxygen defects, Appl. Phys. Lett. **103** (2013) 022910. doi:10.1063/1.4813539.

[3] B.O. Han, E.J. Lavernia, Z. Lee, S. Nutt, D. Witkin, Deformation behavior of bimodal nanostructured 5083 Al alloys, Metall. Mater. Trans. A. **36** (2005) 957–965. doi:10.1007/s11661-005-0289-7.

[4] T.-S. Yeh, M.D. Sacks, Effect of Particle Size Distribution on the Sintering of Alumina, J. Am. Ceram. Soc. **71** (1988) C-484-C-487. doi:10.1111/j.1151-2916.1988.tb05812.x.

[5] J. Carrey, H.B. Radousky, A.E. Berkowitz, Spark-eroded particles: Influence of processing parameters, J. Appl. Phys. **95** (2004) 823–829. doi:10.1063/1.1635973.

[6] P.K. Nguyen, K.H. Lee, J. Moon, S.I. Kim, K.A. Ahn, L.H. Chen, S.M. Lee, R.K. Chen, S. Jin, A.E. Berkowitz, Spark erosion: a high production rate method for producing $Bi_{0.5}Sb_{1.5}Te_3$ nanoparticles with enhanced thermoelectric performance, Nanotechnology. **23** (2012) 415604. doi:10.1088/0957-4484/23/41/415604.

[7] T. Harrington, C. McElfresh, K.S. Vecchio, Spark Erosion as a High-throughput Method for Producing Bimodal Nanostructured 316L Stainless Steel Powder, Powder Technol. **328** (2018) 156-166. doi.org/10.1016/j.powtec.2018.01.012.

[8] M. Hassellöv, J.W. Readman, J.F. Ranville, K. Tiede, Nanoparticle analysis and characterization methodologies in environmental risk assessment of engineered nanoparticles, Ecotoxicology. **17** (2008) 344–361. doi:10.1007/s10646-008-0225-x.

[9] E. Tomaszewska, K. Soliwoda, K. Kadziola, B. Tkacz-Szczesna, G. Celichowski, M. Cichomski, W. Szmaja, J. Grobelny, Detection limits of DLS and UV-Vis spectroscopy in characterization of polydisperse nanoparticles colloids, J. Nanomater. **2013** (2013). doi:10.1155/2013/313081.

[10] S.K. Brar, M. Verma, Measurement of nanoparticles by light-scattering techniques, TrAC - Trends Anal. Chem. **30** (2011) 4–17. doi:10.1016/j.trac.2010.08.008.

[11] H.C. Hulst, Light Scattering By Small Particles, Dover Publications Inc., New York, 1981. doi:0-486-64228-3.

[12] J.A. Gallego-Urrea, J. Tuoriniemi, M. Hassellöv, Applications of particle-tracking analysis to the determination of size distributions and concentrations of nanoparticles in environmental, biological and food samples, TrAC - Trends Anal. Chem. **30** (2011) 473–483. doi:10.1016/j.trac.2011.01.005.

[13] S. Ristig, S. Chernousova, W. Meyer-Zaika, M. Epple, Synthesis, characterization and in vitro effects of 7 nm alloyed silver-gold nanoparticles, Beilstein J. Nanotechnol. **6** (2015) 1212–1220. doi:10.3762/bjnano.6.124.

[14] D. Mahl, J. Diendorf, W. Meyer-Zaika, M. Epple, Possibilities and limitations of different analytical methods for the size determination of a bimodal dispersion of metallic nanoparticles, Colloids Surfaces A Physicochem. Eng. Asp. **377** (2011) 386–392. doi:10.1016/j.colsurfa.2011.01.031.

[15] J.A. Gallego-Urrea, J. Tuoriniemi, T. Pallander, M. Hassellöv, Measurements of nanoparticle number concentrations and size distributions in contrasting aquatic environments using nanoparticle tracking analysis, Environ. Chem. **7** (2010) 67–81. doi:10.1071/EN09114.

[16] D. Stramski, J. Tatarkiewicz, R. Reynolds, M. Karr, Nanoparticle Analyzer, US20150346076 A1, 2015.

[17] D.P. Jones, W. Hanna, H. El-Hamidi, J.P. Celli, Longitudinal measurement of extracellular matrix rigidity in 3D tumor models using particle-tracking microrheology., J. Vis. Exp. **88** (2014) e51302. doi:10.3791/51302.

[18] E. Van Der Pol, C. Gardiner, Particle size distribution of exosomes and microvesicles determined by transmission electron microscopy , flow cytometry , nanoparticle tracking analysis , and resistive pulse sensing, J. Thromb. Haemost. **12** (2014) 1182–1192. doi:10.1111/jth.12602.

[19] C. Gardiner, Y.J. Ferreira, R.A. Dragovic, C.W.G. Redman, I.L. Sargent, Extracelluar vesicle sizing and enumeration by nanoparticle tracking analysis, J. Extracell. Vesicles. **2** (2013) 1–11. doi:10.3402/jev.v2i0.19671.

[20] J. Gross, S. Sayle, A.R. Karow, U. Bakowsky, P. Garidel, Nanoparticle tracking analysis of particle size and concentration detection in suspensions of polymer and protein samples : Influence of experimental and data evaluation parameters, Eur. J. Pharm. Biopharm. **104** (2016) 30–41. doi:10.1016/j.ejpb.2016.04.013.

[21] X. Tian, M.R. Nejadnik, D. Baunsgaard, A. Henriksen, C. Rischel, W. Jiskoot, A Comprehensive Evaluation of Nanoparticle Tracking Analysis (NanoSight) for Characterization of Proteinaceous Submicron Particles, J. Pharm. Sci. **105** (2016) 3366–3375. doi:10.1016/j.xphs.2016.08.009.

[22] R.A. Dragovic, C. Gardiner, A.S. Brooks, D.S. Tannetta, D.J.P. Ferguson, P. Hole, B. Carr, C.W.G. Redman, A.L. Harris, P.J. Dobson, P. Harrison, I.L. Sargent, Sizing and phenotyping of cellular vesicles using Nanoparticle Tracking Analysis, Nanomedicine Nanotechnology, Biol. Med. **7** (2011) 780–788. doi:10.1016/j.nano.2011.04.003.

[23] T. Tran, P. Saveyn, H. Dinh, P. Van Der Meeren, Determination of heat-induced effects on the particle size distribution of casein micelles by dynamic light scattering and nanoparticle tracking analysis, Int. Dairy J. **18** (2008) 1090–1096. doi:10.1016/j.idairyj.2008.06.006.

[24] W. Anderson, D. Kozak, V.A. Coleman, Å.K. Jämting, M. Trau, A comparative study of submicron particle sizing platforms : Accuracy , precision and resolution analysis of polydisperse particle size distributions, J. Colloid Interface Sci. **405** (2013) 322–330. doi:10.1016/j.jcis.2013.02.030.

[25] A.E. James, J.D. Driskell, Monitoring gold nanoparticle conjugation and analysis of biomolecular binding with nanoparticle tracking, Analyst. **138** (2013) 1212–1218. doi:10.1039/c2an36467k.

[26] V. Filipe, A. Hawe, W. Jiskoot, Critical Evaluation of Nanoparticle Tracking Analysis (NTA) by NanoSight for the Measurement of Nanoparticles and Protein Aggregates, Pharm. Res. **27** (2010) 796–810. doi:10.1007/s11095-010-0073-2.

[27] F. Part, G. Zecha, T. Causon, E. Sinner, M. Huber-humer, Current limitations and challenges in nanowaste detection , characterisation and monitoring, Waste Manag. **43** (2015) 407–420. doi:10.1016/j.wasman.2015.05.035.

[28] C.F. Bohren, D.R. Huffman, Absorption and Scattering of Light by Small Particles, Wiley, New York, 1983.

[29] V.C. Solomon, J. Il Hong, Y. Tang, A.E. Berkowitz, D.J. Smith, Electron microscopy investigation of spark-eroded Ni-Mn-Ga ferromagnetic shape-memory alloy particles, Scr. Mater. **56** (2007) 593–596. doi:10.1016/j.scriptamat.2006.12.034.

[30] J. Walter, A. Berkowitz, Method for fabrication of low cost finely divided silicon-germanium and consolidated compacts thereof, US4759905 A, 1988.

[31] R.W. Cahn, J.L. Walter, D.W. Marsh, Characteristics of Ni3Al plus Fe powders produced by spark erosion quenching, Mater. Sci. Eng. **98** (1988) 33-37. doi:10.1016/0025-5416(88)90121-8.

[32] N. Ben Salah, F. Ghanem, B.K. Atig, Thermal and mechanical numerical modelling of electric discharge machining process, Commun. Numer. Meth. Engng. **24** (2008) 2021–2034. doi:10.1002/cnm.1091.

[33] C. Junge, The Size Distribution and Aging of Natural Aerosols As Determined From Electrical and Optical Data on the Atmosphere, J. Meteorol. **12** (1955) 13–25. doi:10.1175/1520-0469(1955)012<0013:TSDAAO>2.0.CO;2.

[34] C.H. Jung, Y.P. Kim, Simplified Analytic Model to Estimate the Ångstrom Exponent in a Junge Aerosol Size Distribution, Environ. Eng. Sci. **27** (2010) 789–795. doi:10.1089/ees.2010.0030.

[35] G.L. Schuster, The Angstrom Exponent and Bimodal Aerosol Size Distributions, J. Geophys. Res. **111** (2005) D07207. doi:10.1029/.

Part 2

Spark Erosion as a High-throughput Method for Producing Bimodal Nanostructured 316L Stainless Steel Powder

2.1 Introduction

Following the discovery of their unique properties, nanoparticles have seen a drastic rise in application across many industries, driving the need for production of nanoparticles of a wide array of materials. Typical chemical synthesis methods can generate uniform particles with well-controlled sizes; however, these methods require specific reaction pathways for generating particles and are often low-throughput. This limits them to single element compositions, so they are not applicable to alloys, and not enough powder can be obtained to produce bulk structural parts. By comparison, spark erosion is a high-throughput, scalable, clean, and versatile technique that has been used to produce powders with particle sizes ranging from a few nm to more than 100µm and has been applied to materials including metals and alloys, semiconductors, and ceramics [1–7]. The process involves the breakdown of bulk samples using repeated electric discharges that produce a high-temperature arc within a dielectric fluid, and since it is a top-down process that breaks down bulk target materials into nanoparticles, it can be applied to a broad range of alloys. Erosion via an electric discharge is also the basis of the popular machining technique - electric discharge machining (EDM), and the initial experiments that investigated the use of spark erosion to produce nanostructured particles were actually carried out in EDM apparatuses [1–3]. During the erosion process, the arc reaches temperatures as high as 10^4K and pressures as high as 280MPa, which allows for the melting and vaporization of the sample material at the spark contacts [1–3,8–10]. The molten droplets are quenched *in situ*, and the vapor is condensed into small droplets that are then also quenched [3,11]. It is theorized that these two separate mechanisms of particle formation inherently lead to a bimodal powder distribution, in which the quenched molten droplets form the larger particles, and the condensed vapors form the nanoscale particles [3,11]. It has been demonstrated that the particle size distribution and the spark erosion rate are heavily dependent on both the choice of dielectric fluid and the energy parameters [11,12]. Higher energy sparks (>100mJ) have been shown to produce between 1% and 5%, by mass, of nanostructured powder, where lower energy sparks (<10mJ) can produce greater than 60% nanostructured particles [11]. Much of the previous research in spark erosion has focused on the minimization of the occurrence of the larger particle mode to produce nanostructured powders [2–6,13]. However, as many previous studies have demonstrated, the bimodal powder distribution can be beneficial for various reasons. It has been shown that the density of green compacts and final sintered or injection molded parts is increased when a multimodal particle size distribution of 316L powder is used [14–16]. Also, the initial bimodal distribution leads to a bimodal grain structure when consolidated into bulk structures, which can be desirable for enhanced mechanical properties such as strength and ductility [17–21]. The bimodal grain structures can result in a material with a drastic increase in strength due to Hall-Petch strengthening in the finer grained regions while maintaining ductility due to the work hardening ability of the coarser grained regions [19–23]. This work aims to present a novel, high-yield, powder generation technique for production of bimodal powder distributions of a widely used structural alloy, 316L stainless steel, with the optimum distribution for sintering of bulk bimodal structured materials.

2.2 Materials and Methods

Type 316L stainless steel in the form of rectangular bar stock and spherical bearings (both obtained from McMaster Carr, Los Angeles, CA, USA) of composition listed in Table 2.1 were used as the sample target material throughout this investigation. The “shaker-pot” spark erosion apparatus, outlined in Figure 2.1, designed by Berkowitz *et al*. [1–5,12,13,24], was employed for nanoparticle production. The device consists of a plastic cell container with two electrodes, connected to a relaxation oscillator, separated by porous insulating base plates. The relaxation oscillator consists of a DC voltage source that charges a capacitor until the breakdown voltage is reached, causing the capacitor to discharge [1–5,13]. The entire assembly is held within a hollow walled, vacuum jacket, glass container that is filled with a dielectric fluid. Target pieces of the desired material for powder production are placed between the electrodes, and the pot is shaken laterally, causing the target pieces to repeatedly come into contact and separate at a high rate between the electrodes. When the gaps between the individual sample target pieces are small enough, and the field between the electrodes exceeds the dielectric breakdown field, the capacitor discharges producing sparks at the individual particle contact points [1]. The sparks create a plasma that contains electrons and ions, which superheats small regions of the surface of the targets up to temperatures in excess of 10^4K [1,2,8,10]. The localized vaporization of the dielectric fluid creates a vapor barrier around the plasma column that is confined by the relatively incompressible liquid. Due to the confinement of the vapor, pressures around the plasma column can reach an estimated 280MPa, which allows for the temperature to exceed the natural boiling point [3,9]. The extreme temperatures liquefy and vaporize a small area of the surface of the target pieces [25,26]. The molten and vaporized material is ejected by the force of the shock wave resulting from the collapsing of the gas jacket and is immediately quenched (or condensed) in the dielectric fluid.

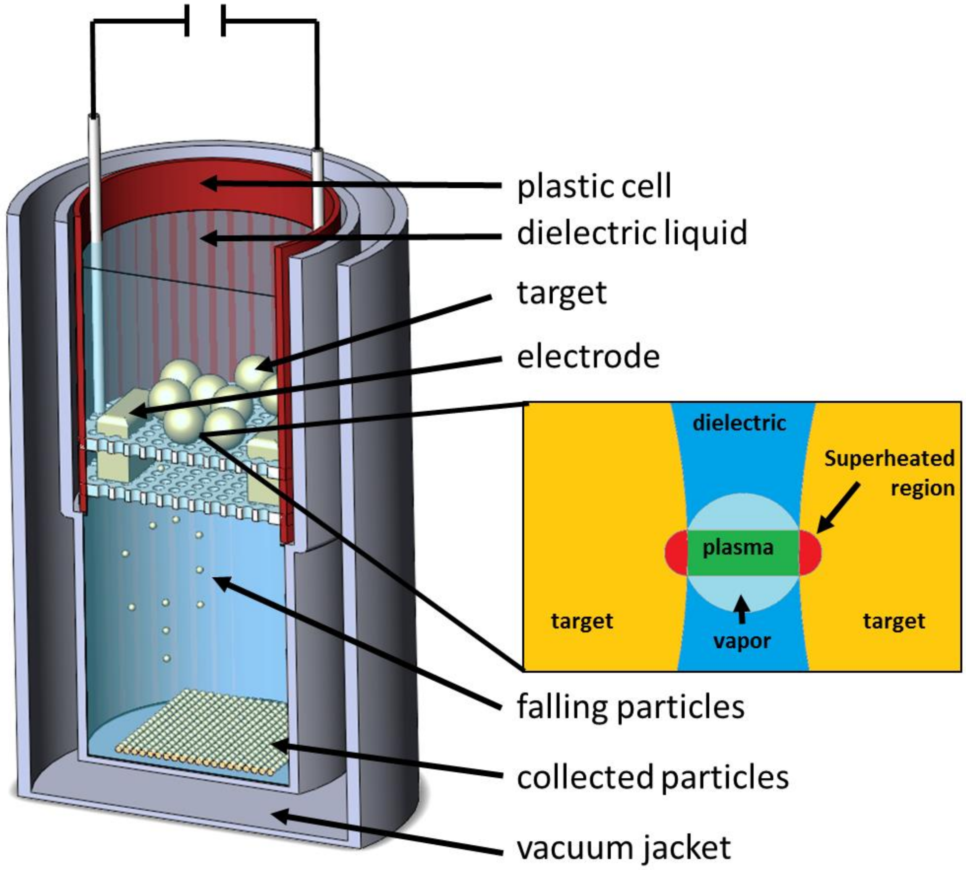

Figure 2.1. Schematic diagram of the "shaker-pot" spark erosion apparatus used for powder production throughout this investigation, where the sample material of interest is shown in gold.

Table 2.1. Composition of the as received rectangular bar stock and spherical bearing materials prior to spark erosion. Obtained from EDS analysis at 20kV.

	Fe (wt%)	Cr (wt%)	Ni (wt%)	Mo (wt%)	Mn (wt%)	Si (wt%)
Bar Stock	69.6	17.6	8.7	2.3	1.5	0.4
Bearings	68.7	17.4	10.0	2.2	1.3	0.5

2.2.1 Target Morphology Study

The three different target shapes depicted in Figure 2.2 were used to determine the optimum target morphology for the spark erosion process. The samples “a” were vacuum arc melted in a copper hearth to form a flattened semi-spherical “platelet” shape from a bar stock of commercially available 316L stainless steel, the “b” samples were rectangular sections cut directly out of the rectangular bar stock, and the “c” samples were spherical ball bearings ranging from 9.5mm to 16mm in diameter. Spark erosion was carried out using a capacitance of 120µF for two-hour runs on each sample morphology. The total number of sparks was recorded every ten minutes throughout the runs, and the average spark rate in Hertz was calculated for each ten-minute interval.

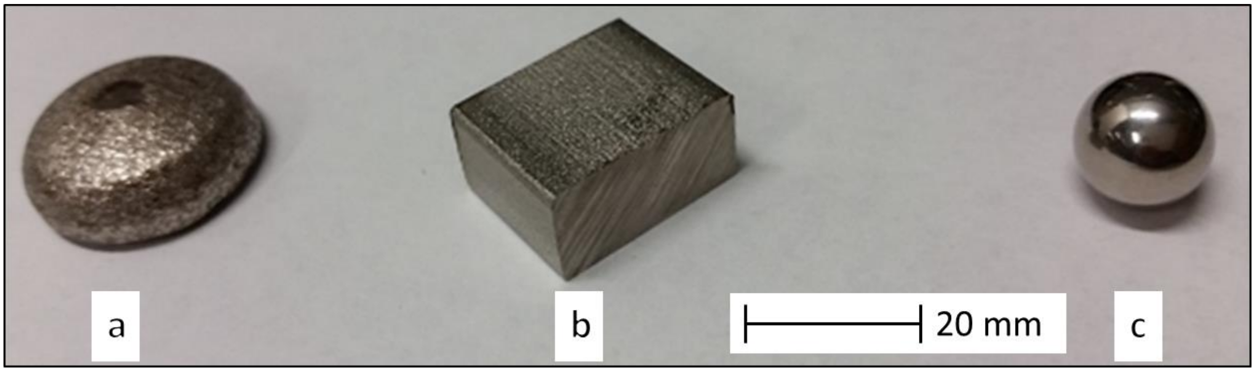

Figure 2.2. Image of the three targets used for spark erosion to test the effect of target morphology on erosion rate: (a) platelet, (b) rectangular, and (c) spherical.

2.2.2 Effect of Power Parameters and Liquid Dielectric on Powder Production

To determine the effect of the capacitance settings on the particle size, particle production rate, and spark energy, separate spark erosion runs were conducted with varying capacitance settings. The power supply voltage for capacitor charging was set to 200V and the current max to 4A. The motor revolutions per minute 1225 giving a shaker frequency of ~20Hz. Throughout every run, twenty 16mm, twenty 12.7mm, and five 9.5mm diameter spherical targets were used for a total of forty-five sample targets. The capacitance was set to each of the following values for individual runs: 120µF, 100µF, 80µF, 60µF, and 40µF. Trials were conducted for both ethanol and liquid nitrogen as a dielectric. For the ethanol trials, the total number of sparks was recorded every ten minutes of each run. The total spark count per ten-minute interval was divided by 600 seconds to determine an average rate in Hz for each interval. Spark energy was calculated for both ethanol and liquid nitrogen using the resultant voltage waveform observed during the sparking process. The surface of the target material was examined via SEM both before and after the spark erosion process. The calculated spark energy values along with the corresponding size distributions were used to better understand and control the sparking mechanism.

2.2.3 Powder Characterization

The powder was distilled and then left for 24 hours to dry following spark erosion. After initial drying, the powder sample was placed in a furnace at 300°C for 4 hours to remove any polymer contaminants from the reaction chamber. Initial powder analysis was done in a FEI Apreo FEG-SEM equipped with an Oxford X-Max^N EDS detector at an accelerating voltage of 20kV. Transmission SEM was also done in a FEI Apreo FEG-SEM with a tSEM detector at an accelerating voltage of 30kV. X-Ray Diffraction (XRD) analysis for phase identification and crystallite size determination was conducted using a Rigaku Rotaflex X-ray Diffractometer with a 2θ scan range of 20°-120°, a step size of 0.02°, and a dwell of 1 second. The crystallite size of the spark-eroded powders was determined by peak broadening in XRD. For this, scans of individual peaks were taken at a step size of 0.02° and a dwell of 10 seconds. Crystal size determination was done via Williamson-Hall [27] analysis, where the broadening due to crystallite size is given by Equation (1):

$$B = \frac{K\lambda}{t \cos \theta} \tag{1}$$

where B is the measured full width at half maximum (FWHM) of the diffraction peaks (2θ in radians), t is the diameter of the crystallites (Ȧ), λ is the x-ray wavelength (Ȧ), and K is a unitless shape parameter assumed to be equal to unity for spherical crystals [28]. The initial FWHM from instrumental broadening was determined using a NIST 660b LaB_6 standard powder for peak position and shape in XRD.

Both Dynamic Light Scattering (DLS) and Multispectral Advanced Nanoparticle Tracking Analysis (MANTA) were also used to characterize the size distribution of the particles. DLS is a well-understood particle characterization technique that is commonly used to determine size distribution profiles of particles in suspension. However, it has been found that polydisperse samples are inherently unreliable in traditional DLS because the scattering intensity of large particles can overwhelm the weak scattering intensity of smaller particles, thus resulting in an inaccurate size distribution. Because the 316L nanopowder of interest is known to have a bimodal/polydisperse particle size distribution, the MANTA technique was utilized in parallel to confirm and further analyze the size profiles.

As with DLS, in the MANTA technique, particles of interest are suspended in a contaminant-free solution. Rather than a single light source, three tunable lasers are employed to simultaneously illuminate the particles in solution. Scattered light from each source is individually collected and used to construct consecutive location profiles of the particles – ultimately resulting in a video of the particles movement. Particle movement videos of each wavelength can be simultaneously processed to determine which wavelength produces the most reliable description of the particle’s movement. Then, by combining the videos using only the optimal particle movement descriptors, an accurate portrayal of particle motion can be constructed. The selection of only the optimal scattering profiles largely eliminates errors induced due to varying scattering intensities of different sized particles. Since the Brownian motion of particles in a fluid is a well-understood mechanism, particle movement in videos can be tracked, evaluated, and correlated to the hydrodynamic radii of the particles present. The culmination of this results in a high-throughput detection technique that can individually count particles to create statistically robust size distributions. Powder dilutions for MANTA were made to 5.7 x 10^8 – 5.0 x 10^7 particles/mL in Xzero Type-1 reference water (XZERO, Sweden). MANTA was performed at a sampling rate of 25 videos per trial, 25 seconds per video, with automated stirring between each video to eliminate double counting of particles. DLS was performed on a Zeta Particle Sizer with 670nm light with 10 trials of 2 minute each. All solutions were ultrasonicated to break apart any agglomerates in the solution. Dilutions were allowed to settle before sampling from the top – to avoid a high population of oversized (>1µm) particles.

To confirm the bimodal nature of the powder, 10g of the 316L spark eroded powder was compacted at 50MPa for 2 minutes and the resulting green compact was mounted for further analysis. The surface was analyzed in a FEI Apreo SEM mode and individual particle sizes were measured. In a region of approximately 400um x 400um, a total of 4508 particles were counted ranging from 30nm to 80um. A number fraction distribution of particle sizes was created by binning particles based on the absolute number of particles counted within a certain diameter range, where the multiplicative factor, r^0 [29]. Likewise, a volume fraction distribution was created by weighting the bin intensity with volumetric multiplicative factor r^3 [29]. Both the number fraction and volume fraction distributions were normalized to relative intensity axes. The mode-average was found to be 120nm for the number fraction form and 30um for the volume fraction form.

2.3 Results and Discussion

2.3.1 Effect of Target Morphology on Erosion Rate

The shape of the target material used in the "shaker-pot" spark erosion method was determined to have a substantial impact on the powder production rate as illustrated in Figure 2.3. This impact is entirely due to mechanical effects within the target arrangement, as was independent of the energy parameters and dielectric fluid. The rectangular targets showed low spark rates, while the spherical targets showed the highest rates. The rectangular targets displayed a tendency to lock into an arrangement in constant contact between the electrodes, causing welding at the target contact points and shorting the circuit rather than allowing effective sparking. The spherical targets had the highest rate due to the close packing effect of spheres within the containment cell creating the maximum number of contact points for sparking to occur at a sustained rate without welding. The semi-spherical arc-melted targets tended to slide over the flat surfaces of each other, eventually reaching an arrangement where they were no longer separating and re-contacting to pass through optimum gap conditions for dielectric breakdown. Following determination of the spherical targets as the most efficient for erosion rate, all further runs were performed using only spherical ball bearing targets. Results from this study agree with those found by Berkowitz *et al.*, [3] that the targets should range from 9.5mm to 19mm and should be equiaxed.

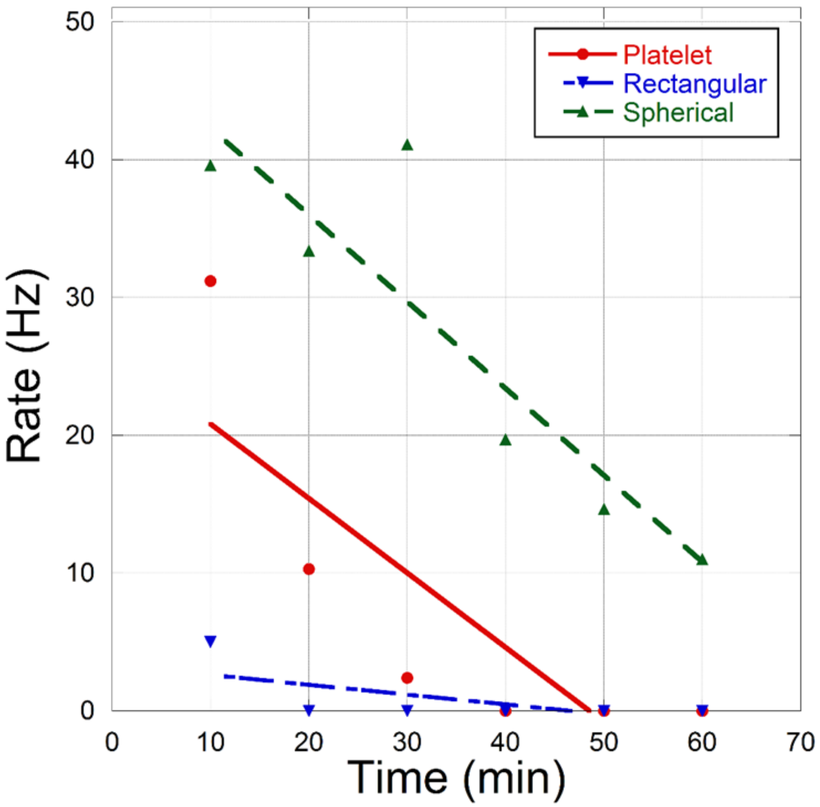

Figure 2.3. Plot of the spark erosion rate as a function of time for a 60-minute run using different target morphologies.

2.3.2 Effect of Capacitance Settings on Production Rate

The spark erosion setup relies on the energy of the relaxation oscillator and can be manipulated through the capacitance. The higher the capacitance of the system, the more energy available for discharge, so it is expected that the erosion rate, as well as particle distribution, will depend on the overall capacitance of the oscillator. Figure 2.4 shows the rate of spark discharge taken every 10 minutes during 160-minute runs with varying capacitances. The high capacitances of 120μF and 100μF show spark discharge rates between 30Hz and 40Hz for the first 30 minutes of the run that quickly decays to less than 10Hz after 40 minutes. The low rate for the high capacitances indicates that the sparking is not limited by the gap conditions of the target material arrangement, but by the charging conditions of the capacitor bank. It is likely that the higher capacitance requires a longer charge time and therefore will discharge at a lower rate, moving the process into an energy limited regime rather than a gap limited regime. The low capacitance run using 40μF shows a high starting rate of more than 60Hz for the first 50 minutes of the run, which begins to decay after 60 minutes and drops to 0Hz after 120 minutes. The high starting rate can be attributed to the faster complete charging of the capacitor bank. The intermediate trials using 60μF and 80μF capacitance initially show a slower increase in spark rate, reaching 50Hz after 50 minutes of erosion time. However, these capacitances maintain their high spark rate through a much longer duration. The 80μF trial decays below 50Hz at 100 minutes, while the 60μF run does not drop below 50Hz until 140 minutes into the run.

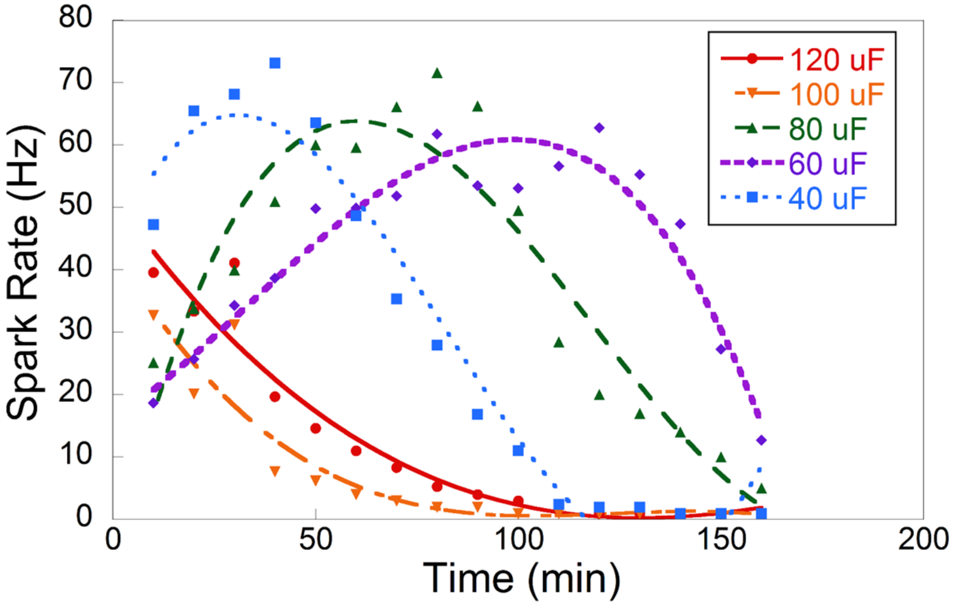

Figure 2.4. Plot of the spark erosion rate as a function of time for a 160-minute run at different capacitances.

Additionally, it is observed for each trial in the gap limited regime (40μF, 60μF, and 80μF) that the rate increases rapidly during the first 20 minutes, indicating that the small concentration of steel particles in the fluid aids in lowering the energy threshold for dielectric breakdown. This effect has been observed in similar applications of EDM, in which semiconducting or conducting particles decrease the dielectric strength of the suspending fluid [30,31]. The newly formed 316L particles act as interconnecting conductive sites that increase charge transport across the breakdown gaps. Reducing the breakdown voltage threshold lowers the capacitor recharge time and increases spark efficiency. In addition, the random orientation of particles in solution increases the maximum possible breakdown gap distance by forming low-energy discharge paths that are beyond the maximum possible breakdown distance of the pure dielectric. Increasing the discharge distance has a multiplicative effect on spark rate by enabling more potential breakdown paths.

The decrease in spark rate for the 40μF, 60μF, and 80μF samples can similarly be understood from the perspective of capacitors discharging in a dielectric with suspended conductive particles. High particle concentrations lead to adhesion of particles to the surface of target electrodes, creating loosely held layers of debris that inhibit the sparking mechanism. Significant particle presence may also lead to short-circuit discharging that eliminates the erosion effect and ultimately terminates the particle formation mechanism. Since the 40μF sample begins at a higher sparking rate, the threshold particle concentration for the stunting of the sparking mechanism is achieved faster than the 60μF and 80μF trials.

Figure 2.5 features the extracted spark time, voltage, and calculated energy properties with varying capacitance settings of the relaxation oscillator. Both liquid nitrogen and ethanol were found to have similar spark times through all capacitance values. Sparks were observed to be shortest at 10μF with a spark time of ~25μs and longest at 200μF with a spark time of near 120μs. As expected, in both ethanol and liquid nitrogen discharge voltage, and consequently total spark energy, increases with capacitance.

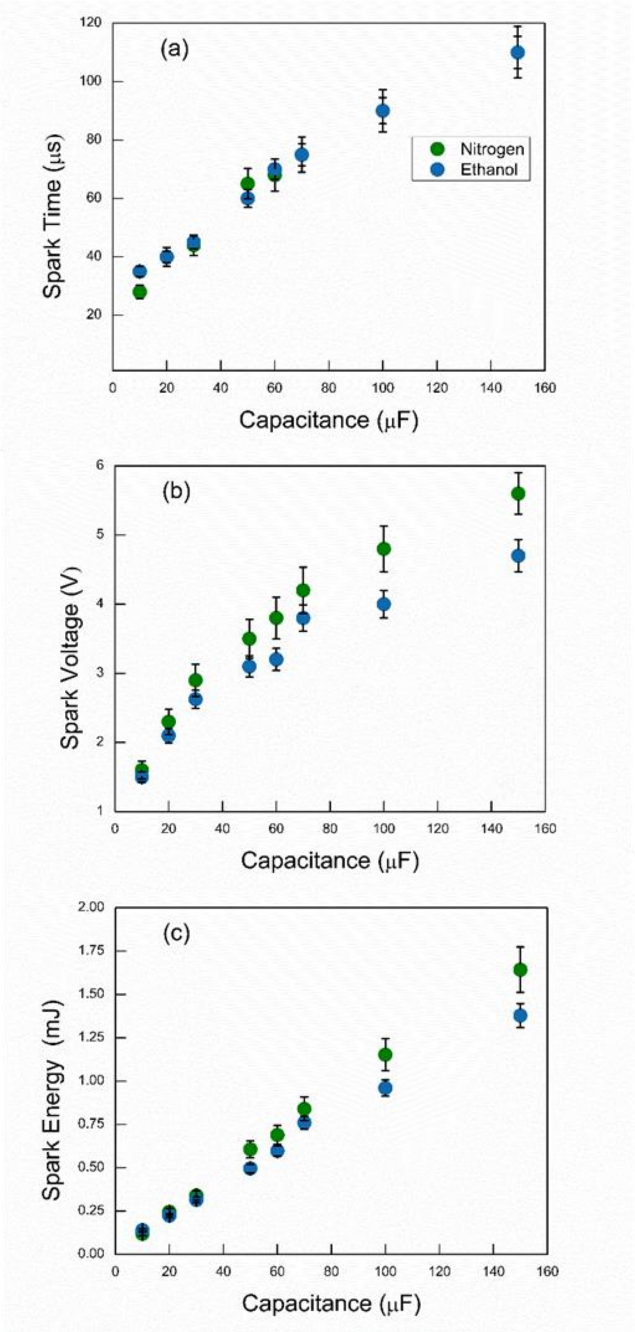

Figure 2.5. Plots of monitored spark properties with varying capacitance and dielectric. Measured properties were (a) spark time, (b) maximum spark voltage, and (c) resultant spark energy with respect to varying capacitance.

As capacitance increased beyond 60μF, however, sparks in the liquid nitrogen dielectric exhibited a noticeably higher spark voltage than those in ethanol at the same capacitance. It is possible that the higher required spark voltage in liquid nitrogen is due to its significantly lower dielectric strength (ε_r = ~1.4) compared to ethanol (ε_r = ~24). However, it must be noted that because the spark voltage and time data was extracted through an indirect method of monitoring the voltage discharges across the capacitors, it is likely that it is not quantitatively representative of the complex, and arguably uncontrolled, plasma-sparking mechanism that is occurring. Due to the shaker-pot implementation, it is certain that sparks between adjacent electrodes are occurring at widely variable distances, times, intensities, etc. This magnitude of variability indicates a more sensitive analysis technique must be employed to better understand the spark plasma properties.

Figure 2.6 features SEM analysis of the target surface before and after the spark erosion process. Figure 2.6(b-d) illustrate the unique surface topology of the target surface post-erosion. The craters represent areas that were in the immediate central zone of the plasma discharge region. The lost material in the craters was likely vaporized and ejected once the channel collapsed. The lighter area around the crater, and often inside the crater as well, is the solidified material that was thermally affected, but not vaporized. These areas still experienced extreme thermal discharges but did not reach sufficiently high temperatures or pressures to eject from the surface. Lighter areas are often referred to as "white layers" when classified in EDM context and are typically undesirable due to both surface roughness, as well as phase changes that occur during the rapid heating and cooling of the material [32]. It is unclear whether "white layers" affect spark erosion. However, the resolidification of molten material creates significant target surface roughness that may assist in low-voltage breakdown sites due to areas of locally concentrated electric fields [33]. This claim is supported by observation of Figure 2.6(b), Figure 2.6(c) and other target surfaces, in which large volumes of ejection sites appear to clump together indicating that ejection sites created areas of preferential breakdown.

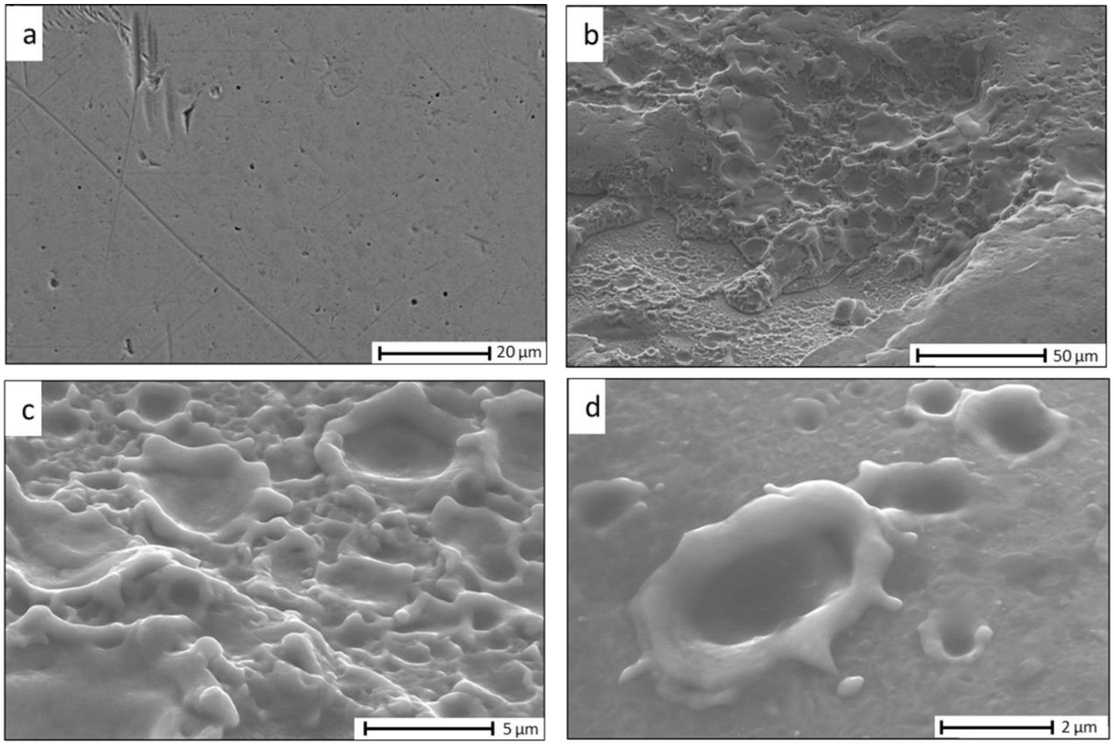

Figure 2.6. (a) Low magnification SEM evaluation of the target surface prior to spark erosion, (b) low magnification of clustered ejection sites on the target surface after spark erosion, (c) and (d) higher magnification images of the ejection sites illustrating individual ejection sites ranging from 5µm to 500nm.

2.3.3 Powder Microscopy

SEM analysis confirms that the spark erosion of 316L stainless steel successfully produced spherical particles with sizes ranging from 5nm to 75µm, in agreement with previous results from Berkowitz *et al.*, [1] for a number of materials. Figure 2.7(a-b) depicts SEM and t-SEM images of spark eroded powder, showing both the larger mode of uniform spherical particles (up to 50µm), numerous agglomerates of smaller particles, as well as dispersed ultra-fine particles (<100nm). Figure 2.7c features a cracked hollow spherical particle, which were primarily observed in the powder that was produced in liquid nitrogen and was typically found as particles larger than ~80µm. The occurrence of hollow particles has been observed in previous work with the spark erosion technique and is believed to be due to the condensation of superheated surface material on the gas liquid interface of individual bubbles [4,34,35]. Although these hollow microspheres do occur, they are outliers and are not expected to contribute significantly to the overall particle distribution. Results of chemical analysis of the metals in the powder product of the spark erosion process done in ethanol and liquid nitrogen are given in Table 2.2. The chemical composition following spark erosion mirrors that of the initial material, indicating that no significant change in chemical composition of the alloy has taken place during the erosion process. This is expected due to the high temperature of the erosion process, which is enough to vaporize each of the metals and allow them to mix in the vapor state, leading to a homogeneous distribution that is essentially equivalent to the starting material [7]. There is also no apparent difference in composition of the metals between the products of spark erosion in liquid nitrogen and ethanol and no detectable nitrogen peak was visible in EDS for the nitrogen processed powders.

Table 2.2. Composition of the powder products following spark erosion. Obtained from EDS analysis at 20kV.

	Fe (wt%)	Cr (wt%)	Ni (wt%)	Mo (wt%)	Mn (wt%)	Si (wt%)
Ethanol	69.1	17.1	10.0	2.2	0.9	0.7
Liquid N_2	69.2	17.6	9.7	2.0	1.2	0.4

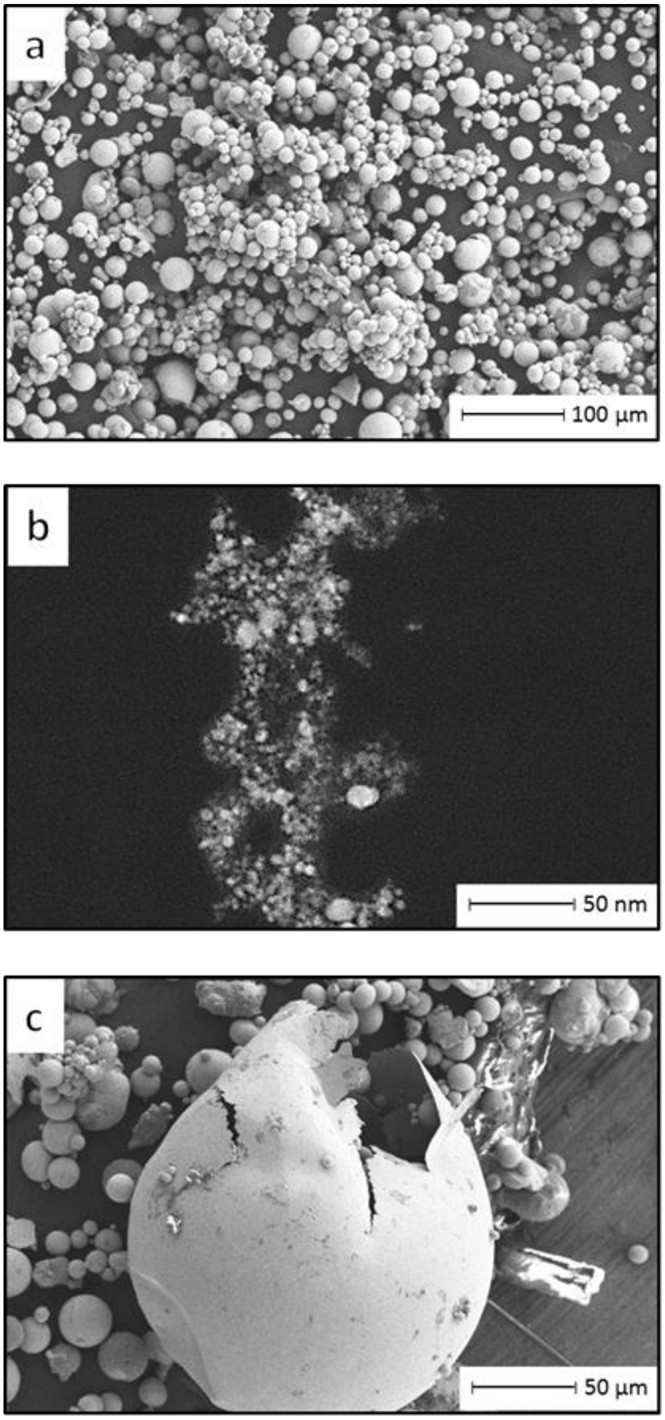

Figure 2.7. (a) Low magnification secondary electron image of the spark eroded powder reveals the polydisperse and varied size distribution of the particles, (b) HAADF t-SEM image depicting particles in the <25nm range, and (c) large hollow particle, which form as a result of the spark erosion process.

2.3.4 XRD Analysis

Figure 2.8(a) contains the diffraction patterns for the spark eroded powder in cryogenic N_2 and ethanol (60µF) compared to the as-received commercial powder (<43µm), revealing that the powder remains crystalline, in agreement with results found in previous work [6]. Both patterns show primarily austenite with a small amount of retained ferrite or martensite. The analysis for differentiation between retained ferrite and martensite is beyond the scope of this study, however the role of nitrogen suggests that the structure contains martensite rather than retained ferrite. The existence of ferrite/martensite was also seen previously by Marnier *et al.* [36], and is likely due to the large number of defects introduced during preparation, which increases the free energy of the austenite phase and thereby stabilizes the ferrite phase [37]. Considering the role of nitrogen as an austenite stabilizer, it is interesting to note that there is significantly less austenite in the powder that was spark eroded in liquid nitrogen. This is likely due to the low temperature of the liquid nitrogen following the particle formation. The low temperature of the liquid nitrogen allows the particles to reach the martensite start temperature and form martensite from the austenitic region, where the entire cooling process within ethanol never reaches the martensite transformation temperature. Figure 2.8(b) shows a higher magnification of the [200] diffraction peaks of the commercial powder, ethanol spark eroded powder, and liquid nitrogen spark eroded powder where extensive broadening of the spark eroded powder peaks due to a smaller average crystallite size is clearly demonstrated. The slight difference in FWHM of the ethanol and liquid nitrogen spark eroded samples shows broader peaks for the ethanol powder, which suggests that the liquid nitrogen results in slightly larger particle distribution than the ethanol. The calculated average crystallite size from Williamson-Hall analysis for the spark eroded 316L sample is 150 ± 26nm, which is within the range of accurate determination via peak broadening in a laboratory XRD and agrees with results attained via t-SEM analysis, DLS, MANTA, and previous work in spark erosion [1–5,12,13,24,35].

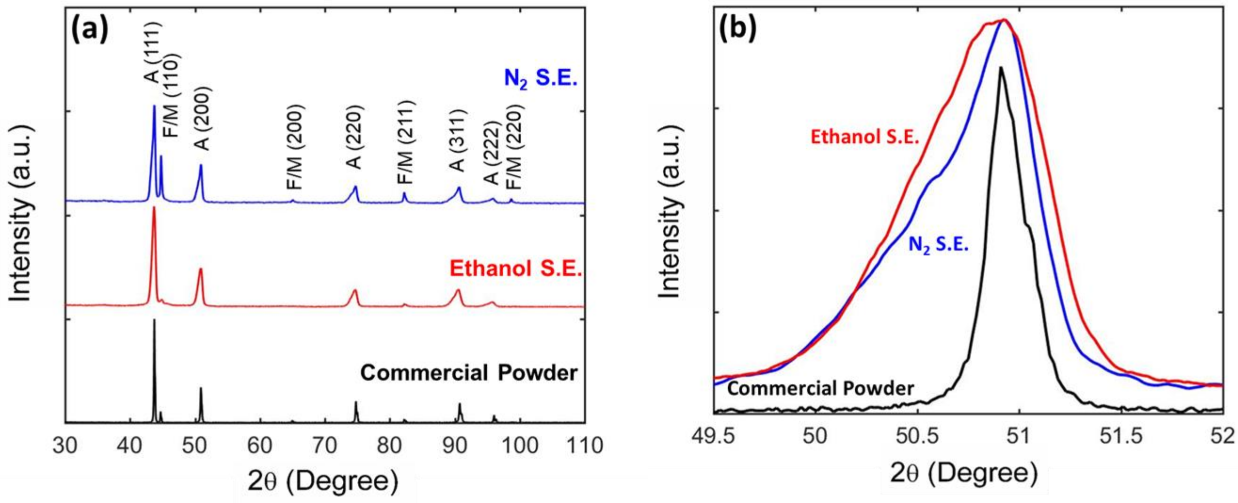

Figure 2.8. (a) 20˚–120˚ XRD patterns for the commercial powder and spark eroded powder, where A denotes the FCC austenite structure, and F/M denotes the BCC ferrite or BCT martensite structure. (b) zoomed in pattern of the [200] peak of the FCC structure.

2.3.5 Dynamic Light Scattering

DLS trials were conducted for powders produced in the 20-150μF size range. In general, it was found that as the capacitance was increased, the average particle size increased. Figure 2.9 is an illustration of the particle size distribution for a 60μF trial using ethanol as the dielectric. The average of the lower mode for this trial was found to be 156nm. The lower range of particle size agrees well with the XRD-calculated range of 124-176nm. However, upon further investigation, it was clear that much of the data found through DLS was largely truncated and incomplete. SEM and t-SEM observation of the 60μF powder found many particles above and below 100nm, suggesting that over or under-exposure of certain scattering intensities in the polydisperse sample lead to significant losses of information. A comparative illustration of MANTA performed on the same solution is featured in Figure 2.9. The small population of nanoparticles in the 800nm range appears to be overexpressed in DLS analysis. This is possibly due to higher scattering intensity of larger particles overwhelming that of the smaller particles and skewing the distribution. Furthermore, the same issue is apparent below 100nm, in which DLS cannot detect the lower concentrations of small diameter particles. Due to the inaccuracies found during DLS, the remainder of the discussion will be focused on particle size distributions detected through alternative methods such as SEM and MANTA.

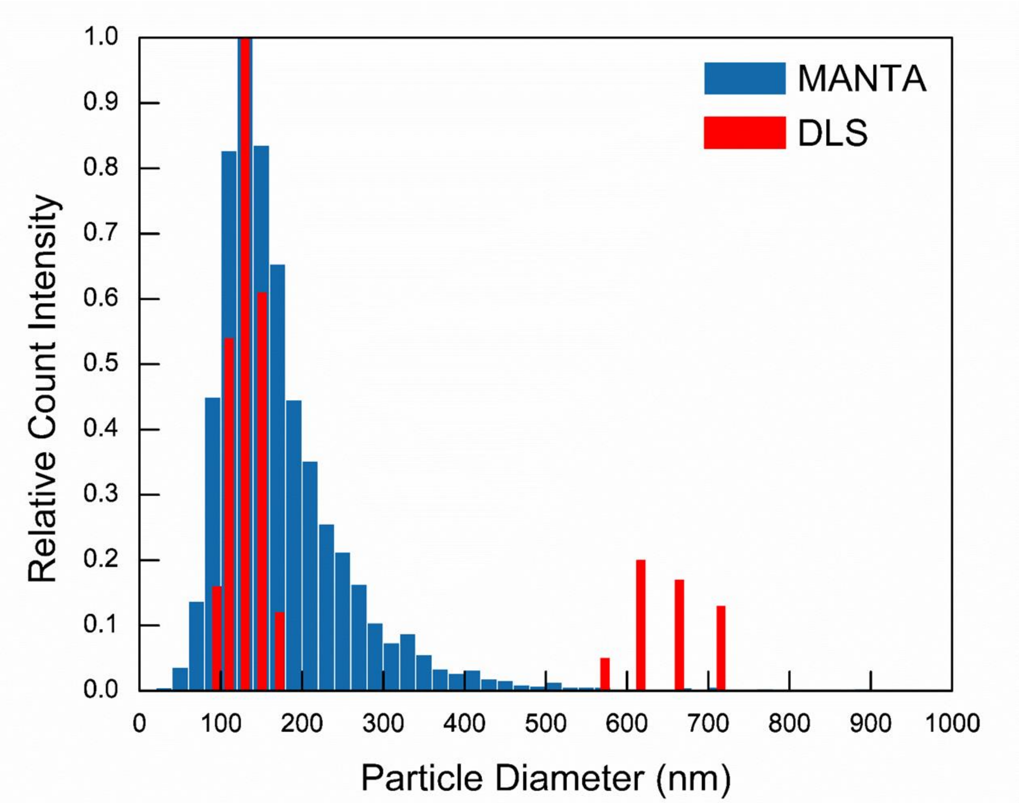

Figure 2.9. Comparative illustration of particle size distribution profiles found by both DLS and MANTA, performed on the same solution of 316L nanoparticles

2.3.6 Powder Bimodality Analysis

The size bimodality of a system of particles can be demonstrated through the parallel representation of the distribution, from a single measurement, as both the number density function and the area density function. The work of Toth *et al.*, [38] showed that for bimodal grain distributions in alloys, there is a large observed difference in the average grain size when the number density function and area density function are considered. This is expected as the smaller particle mode will have a much higher number of particles to occupy the same area as a larger particle mode, while the larger particles will occupy a much larger volume with a much lesser number. The bimodality can then be measured by the difference in the average from the number density function and the average from the area density function. This is demonstrated in Figure 2.10, where the number weighted distribution shows entirely the small mode of particles, which is expected as the total number of small particles counted easily trumps the number of large particles counted. When represented as the volume weighted distribution the opposite effect occurs, where only the large particle mode manifests. The average particle size values obtained from the number density function and area density function are 130nm and 30µm, respectively. The very large difference in the average values obtained from the same data set demonstrates that the powder is indeed a bimodal distribution with a small mode near 130nm and a large mode near 30µm.

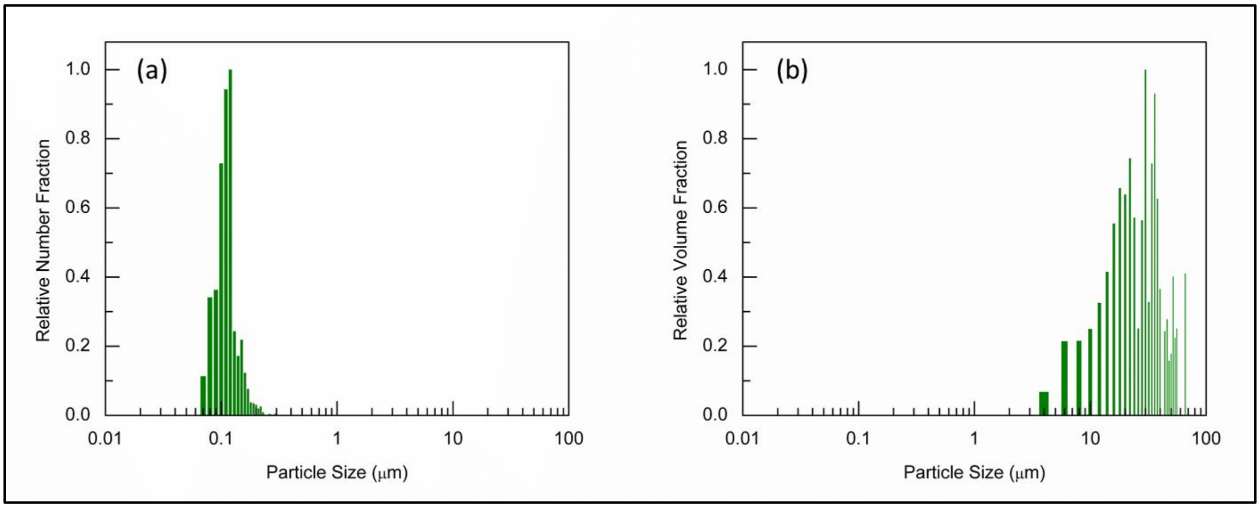

Figure 2.10. A comparison of the particle size distribution plotted as (a) the relative number fraction and (b) the relative volume fraction, which demonstrates the bimodality of the powder.

2.3.7 Multispectral Advanced Nanoparticle Tracking Analysis

Figure 2.11 features particle size distributions of varying capacitance for both ethanol and liquid nitrogen found by MANTA. For ethanol, the mode average of particle size detected was found to be 100nm, 110nm, 130nm, and 150nm for 60µF, 80µF, 100µF, and 120µF, respectively. Results of particle size for the small mode show similar sizes to the crystallite size obtained from Williamson-Hall analysis in XRD, indicating that the size of coherent scattering domains is on the same order of the particle size, so it can be concluded that the smaller particles are largely single crystals. For liquid nitrogen, the mode average particle size detected was found to be 170nm, 190nm, 210nm, and 290nm for 60µF, 80µF, 100µF, and 120µF, respectively. Evidently, both dielectrics exhibited indisputable increases in the average particle size produced as the capacitance was increased. This agrees well with the previous finding that a higher capacitance leads to higher energy and more sustained sparks. As the energy of the spark increases, larger portions of the surface are vaporized. This leads to a higher volume of available vapor and allows for more significant growth of individually nucleated particles. The increased spark time permits a longer growth phase of the nucleated particles, which is likely to be the cause of the slightly increased overall particle mode average as the capacitance setting increases. Conversely, when the spark energy and time are lowered, a smaller portion of the surface is vaporized which, when ejected, has a lower volume and shorter time to condense and thereby forms smaller particles. Future work using plasma spectroscopy methods could confirm this proposed explanation. It is also observed that as the capacitance increases there is a distinct increase in the width of the distribution, particularly about the right-sided, larger particle tail. This is believed to be the result of higher energy plasma channels leading to larger areas of superheated sample surface that are non-uniform. The liquid and vapor ejection occurring during spark erosion leave a surface full of craters and non-uniform surface topology. Thus, as the area of the superheated region increases, there is a higher chance of non-uniform heating and vapor ejection.

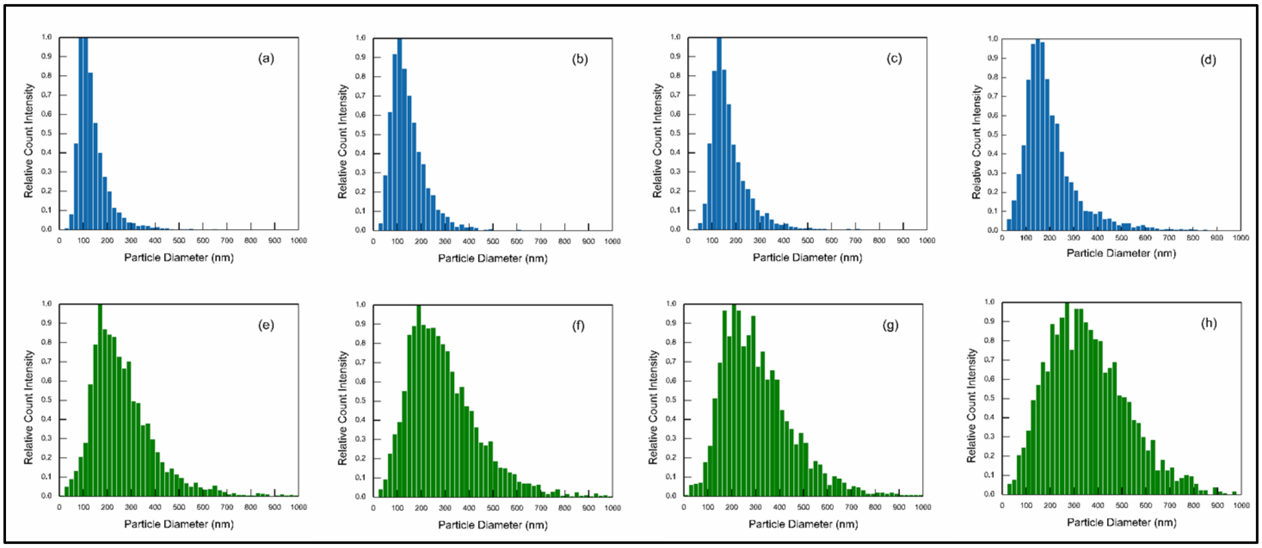

Figure 2.11. Plots of particle size distributions found with MANTA using either (a-d) ethanol or (e-h) liquid N2 as the dielectric. Capacitance values were set to: (a, e) 60µF, (b, f) 80µF, (c, g) 100µF, or (d, h) 120µF.

Upon comparison, regardless of the capacitance, ethanol produces a smaller average particle size as well as a narrower particle size distribution. Considering that, as discussed, particle formation is heavily affected by spark distance, plasma temperature, plasma composition, shock wave propagation, and several other variables that cannot be accounted for in the current study, development of a conjecture on the exact mechanisms of the varying produced particle size is a difficult task. Nonetheless, there are obvious differences between the two fluids, when considering simple quenching of metals, that are likely to cause the particle nucleation and growth kinetics to differ - the temperature and the boiling point. Although there is a large difference in initial temperature of the dielectrics, unlike quenching, in the spark erosion process the temperature within the spark is estimated to reach upwards of 10^4K, which makes the initial temperature of the dielectric fluid a negligible factor when considering the particle formation that happens in this environment. Further, as temperature is a state function, the initial state of the dielectric is expected to have little effect on the solidification kinetics, which happen following the superheating breakdown. The boiling point, however, is expected to influence the formation of the particles. When considering the process following the spark, where particles are condensing and quenching within the high-pressure environment, the boiling points of -195.8°C and 78.4 °C for liquid nitrogen and ethanol, respectively, are very different. It is known that the low boiling point of liquid nitrogen makes it a slow quenching medium due to the large gas jacket that prevents contact with the liquid. This could explain the difference in particle size – the low boiling point of the nitrogen allows for the gas jacket to remain for a longer duration, thus allowing for a longer growth phase of the particles [39]. Vapor condensation of superheated surface material, the driving mechanism for the submicron particle formation, could be better understood after analyzing the sparking and shock wave processes. If the heating and ejection processes are well-defined, then the condensation process could possibly be modeled as heterogeneous nucleation in an atmospheric aerosol.

2.3.8 Spark Discharge Modeling

In addition, an effort was made to provide an analytical model of the spark discharge mechanism. While the spark erosion mechanism is an extraordinarily complex process, which involves the combination of thermodynamic, electrodynamic, hydrodynamic, and electromagnetic factors, a basic simulation of the discharge may assist in understanding trends found in the synthesized nanoparticle size [40]. In this study, a Gaussian heat input model often used to simulate EDM plasma was adapted to estimate the heat flux from the spark erosion plasma [40–42]. The heat flux in the Gaussian heat distribution is given by Equation (2) as follows:

$$q_f(R) = \frac{4.45\, W_M I\, V}{\pi \left(r_{sp}\right)^2} \times e^{\left[-4.5\left(\frac{R}{r_{sp}}\right)^2\right]} \tag{2}$$

where q_f is the heat flux into the material (W/mm^2), W_M is the fraction of the energy utilized by the material (W), I is the pulse current (Amp), V is the pulse voltage (Volts), R is the radial distance from the axis of the spark (μm), and r_{sp} is the spark radius (μm). Current (I) and voltage (V) parameters were extracted from spark discharge waveforms and equipment measurements. Following the approach taken by Abdulkareem *et al.*, [40] if one is only concerned with the heat flux into the surface of the material, then the spark radius can be expressed as a function of the pulse time [40]. Equation (3) represents the expression used for spark radius.

$$r_{sp} = \sqrt{\frac{4.45}{\pi\, t_{on}}} \tag{3}$$

where t_{on} is the duration of the pulse (μs). The t_{on} values used here were determined through the discharge waveforms. Due to the inherent randomness of the system, several assumptions were made to construct this model: (1) the radial distance R from the axis of the spark is set to 0.2μm; (2) the total power of each pulse is used by one spark; (3) the heat transfer to the target surface is axisymmetric; (4) the heat transfer to the sample is done by conduction; (5) there is constant heat flux to the electrode during the pulse; and (6) the fraction of energy utilized by the material was set to W_M=0.1. The W_M value was chosen to be lower than common W_M variables in EDM modeling (W_M=0.17-0.20), because the efficiency of discharge in the spark erosion system is likely diminished due to the variable, and often non-ideal, breakdown conditions [40–42]. The surface temperature of the material was computed through the use of Equation (4), once the total heat flux into the surface of the material had been found.

$$q_{conv} = \mathrm{k}\,\Delta T \tag{4}$$

where q_{conv} is equivalent to the heat flux into the material (W/mm^2), K is the heat transfer coefficient (W/mm^2-°C) [40]. The internal temperature of the target can be found by combining

Equation (5), and Equation (6), which account for the thermal diffusivity and temperature change due to thermal diffusion, respectively.

$$\alpha = \frac{k}{\rho C_p} \tag{5}$$

$$T_{Surface} = T_{Internal} + \alpha \Delta z \tag{6}$$

where α is the thermal diffusivity of the target (mm^2/s), ρ is the density of the target (g/mm^3), C_p is the specific heat capacity (J/g-°C), and Δz is the depth of penetration (mm). In the present study, these parameters were set to $C_p = 452 \times 10^3$J/g-°C, $\rho = 7.95 \times 10^{-3}$g/mm^3, and k = 14W/m-°C. The depth of penetration was adjusted for the energy lost due to the heat of vaporization, which was set to $L_v = 6.8 \times 10^3$kJ/kg.

Figure 2.12(a) shows the results of modeling the depth of vaporization of the 316L targets during spark erosion at various capacitance settings and dielectrics. For juxtaposition, Figure 2.12(b) illustrates the average nanoparticle size measured at varying capacitance values using either liquid nitrogen or ethanol as the dielectric. The simulation of the volume of target material vaporized agrees well with the experimentally obtained results. It should be expected that as the energy parameters permit higher energy sparks, the amount of surface material vaporized will commensurately increase, as observed here. It should be noted that the mechanism of high throughput spark erosion is chaotic by nature, and this representation is by no means an accurate quantitative analysis, but rather, it serves to provide a theoretical basis for the observed trend.

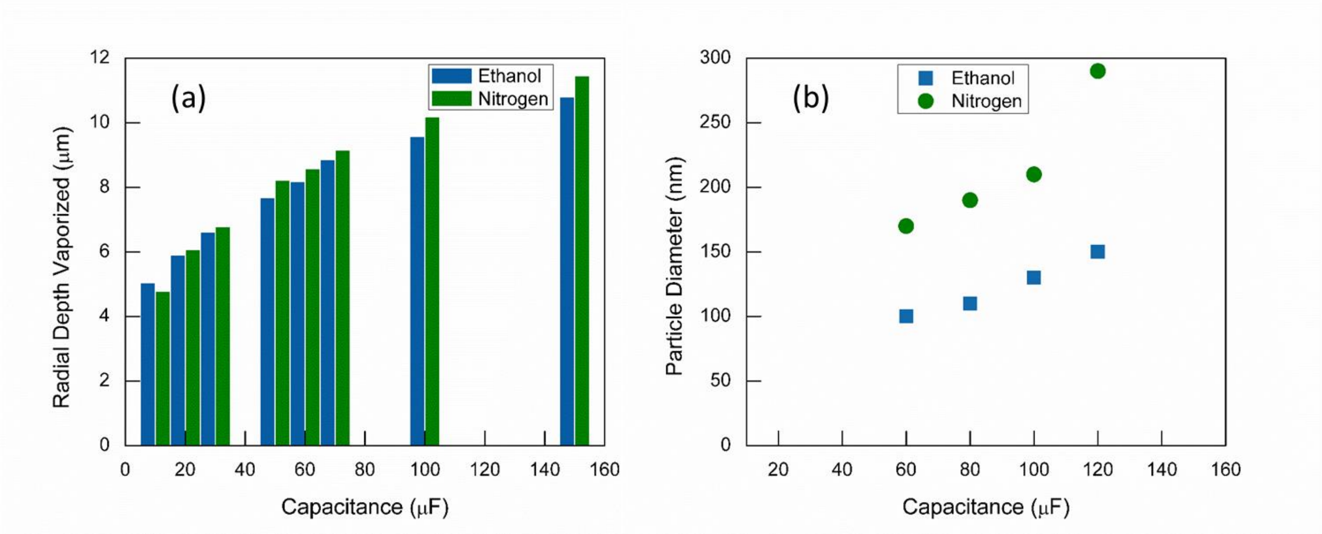

Figure 2.12. (a) Results of the simulated radial depth of vaporization for the 316L targets with varying capacitance settings, and (b) the average measured nanoparticle size for 316L spark erosion run at varying capacitances, for either liquid nitrogen or ethanol as the dielectric.

The shock wave phenomenon during the spark erosion process is a crucial step in understanding nanoparticle formation. Typically, between 15-25% of the breakdown energy is lost to the shock wave and bubble formation, while the remaining 75-85% is transformed into heat [43]. During the plasma breakdown, the development of the primary wave, reflected wave, refraction wave, and head wave create a complex acoustic system [43]. The breakdown geometry, dielectric, and input energy all influence the propagation of the high-pressure wave components in the spark erosion system. The initial shock wave front is responsible for the creation of the gaseous plasma channel that mediates the majority of the target surface heating. The collapse of the high-pressure plasma channel, likewise, contributes to the ejection of the superheated material. By assuming an adiabatic process and small temperature changes, the pressure of the initial wave front can be expressed using a modified Tait equation as in Equation (8) [43,44].

$$p_s = (p_i + B)\left(\frac{2nu_s^2}{(n+1)c_o^2} - \frac{n-1}{n+1}\right) - B \tag{8}$$

where p_s is the pressure of the shock wave front (MPa), p_i is the hydrostatic pressure (0.101MPa), c_o is the sound velocity in the dielectric of interest (m/s), u_s is speed of the wavefront (m/s), and B and n are liquid specific constants based on the permittivity dependence on pressure. To the best of these authors' knowledge, B and n have not been experimentally determined, and thus, the values determined for cyclohexane were used in their place due to the relative similarities of liquid density and sound velocity. For liquid nitrogen, n = 17.9, B = 3.7MPa, and c_o = 558m/s. For ethanol, n = 10.7, B = 121.8MPa, and c_o = 1144m/s [43]. The initial speed of the wavefront during its supersonic development (first few ns) can be approximated using the approach from Jomni *et al*. [43]. For t=0, the extrapolated pressures were p_s = ~400MPa for ethanol and p_s = ~15MPa for liquid nitrogen. Here, the increased pressure experienced in the ethanol could possibly contribute to a more intense collapse of the column and a higher degree of refinement of the ejected vapor.

2.4 Conclusion

A target morphology study employing rectangular, "platelet," and spherical target shapes has determined that the "shaker-pot" spark erosion apparatus runs most efficiently with equiaxed targets due to packing effects, in agreement with the findings of Berkowitz *et al.* [3]. The capacitance to achieve the most efficient spark energy and time, and therefore the highest sustained spark rate for the maximum yield of powder was found to be between 60µF and 80µF. The powder produced during spark erosion is generally spherical, and the particle size distribution was determined to include two modes of powder size. The smaller mode having an average size of ~150nm as determined by DLS and MANTA analysis with similar sized coherent scattering domains from XRD, and the larger mode between 10µm and 50µm from SEM analysis. Both capacitance and liquid dielectric were found to have a strong influence on the small mode size average and overall synthesized particle size distribution. Higher capacitances undoubtedly lead to larger average particle sizes but also increased the width of the size distribution. Ethanol, as opposed to liquid nitrogen, was found to produce smaller average particle sizes with a narrower distribution. This phenomenon was supported by initial modeling of the heat discharge into the superheated region of the target material. The "shaker-pot" spark erosion system has been confirmed to be an effective method of direct production of bimodal nanostructured powders for use in powder metallurgical techniques to fabricate bulk nanostructured parts for use in structural applications. Future work with analysis techniques such as plasma spectroscopy and Schlieren imaging may be valuable in furthering the understanding of the sparking and consolidation processes.

2.5 Acknowledgements

Part 2, is a modified reprint of material that appears in Powder Technology, 2018, Harrington, Tyler; McElfresh, Cameron; Vecchio, Kenneth. The thesis author was the primary investigator and author of this material. Special thanks to Dr. Kuba Tatarkiewicz and Rick Cooper of MANTA Instruments as well as Dr. George Tynan for sharing your expertise.

2.6 References

[1] J.L. Walter, Fine Powders by Spark Erosion, JOM. **39** (1987) 60–60. doi:10.1007/BF03258618.

[2] P.K. Nguyen, K.H. Lee, J. Moon, S.I. Kim, K.A. Ahn, L.H. Chen, S.M. Lee, R.K. Chen, S. Jin, A.E. Berkowitz, Spark erosion: a high production rate method for producing $Bi_{0.5}$ $Sb_{1.5}$ Te_{3} nanoparticles with enhanced thermoelectric performance, Nanotechnology. **23** (2012) 415604. doi:10.1088/0957-4484/23/41/415604.

[3] A.. Berkowitz, M.. Hansen, F.. Parker, K.. Vecchio, F.. Spada, E.. Lavernia, R. Rodriguez, Amorphous soft magnetic particles produced by spark erosion, J. Magn. Magn. Mater. **254** (2003) 1–6. doi:10.1016/S0304-8853(02)00932-0.

[4] A.E. Berkowitz, H. Harper, D.J. Smith, H. Hu, Q. Jiang, V.C. Solomon, H.B. Radousky, Hollow metallic microspheres produced by spark erosion, Appl. Phys. Lett. **85** (2004) 940–942. doi:10.1063/1.1779962.

[5] M.S. Hsu, M.A. Meyers, A. Berkowitz, Synthesis of nanocrystalline titanium carbide by spark erosion, Scr. Metall. Mater. **32** (1995) 805–808. doi:10.1016/0956-716X(95)93205-I.

[6] W. Zhang, A. Farooq, W. Wang, Generating Silicon Nanoparticles Using Spark Erosion by Flushing High-Pressure Deionized Water, Mater. Manuf. Process. **31** (2016) 113–118. doi:10.1080/10426914.2014.984199.

[7] T.V. Pfeiffer, J. Feng, A. Schmidt-Ott, New developments in spark production of nanoparticles, Adv. Powder Technol. **25** (2014) 56–70. doi:10.1016/J.APT.2013.12.005.

[8] K. Albinski, K. Musiol, A. Miernikiewicz, S. Labuz, M. Malota, The temperature of a plasma used in electrical discharge machining, Plasma Sources Sci. Technol. **5** (1996) 736–742. doi:10.1088/0963-0252/5/4/015.

[9] H. Tsuchiya, T. Inoue, Y. Mori, No Title, in: J.R. Crookall (Ed.), Proc. Seventh Int. Conf. Electromachining, North-Holland, Amsterdam, 1983: p. 107.

[10] A. Descoeudres, C. Hollenstein, G. Wälder, R. Perez, Time-resolved imaging and spatially-resolved spectroscopy of electrical discharge machining plasma, J. Phys. D Appl. Phys. **38** (2005) 4066–4073. doi:10.1088/0022-3727/38/22/009.

[11] G.C.H. R.W. Siegel, G.E. Fougere, Nanophase Materials: Synthesis - Properties - Applications - Google Books, Kluwer Academic Publishers, Dordrecht, 1994. https://books.google.com/books?hl=en&lr=&id=b6TnCAAAQBAJ&oi=fnd&pg=PR13&dq=nanophase+materials+siegel&ots=LD6RT5fL3t&sig=kUcux3qcT4MZEPJq4nRh1I0fb0M#v=onepage&q=nanophase materials siegel&f=false (accessed April 5, 2017).

[12] J. Carrey, H.B. Radousky, A.E. Berkowitz, Spark-eroded particles: Influence of processing parameters, J. Appl. Phys. **95** (2004) 823–829. doi:10.1063/1.1635973.

[13] R.H. Kodama, A.E. Nash, F.E. Spada, A.E. Berkowitz, Spark Erosion for Production of Nanocrystalline Materials, in: Nanophase Mater., Springer Netherlands, Dordrecht, 1994: pp. 101–108. doi:10.1007/978-94-011-1076-1_14.

[14] S. Martin, R. Parekh, M. Guessasma, J. Léchelle, J. Fortin, K. Saleh, Study of the sintering kinetics of bimodal powders. A parametric DEM study, (2015). doi:10.1016/j.powtec.2014.03.057.

[15] M.E. Sotomayor, A. Várez, B. Levenfeld, Influence of powder particle size distribution on rheological properties of 316 L powder injection moulding feedstocks, Powder Technol. **200** (2010) 30–36. doi:10.1016/j.powtec.2010.02.003.

[16] J.W. Oh, S.K. Ryu, W.S. Lee, S.J. Park, Analysis of compaction and sintering behavior of 316L stainless steel nano/micro bimodal powder, Powder Technol. **322** (2017) 1–8. doi:10.1016/J.POWTEC.2017.08.055.

[17] L. Zhu, S. Shi, K. Lu, J. Lu, A statistical model for predicting the mechanical properties of nanostructured metals with bimodal grain size distribution, Acta Mater. **60** (2012) 5762–5772. doi:10.1016/j.actamat.2012.06.059.

[18] L. Zhu, J. Lu, Modelling the plastic deformation of nanostructured metals with bimodal grain size distribution, Int. J. Plast. **30** (2012) 166–184. doi:10.1016/j.ijplas.2011.10.003.

[19] D. Witkin, Z. Lee, R. Rodriguez, S. Nutt, E. Lavernia, Al–Mg alloy engineered with bimodal grain size for high strength and increased ductility, Scr. Mater. **49** (2003) 297–302. doi:10.1016/S1359-6462(03)00283-5.

[20] B.O. Han, E.J. Lavernia, Z. Lee, S. Nutt, D. Witkin, Deformation behavior of bimodal nanostructured 5083 Al alloys, Metall. Mater. Trans. A. **36** (2005) 957–965. doi:10.1007/s11661-005-0289-7.

[21] G.J. Fan, H. Choo, P.K. Liaw, E.J. Lavernia, Plastic deformation and fracture of ultrafine-grained Al–Mg alloys with a bimodal grain size distribution, Acta Mater. **54** (2006) 1759–1766. doi:10.1016/j.actamat.2005.11.044.

[22] T.S. Wang, F.C. Zhang, M. Zhang, B. Lv, A novel process to obtain ultrafine-grained low carbon steel with bimodal grain size distribution for potentially improving ductility, Mater. Sci. Eng. A. **485** (2008) 456–460. doi:10.1016/j.msea.2007.09.026.

[23] Z. Lee, V. Radmilovic, B. Ahn, E.J. Lavernia, S.R. Nutt, Tensile Deformation and Fracture Mechanism of Bulk Bimodal Ultrafine-Grained Al-Mg Alloy, Metall. Mater. Trans. A. **41** (2010) 795–801. doi:10.1007/s11661-009-0007-y.

[24] F.T. Parker, F.E. Spada, A.E. Berkowitz, K.S. Vecchio, E.J. Lavernia, R. Rodriguez, Thick amorphous ferromagnetic coatings via thermal spraying of spark-eroded powder, (2001). doi:10.1016/S0167-577X(00)00300-1.

[25] N.S. Tabrizi, Q. Xu, N.M. van der Pers, U. Lafont, A. Schmidt-Ott, Synthesis of mixed metallic nanoparticles by spark discharge, J. Nanoparticle Res. **11** (2009) 1209–1218. doi:10.1007/s11051-008-9568-8.

[26] I.A. Bucklow, L.E. Drain, Spark erosion in liquid argon, J. Sci. Instruments J. SCI. INSTRUM. (1964). http://iopscience.iop.org/article/10.1088/0950-7671/41/10/308/pdf (accessed November 17, 2017).

[27] G.. Williamson, W.. Hall, X-ray line broadening from filed aluminium and wolfram, Acta Metall. **1** (1953) 22–31. doi:10.1016/0001-6160(53)90006-6.

[28] B.D. Cullity, Elements of X-ray diffraction, Addison-Wesley Pub. Co., Reading, Mass., 1956.

[29] A.B. Yu, N. Standish, A study of particle size distributions, Powder Technol. **62** (1990)

101–118. doi:10.1016/0032-5910(90)80073-8.

[30] P. Pec, Electrical discharge machining using simple and powder-mixed dielectric : The effect of the electrode area in the surface roughness and topography, **0** (2007) 250–258. doi:10.1016/j.jmatprotec.2007.09.051.

[31] G. Setia, M. Mahardika, M. Hamdi, Y.S. Wong, K. Mitsui, International Journal of Machine Tools & Manufacture Effect of micro-powder suspension and ultrasonic vibration of dielectric fluid in micro-EDM processes — Taguchi approach, **49** (2009) 1035–1041. doi:10.1016/j.ijmachtools.2009.06.014.

[32] J.F. Liu, Y.B. Guo, Modeling of White Layer Formation in Electric Discharge Machining (EDM) by Incorporating Massive Random Discharge Characteristics, Procedia CIRP. **42** (2016) 697–702. doi:10.1016/j.procir.2016.02.304.

[33] A.M. Mahdy, H.I. Anis, Electrode Roughness Effects on the Breakdown of Air-insulated Apparatus I **__** IL **_**, **5** (1998) 612–617.

[34] H. Peng, D. Yu, X. Zhang, S. Wang, Y. Wen, Fabrication of hollow nickel micro-spheres with high degree of hollowness by silicon powder-mixed spark erosion, Int J Mach Tool Manu. **85** (2014). doi:10.1016/j.ijmachtools.2014.06.002.

[35] V.C. Solomon, J.-I. Hong, Y. Tang, A.E. Berkowitz, D.J. Smith, Electron microscopy investigation of spark-eroded Ni–Mn–Ga ferromagnetic shape-memory alloy particles, Scr. Mater. **56** (2007) 593–596. doi:10.1016/j.scriptamat.2006.12.034.

[36] G. Marnier, C. Keller, J. Noudem, E. Hug, Functional properties of a spark plasma sintered ultrafine-grained 316L steel, Mater. Des. **63** (2014) 633–640. doi:10.1016/j.matdes.2014.06.053.

[37] H. Fujiwara, K. Ameyama, Nano-Grain formation in a fully Ferritic Sus 316L austenitic stainless steel produced by Hs-Pm process, Mater. Sci. Forum. **304** (1999) 47–52. https://www.scientific.net/MSF.304-306.47.pdf (accessed December 14, 2017).

[38] L.S. Toth, S. Biswas, C. Gu, B. Beausir, Notes on representing grain size distributions obtained by electron backscatter diffraction, Mater. Charact. **84** (2013) 67–71. doi:10.1016/j.matchar.2013.07.013.

[39] A.E. Berkowitz, J.L. Walter, Spark erosion: A method for producing rapidly quenched fine powders, J. Mater. Res. **2** (1987) 277–288. doi:10.1557/JMR.1987.0277.

[40] S. Abdulkareem, A.A. Khan, Q. Shah, Temperature Distribution in Copper Electrode during Electrical Discharge Machining Process, **9** (2017) 39–43.

[41] D.K. Panda, Study of thermal stresses induced surface damage under growing plasma channel in electro-discharge michining, J. Mater. Process. Technol. **202** (2008) 86–95.

[42] P. Allen, X. Chen, Process simulation of micro electro-discharge machining on molybdenum, J. Mater. Process. Technol. **186** (2007) 346–355.

[43] F. Aitken, F. Jomni, F. Aitken, A. Denat, Experimental investigation of transient pressure waves produced in dielectric liquids Experimental investigation of transient pressure waves, (2000). doi:10.1121/1.428409.

[44] S. Xiao, J.F. Kolb, M.A. Malik, X. Lu, M. Laroussi, S. Member, R.P. Joshi, S. Member, E. Schamiloglu, K.H. Schoenbach, Electrical Breakdown and Dielectric Recovery of Propylene Carbonate, **34** (2006) 1653–1661.

Part 3

Investigation of Liquid Spark Erosion Nanoparticle Fabrication Using High-Speed Imaging and Emission Spectroscopy

3.1 Introduction

Nanomaterials have gained increasing interest in the past decade due to unique properties that occur when component dimensions are confined below 1μm. For instance, metallic nanoparticle grain-refiners enable synthesis of bimodal or graded microstructures that consist of fine-grained regions (<1μm) interspersed in coarse-grained (>10μm) regions. Bimodal microstructures have demonstrated a high degree of both strength and ductility – making them advantageous for military, aerospace, and performance technology applications [1–4]. Magnetic nanoparticles are also of interest for use in biomedical targeting, drug delivery, and contrast-enhanced imaging. Ferromagnetic materials, such as Fe or Fe_2O_3, are of particular interest because external magnetic fields can be used to stimulate drug release or local heating (magnetic hyperthermia) from embedded particles [5–7].

Regardless of the intended application, the smallest confined dimension often determines the functionality of the nanomaterial. As such, there are obvious benefits to understanding mechanisms of tunable nanomaterials synthesis techniques. Submerged shaker-pot spark-erosion is a high-throughput nanoparticle synthesis technique that is versatile, can be applied across various metallic materials, and is tunable through variation of erosion parameters [8–13]. Figure 3.1 is a cross-sectional illustration of a shaker-pot spark erosion setup. The target material is suspended in a non-conductive container that is completely submerged in the dielectric fluid of choice. Liquid nitrogen and ethanol are commonly used dielectrics because they are readily available and inexpensive processing mediums. Electrodes are mounted to the base of the container and then wired to an external capacitor bank. The submerged container is driven by a motor to shake laterally at approximately 20Hz, causing the target material to rapidly come into contact and separate at a high rate. When the gap conditions are met a dielectric breakdown occurs, and an arc discharges between two target pieces (or a target piece and an electrode). The arc liquefies and vaporizes local areas of the target pieces that are then ejected into the surrounding dielectric and immediately quenched, resulting in highly spherical oxidation-free particles in the range of 10nm to 50μm. The arc is believed to reach temperatures upwards of 10^4K and pressures near ~280MPa – though direct measurement has not been performed during the spark erosion process due to the uncontrollable and random nature of the shaker-pot setup [14,15]. Understanding the physical mechanisms of the particle formation is vital for researchers and manufacturers alike to further control the size and properties of synthesized nanoparticles.

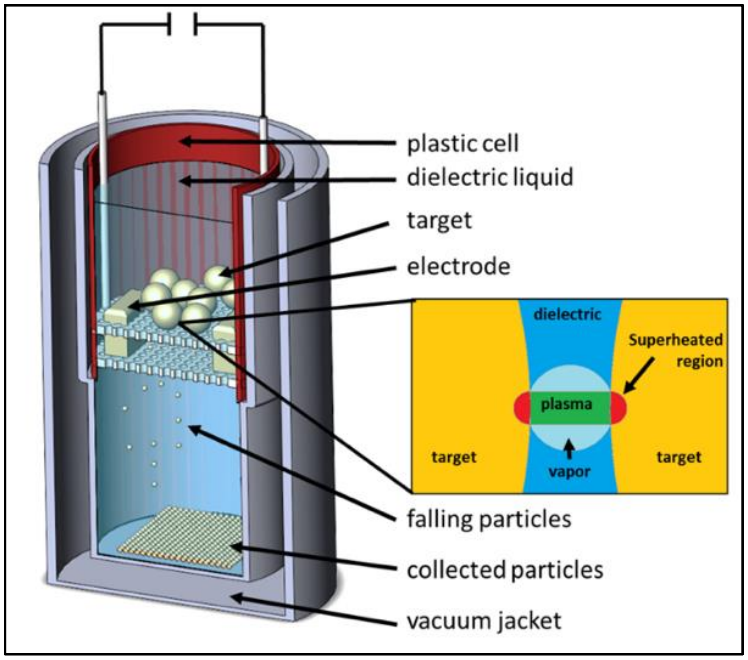

Figure 3.1. Schematic of high-through shaker-pot spark erosion technique. Sample material of interest is shown in gold.

To combat the issue of observability, we constructed a more controlled submerged discharge chamber; a diagram of the chamber is featured in Figure 3.2. One electrode is fixed while the other is attached to a drivable arm. Both target wires, in this case, are mounted to the end of an arm and connected to the same capacitor bank used by Harrington *et al.* [8] The reaction container is filled with a dielectric fluid, then the movable arm is driven until the gap conditions are met and a dielectric breakdown occurs. The electrodes are aligned with a quartz window, so direct observation of the discharge is possible.

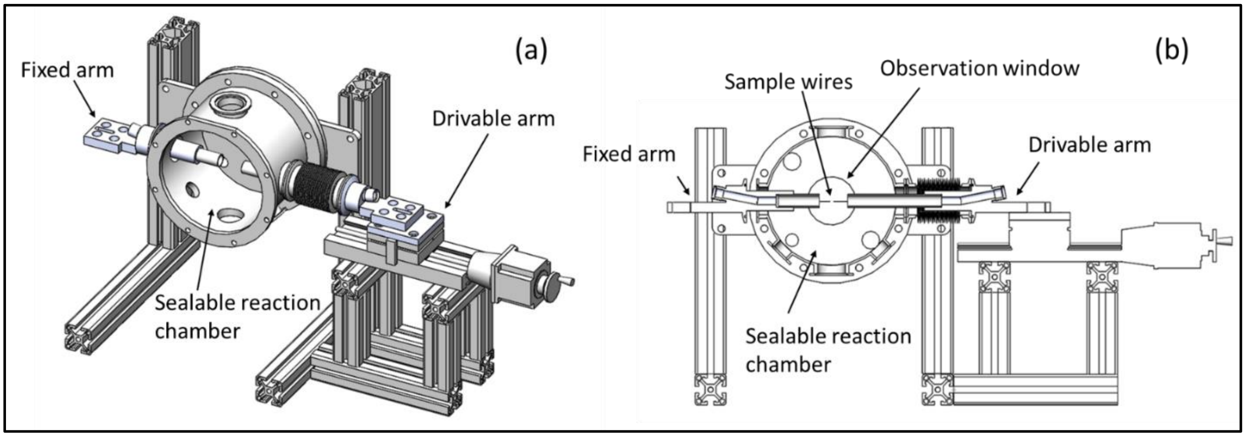

Figure 3.2. (a) Trimetric view of a 3D illustration of the experimental spark discharge setup with the front plate removed and (b) a cross sectional view from the back of the apparatus.

This study uses high-speed imaging and optical emission spectroscopy to investigate submerged discharge characteristics such as temperature, pressure, and plume duration with respect to varying spark erosion capacitance (60μF – 120μF) and liquid dielectric (ethanol/liquid nitrogen) using Fe electrodes. The studied characteristics will be used to investigate how these processing parameters may affect the final synthesized nanoparticle size and distribution with respect to work performed by Harrington *et al.* [8] on spark erosion of 316L stainless steel. Harrington *et al.* [8] demonstrated that increasing the capacitance increased the modal average and size variance of the produced nanoparticles and, similarly, liquid nitrogen produced particles with an increased modal average and size variance when compared to ethanol as a dielectric. Particle size distributions measured at varying capacitance levels with ethanol and liquid nitrogen dielectrics are featured in Figure 3.3(a) and 3(b), respectively. The overall goal of this study is to gain insight that will assist in tuning the processing parameters of spark erosion to fabricate a desired size and distribution of nanoparticles. Extending the current understanding of submerged discharge particle formation is invaluable to its future application as a cheap, versatile, and controllable processing technique.

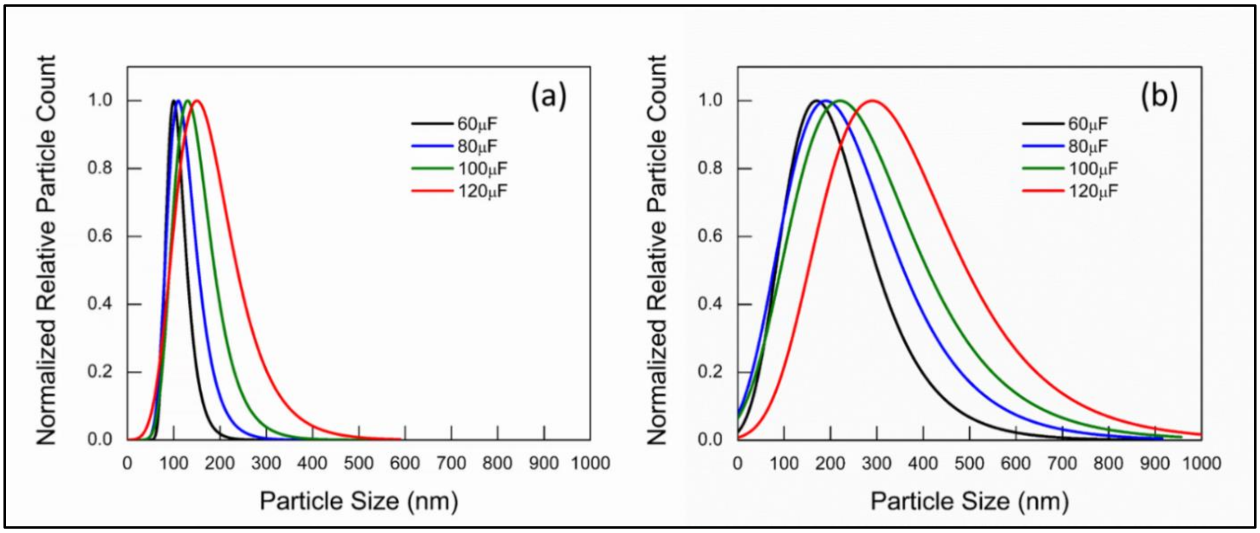

Figure 3.3. Nanoparticle size distributions of 316L particles fabricated by high-throughput spark erosion in (a) ethanol and (b) liquid nitrogen. Reproduced from findings in Harrington *et al*. [8].

3.2 Materials and Methods

Electrodes were made of 0.508mm diameter Fe wire (99.9% purity McMaster Carr, Los Angeles) that were confirmed to be single phase on a Rigaku Rotaflex X-ray diffractometer (XRD) with Cu Kα radiation. Liquid nitrogen or ethanol (99.9% purity) were used as liquid dielectrics. High-speed imaging of the discharge events was captured on a Shimadzu HPV-X2 (Shimadzu Corp., Kyoto) using a PicoScope 4824 (Pico Technology, St Neots) as a trigger, achieving a spatial resolution of approximately 30μm/pixel for all figures. A 25% and 6% neutral density transmittance filter (Olympus Corp., Toyko) were used to optimize image capture quality of the characteristic ejection edge/shock wave. A 513±10nm optical bandpass filter (Edmund Optics, New Jersey) was used to selectively visualize the high-temperature Fe regions of the event from the Fe (I) strong emission peak at 516.74nm, though some other radiation from the event is also able to reach the camera. The radial shock wave propagation was measured using ImageJ software. Emission spectroscopy was captured with an Ocean Optics USB4000-VIS-NIR Spectrometer (Ocean Optics, Florida) with an integration time of 10ms. Spectroscopy and plume expansion/collapse measurement was repeated for dozens of sparks for each dielectric/capacitance combination.

3.2.1 Shock Wave Analysis

The spark discharge plume evolution can be paralleled to the physical mechanism of a concentrated explosion in a homogeneous atmosphere [16–18]. The rapid deposition of energy in a small area facilitates the formation of an expanding gaseous plume and shock wave that propagates through the liquid dielectric. Here, the initial shock can be described using the simple Taylor-Sedov (TS) homogenous expansion blast wave model [16,18,19]. The radial expansion of a TS spherical shock is given in Equation (1):

$$R(t) = \xi \left(\frac{2E_0}{\rho}\right)^{1/5} t^{2/5} \tag{1}$$

here $R(t)$ is the radial distance of the wave, ρ is the density of the surrounding medium, t is the time, and E_o is the initial total energy. The parameter ξ is a material constant that is dependent on the specific heat capacity ratio (γ) and detailed in Equation (2):

$$\xi = \left\{\frac{[75(\gamma-1)\times(\gamma-1)^2]}{16\pi(3\gamma-1)}\right\}^{1/5} \tag{2}$$

Use of the TS model requires the assumptions that: (i) the mass of the background gas is larger than the mass of the ablated material, and (ii) the strength of the shock wave is sufficiently more substantial than the ambient pressure. The TS model reliably describes early and intermediate-stage shock mechanics and has been previously applied to spark discharge and laser ablation [16,18,19]. However, later stages of the shock are often more accurately described by drag-force models. For this study, the drag and late-stage shock phenomena are not pertinent to the mechanisms of interest, therefore this study will focus on the TS model.

The Rankine-Hugoniot (R-H) relations are expressions that conserve energy, mass, and momentum across the boundary of a shock front. Though the internal dynamics of the plasma arc and gas plume are exceedingly complex, the R-H conditions can roughly describe the pressure at the edge of the propagating shock to assist in understanding how overall plume conditions are evolving with respect to changes in the capacitance setting and liquid dielectric. Equation (3) is the R-H expression for the boundary pressure of the shock:

$$P = \left[\frac{\rho U^2}{P_0} - 1\right]\frac{2\gamma P_0}{\gamma+1} + P_0 \tag{3}$$

here U is the velocity of the shock front, P_o is the ambient pressure, and P is the pressure inside the shock front.

3.2.2 Spectroscopy-Temperature Analysis

When the gap conditions are met, a dielectric breakdown occurs between the electrodes and current begins to move across the channel – forming a plasma streamer containing a mixture of high-temperature electrons, gaseous molecules, and ionized species. Plasma channel formation is accompanied by intense light emission from atomic transitions of the molecular and ionic streamer constituents. For a plasma in local thermal equilibrium (LTE), the line intensities of a single atomic species can be used in the Boltzmann plot method to extract the species temperature [20–25]. The electron-temperature Saha-Boltzmann relation is given in Equation (4):

$$\ln\left(\frac{I\lambda}{Ag}\right) = \frac{-E_k}{kT} \tag{4}$$

where I is the total measured intensity of the characteristic emission, λ is the wavelength of characteristic emission, A is the transition probability, g is the upper-level degeneracy, k is the Boltzmann constant, E_k is the upper-level energy, and T is the electron excitation temperature. A set of 5 Fe (I) emission lines were used to construct the Saha-Boltzmann plot in this study [25]. The characteristic emission lines and their relevant mathematical quantities are shown in Table 3.1. It should be emphasized the Fe (I) electron temperature is being used as an approximation of the plasma temperature – although the plasma components are likely not in LTE. The presence of nanometer and micrometer-sized particles creates a "dusty" plasma [26–29]. These suspended particles become charged and greatly alter the gas-ion-electron-dust interactions such that non-equilibrium states are extremely common. The relevance of dusty plasmas in this context will be addressed in the subsequent discussion. Moreover, the high pressure on the gaseous channel, exothermic nature of coalescence, dynamic expansion, and active quenching of the plume suggest that the environment is non-LTE and non-isothermal. More accurate evaluation of the gas/ion temperatures could be established through evaluation of the molecular rotation/vibration temperatures, though this extends beyond the scope of this body of work.

Table 3.1. Fe (I) emission peaks used for construction of Saha-Boltzmann plots.

Wavelength [nm]	E_j [eV]	E_i [eV]	g_j	A_{ij} [10^8 s^{-1}]
370.5	3.4	0.052	7	0.0322
373.2	5.52	2.200	5	0.2800
385.6	3.27	0.051	5	0.0464
386.5	4.22	1.010	3	0.1550
390.2	4.73	1.560	7	0.2140

Emission peaks can be masked or overwhelmed by background radiation from discharges in liquids, making accurate line-ratio measurements impractical [30–34]. Instead, Planck's equation for blackbody radiation can be used to fit the background spectrum and estimate the temperature of the plasma hot zone [30,32,33]. Planck's equation of blackbody radiation is given in Equation (5):

$$B_\lambda(\lambda,T) = \frac{2hc^2}{\lambda^5}\frac{1}{\exp(\frac{hc}{\lambda kT}-1)} \tag{5}$$

where $B_\lambda(\lambda,T)$ is the intensity of blackbody radiation, h is Planck's constant, c is the speed of light, λ is the wavelength of emission, k is the Boltzmann constant, and T is temperature.

3.3 Results and Discussion

3.3.1 Shock Wave Analysis Results

Initial survey imaging found that liquid nitrogen discharges had significantly more intense emission than ethanol discharges. This was observed as overexposure or "whiting out" of the image for a longer duration and masking any visible traits. To compensate for the increased optical emission, a 513±10nm bandpass filter was used to observe the shock front propagations in liquid nitrogen. The results of imaging for radial shock wave tracking in ethanol and liquid nitrogen are shown in Figure 3.4 and 3.5, respectively. Imaging was done at 1000000 frames per second (fps) with an exposure of 500ns. Additional images were taken between 15μs and 150μs using a 6% and 25% neutral density transmittance filter (not shown here) to visualize the shock wave propagation and track early stages of radial progression. The black area in the center of the discharge is a region of oversaturated pixels, likely due to emission from the high-temperature plasma. The outer edge of the initial shock clearly carries away a rim of larger particles that move with its expansion into the surrounding dielectric. Larger particles are then continually ejected from the superheated region after the initial shock. Post-shock wave particle ejections are readily observable between 150-230μs in the 100μF ethanol spark. The formation of these larger particles is not of interest for this study, and future work will address the mechanisms relevant to their synthesis and size. The gaseous plume created around the plasma arc is the near-spherical region of high emission intensity inside the edge of the expanding shock front. The plume expands with shock wave growth and is often observed to be slightly smaller in radial size than the shock front. Eventually, the plume loses its spherical shape as the initial explosive energy is absorbed by the surrounding liquid.

Results of radial shock propagation at varying capacitance are featured in Figure 3.6. The spherical shock propagated faster and further in liquid nitrogen than its counterpart in ethanol for any given capacitance level. Similarly, increasing capacitance increased the speed of the shock front for both liquids. The experimental data were fitted using the Taylor-Sedov expansion model described in Equations (1) and (2). The TS model appropriately fit the experimental data for the early and intermediate-stage shock expansion, though, the later stages in liquid nitrogen are marginally lower than the extrapolated fit. This deviation may be due to drag effects that are more accurately described using viscous force models. The variation is not significant enough to warrant reevaluation using a different model.

The TS shock expansion fit was used to extrapolate shock front pressures using Equation (3). The calculated boundary pressures are shown in Figure 3.7. The initial (maximum) shock front pressures for ethanol were 47MPa, 55MPa, 82MPa, and 99MPa for 60μF, 80μF, 100μF, and 120μF; respectively. The initial (maximum) shock front pressures for liquid nitrogen were 60MPa, 77MPa, 92MPa, and 109MPa for 60μF, 80μF, 100μF, and 120μF; respectively. The rapid decline of boundary pressure is reflective of the slowing of the shock front as the discharge energy is dissipated in the surrounding medium – quantitatively represented by a decrease in the slope of the TS expansion curve with time. The initial shock pressure increased with increasing capacitance for both dielectrics, which can be understood as higher energy discharges correlating to more powerful point-source explosions. It is also possible that increasing the amount of energy released in the discharge leads to higher-temperature plasma streamers, which causes more rapid expansion of the plume.

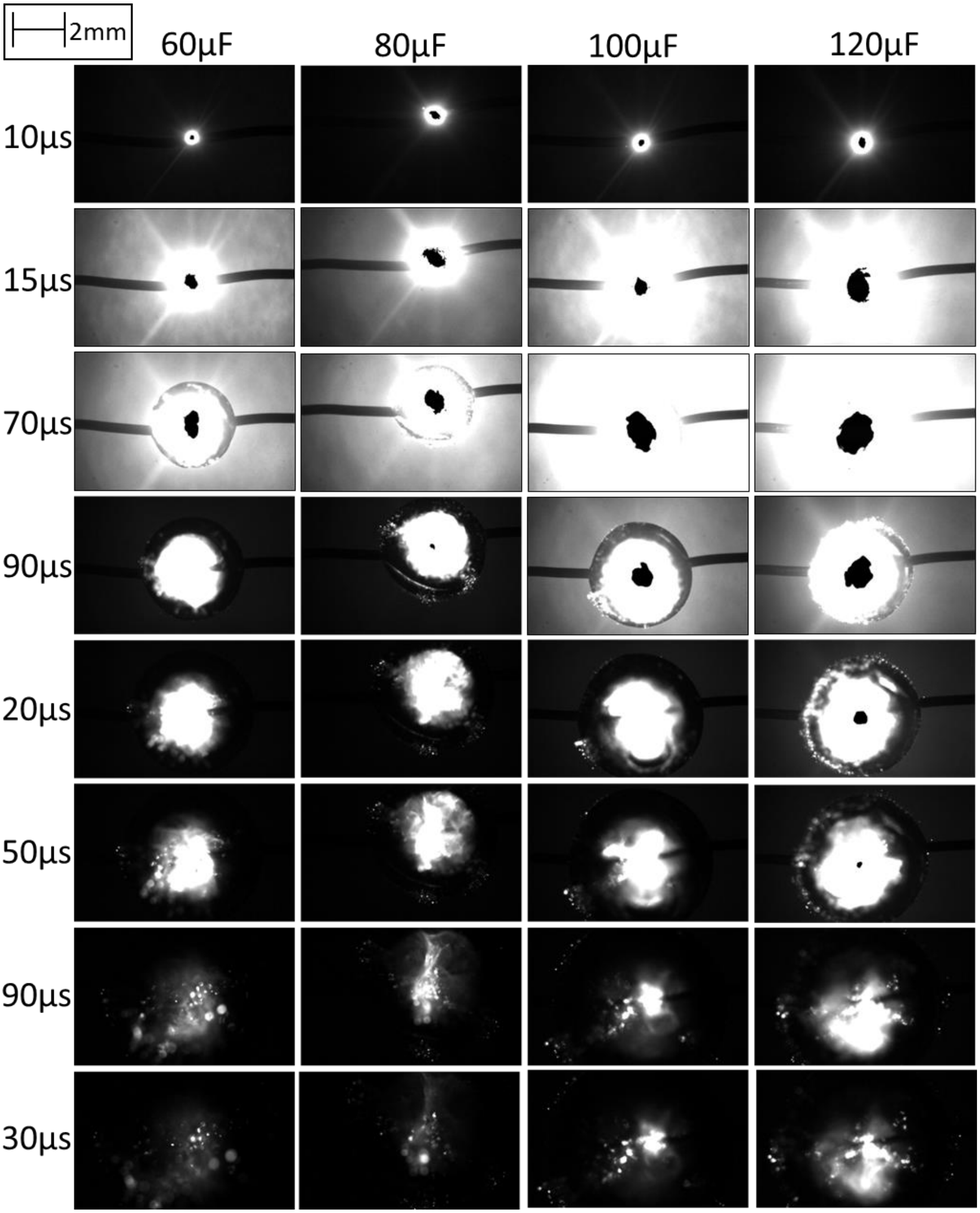

Figure 3.4. Imaging of discharges in ethanol at varied capacitance. Taken at 1000000fps and 500ns exposure.

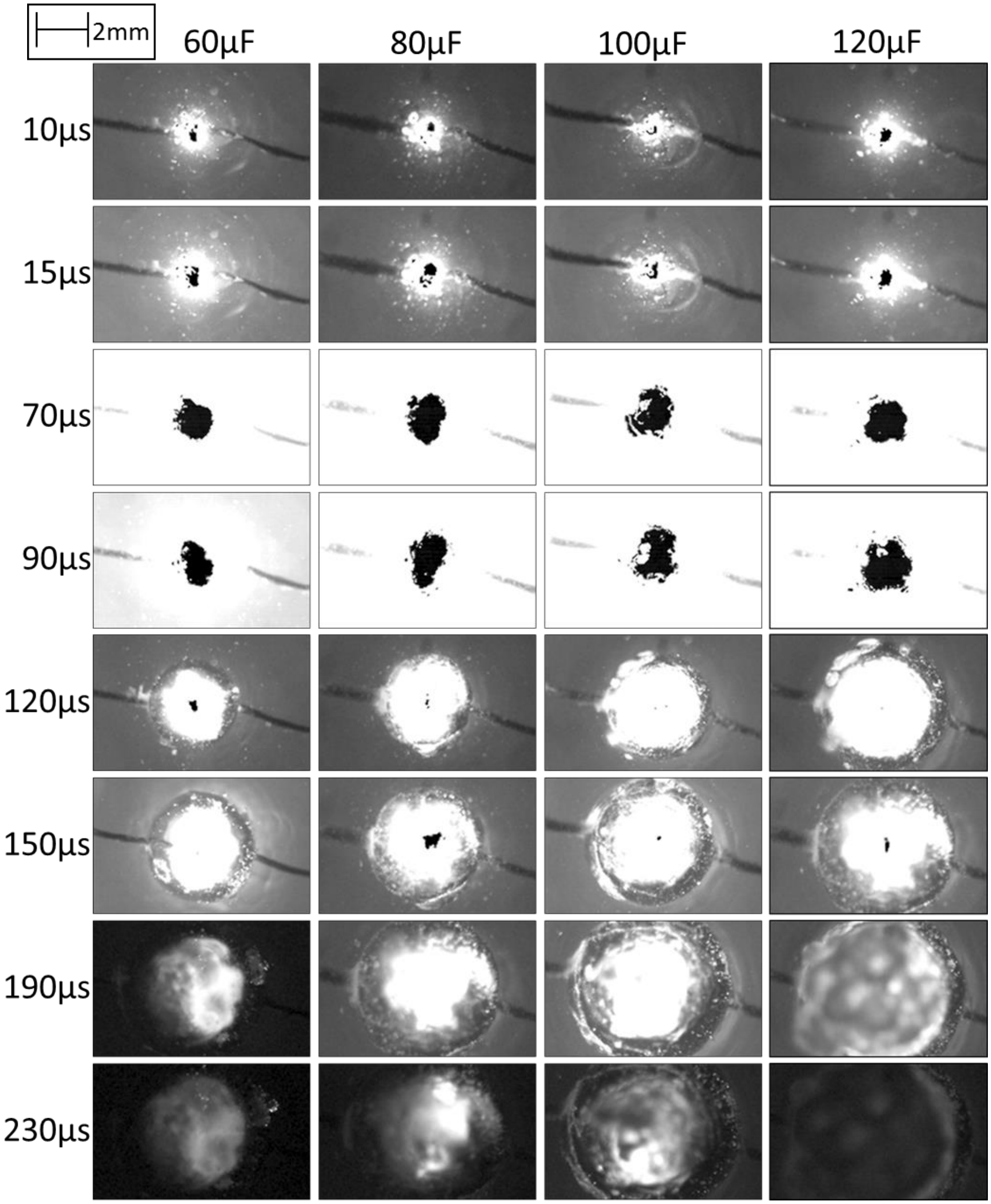

Figure 3.5. Imaging of discharges in liquid nitrogen at varied capacitance. Taken at 1000000fps and 500ns exposure.

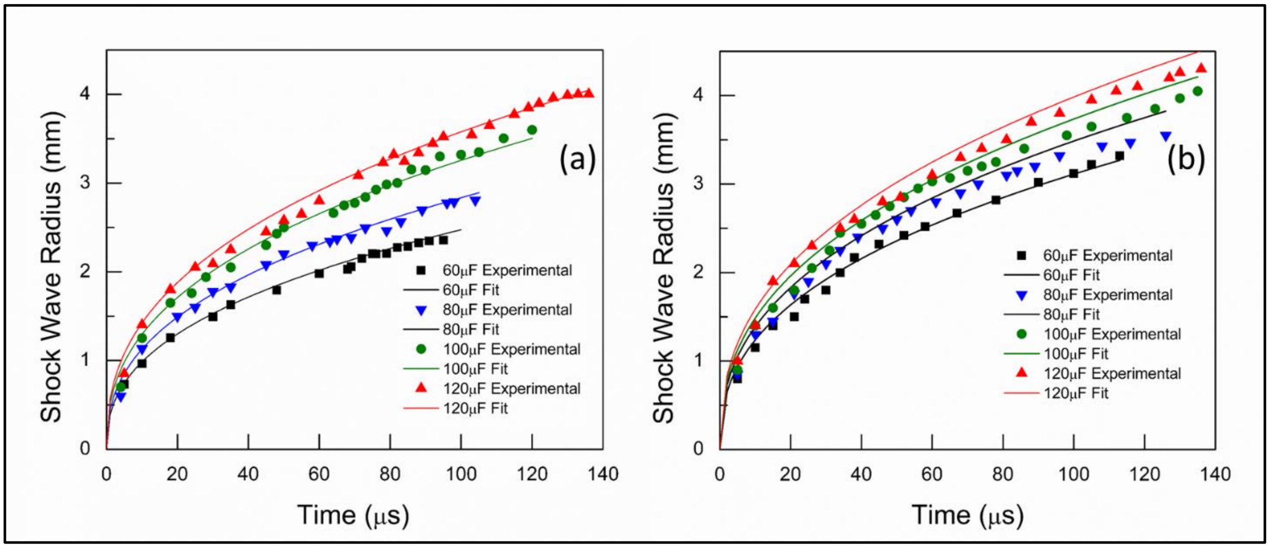

Figure 3.6. Radial shock wave propagation from discharges in (a) ethanol and (b) liquid nitrogen. Experimental data was fit with the Taylor-Sedov expansion model.

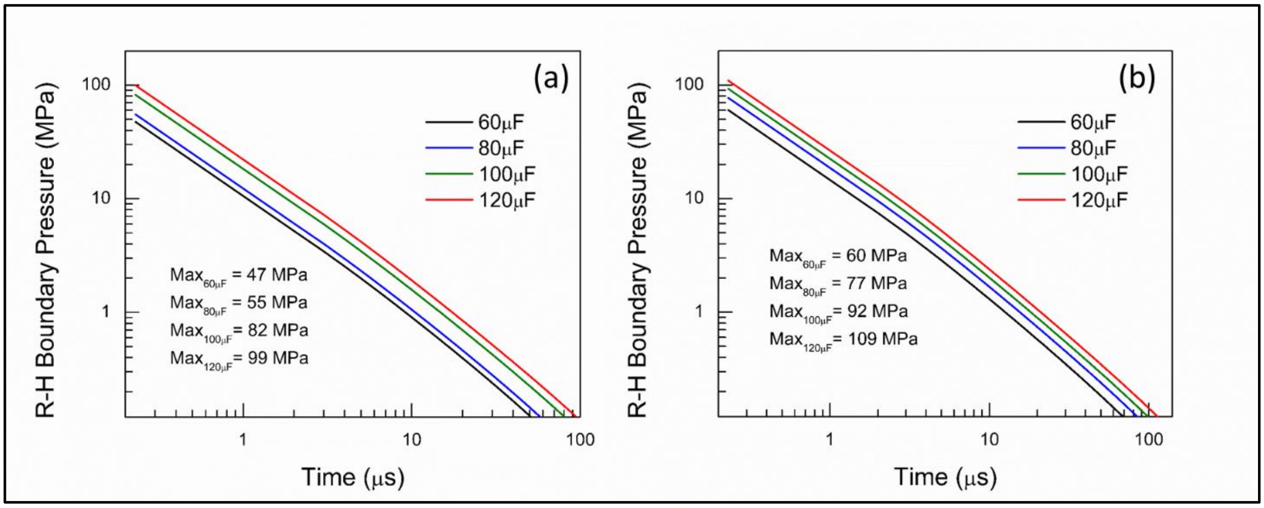

Figure 3.7. Calculated results of the Rankine-Hugoniot shock front boundary pressure in (a) ethanol and (b) liquid nitrogen.

3.3.2 Spectroscopy-Temperature Analysis Results

Typical results of emission spectroscopy for discharges in ethanol and liquid nitrogen are shown in Figure 3.8. Since the spectroscopy integration time (10ms) is significantly longer than the discharge event (~60-300μs) it can be assumed that these profiles are an average of the early, intermediate, and late-stage arc along with any stray radiation that reached the detector. Though plasma characteristics such as species emission intensity and electron temperature significantly evolve throughout a discharge, the spectroscopy technique available did not have the temporal resolution to resolve the progression.

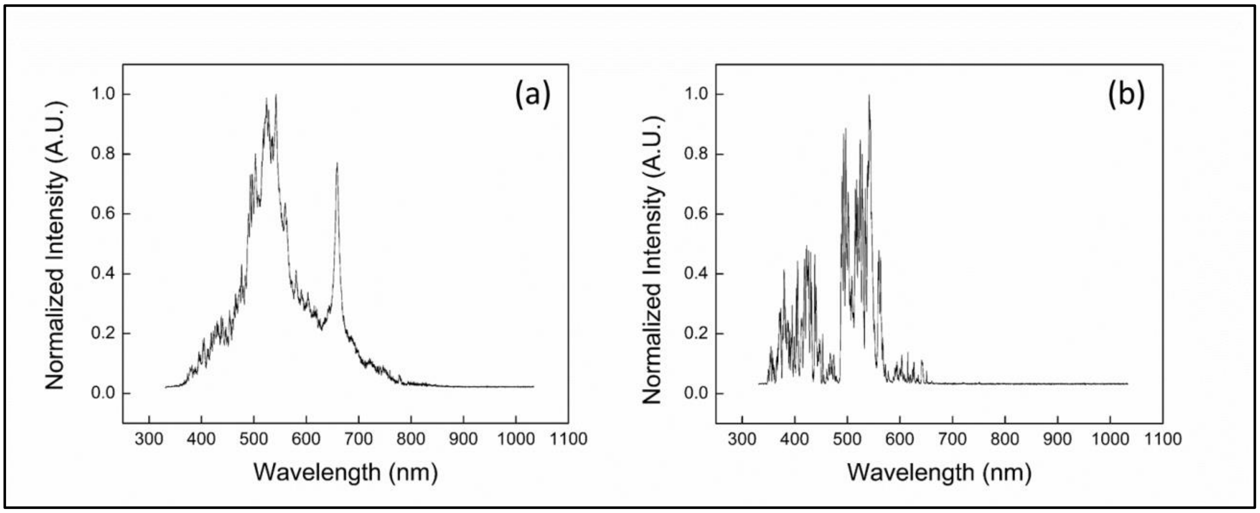

Figure 3.8. Typical results of optical emission spectroscopy of discharges in (a) ethanol and (b) liquid nitrogen. Spectroscopy taken with a 10ms integration time. Capacitance was 100μF for these spectra.

The distinguishable Fe (I) lines listed in Table 3.1 were used to construct the Saha-Boltzmann plots shown in Figure 3.9. The inverse-slope relationship was used to extract species temperatures of 10030K, 11500K, 12100K, and 13000K for 60μF, 80μF, 100μF, and 120μF, respectively.

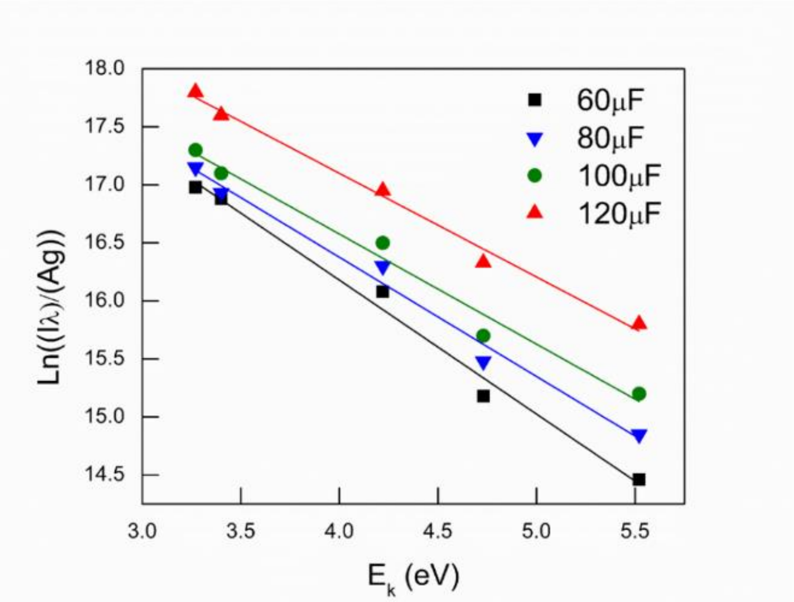

Figure 3.9. Saha-Boltzmann plots of Fe (I) emission species in liquid nitrogen discharges at varied capacitance.

Overlapping or crowded peaks from various radiative species introduced during the decomposition of ethanol complicated deconvolution of the ethanol emission spectrum. Ethanol can decompose by Equation (6) or (7) [35]:

$$C_2H_5OH \rightarrow CO + \frac{5}{2}H_2 + \frac{1}{2}C_2H_2 \tag{6}$$

$$C_2H_5OH \rightarrow CO + 3H_2 + C \tag{7}$$

Further dissociation and recombination ultimately produces a mixture of CO, OH, H_2, O_2^+, CH, C_2, and other assorted ionized byproducts. In a high-temperature environment, these byproducts undergo molecular or atomic transitions from a high energy state to a low energy state and produce radiation that comprises unique emission spectra. Reyes *et al.* [35] characterized the ethanol plasma glow optical emission spectra and categorized distinguishable peaks with their corresponding origin. The highest intensity emitting species were CO, C_2, and most prominently, H. The high intensity of the hydrogen emission is reasonable considering the significant concentration of H_2 that decomposes at increased temperatures. The four wavelengths of hydrogen emission in the visible light spectrum correspond to the Balmer series - a group of well-studied spectral lines often used to quantitatively extract species conditions, such as temperature and electron density. The Balmer series consists of H_α (656.3nm), H_β (486.1nm), H_γ (434.0nm), and H_δ (410.2nm) [36–38]. The observed neutral CO emission originated from transitions within the Angstrom System ($B^1\sum - A^1\prod$) at 451.09nm, 483.53nm, 519.82nm, 561.02nm, 607.99nm, and 662.03nm. The observed C_2 emission originated from transitions in the vibrational energy state of the C-C molecule. As opposed to initiating from electronic transitions within the molecule, as with the Balmer emission spectra, molecular transitions from a high energy vibrational state to a low energy state facilitates the emission of a characteristic radiation spectra. Reyes *et al.* recorded bands within the Swam system ($A^3\prod_g - X'^3\prod_u$) at 449.41nm and 516.52nm [35].

In this study, prominent emission peaks from the CO species in the Angstrom System ($B^1\sum - A^1\prod$) were identified near 519.82nm, 561.02nm, and 607.99nm. A weak band of the C_2 Swam system ($A^3\prod_g - X'^3\prod_u$) is detectable near 449.41nm and the higher wavelength 516.52nm transition, previously found as an emitting species by Reyes *et al.* [35] is indiscernible. The H_α emission peak is prominent near 656nm but H_γ (434.0nm) and H_β (486.1nm) are overwhelmed by background radiation. Due to limited visibility of the characteristic Balmer excitation states, Planck's equation of Blackbody radiation was applied to estimate the temperature of the plasma hot zone. The average calculated plasma temperatures were 5300K, 5500K, 5700K, and 6500K for 60μF, 80μF, 100μF, and 120μF, respectively. Both the liquid nitrogen and ethanol discharge temperature results are on the same magnitude of previous studies on spark discharge mechanics [20,21,33,39].

The mathematically determined temperatures from both the liquid nitrogen and ethanol discharges at varying capacitance levels are plotted in Figure 3.10. Plasma temperatures increased as the capacitance increased for both liquids. Though the discharge temperatures in ethanol are consistently lower than those in liquid nitrogen, it is unclear whether this is due to variance in the calculation method or from the physical characteristics in the spark. In the following discussion, both possibilities are addressed.

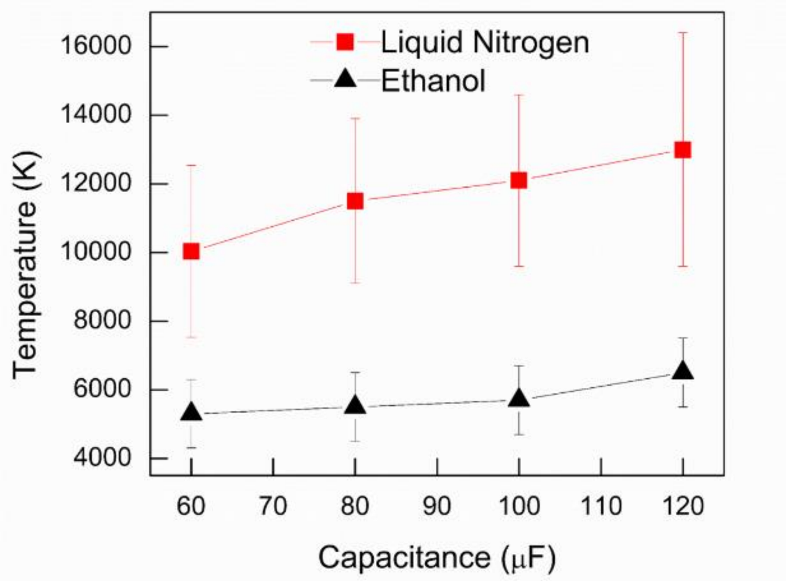

Figure 3.10. Results of temperature approximations for ethanol and liquid nitrogen discharges at varied capacitance levels. The Saha-Boltzmann plot method was used for liquid nitrogen and Planck’s blackbody approximation was used for ethanol.

3.3.3 Visualization of Plume

High-speed imaging was also done at 1000000fps and 500ns exposure using a 25% neutral density transmission filter to examine differences in plume duration. The results are shown in Figure 3.11 for ethanol and Figure 3.12 for liquid nitrogen. Note that different timestamps were used for either dielectric due to contrasting rates of decay. The plume originating from the liquid nitrogen discharge sustains emission for significantly longer than the ethanol discharges at all capacitance levels – suggesting that the high-temperature gaseous nanoparticle-forming region is retained for longer. At any given capacitance, the concentrated vapor region in liquid nitrogen was observed to be sustained for an additional 60-120μs. Plume duration was also observed to increase ~20-30μs per 20μF increase for both dielectrics. This was confirmed by observation of dozens of sparks with all combinations of capacitance and dielectric.

While it is tempting to quantify the plume size, we believe doing so with these experimental conditions would be non-representative of any true physical phenomena. At any given point in time, the temperature, and therefore emission intensity, generally decreases with increasing plume radius. Plume vapor density is also radially non-homogenous. Thus, the furthest radial distance of detectable emissivity may be heavily influenced by the imposed emission intensity threshold. This is further complicated by two non-similar dielectrics that may differ in the degree of variation in emission with respect to temperature. Setting an arbitrary optical emission threshold may lead to different results even if the same physical process is occurring within the liquid systems. A more accurate description of the plume radius could be achieved through spatially resolved high-resolution spectroscopy, which could readily discern variation due to complex temperature profiles.

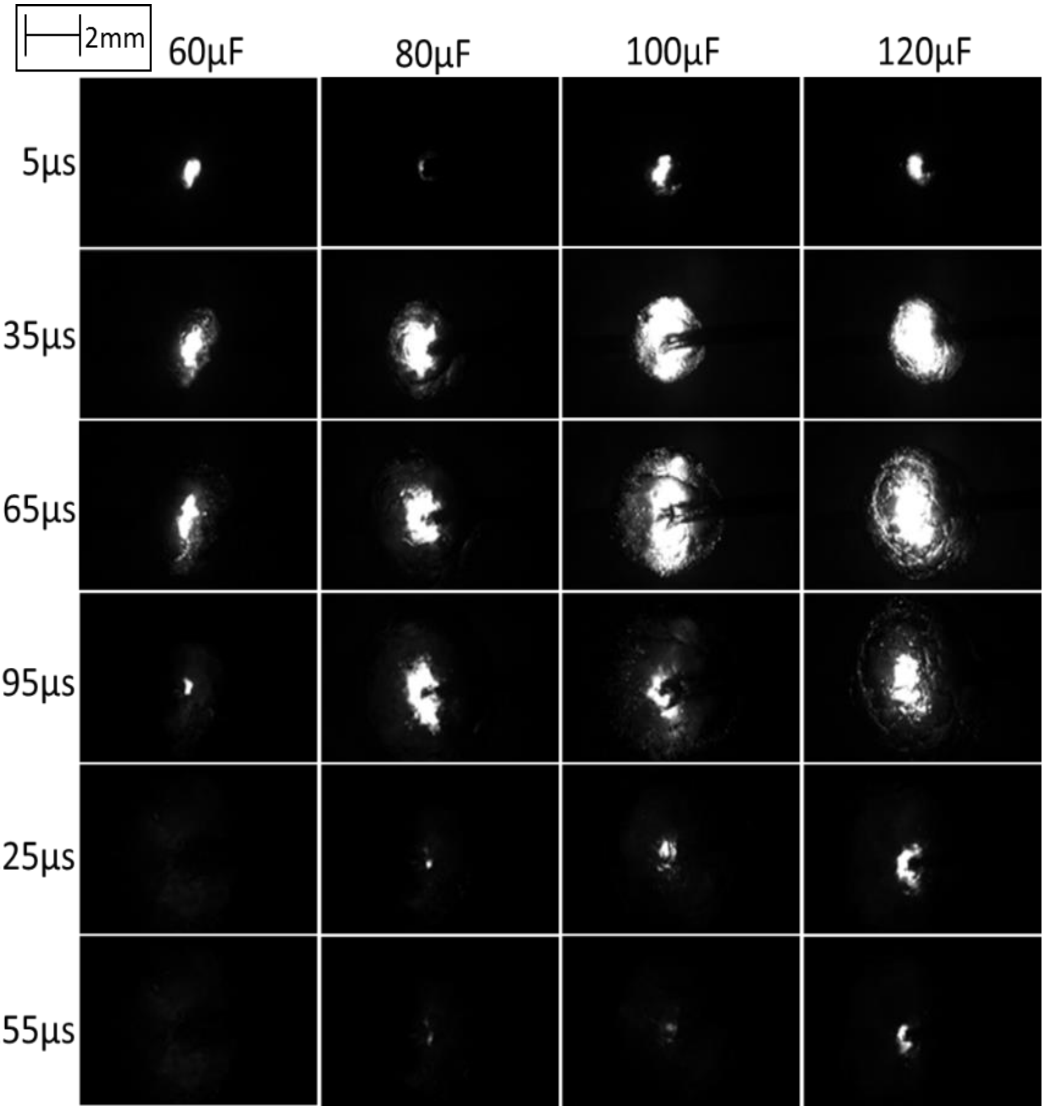

Figure 3.11. Imaging of ethanol discharges at varied capacitance levels. Images taken at 1000000fps and 500ns exposure with a 25% neutral density transmission filter.

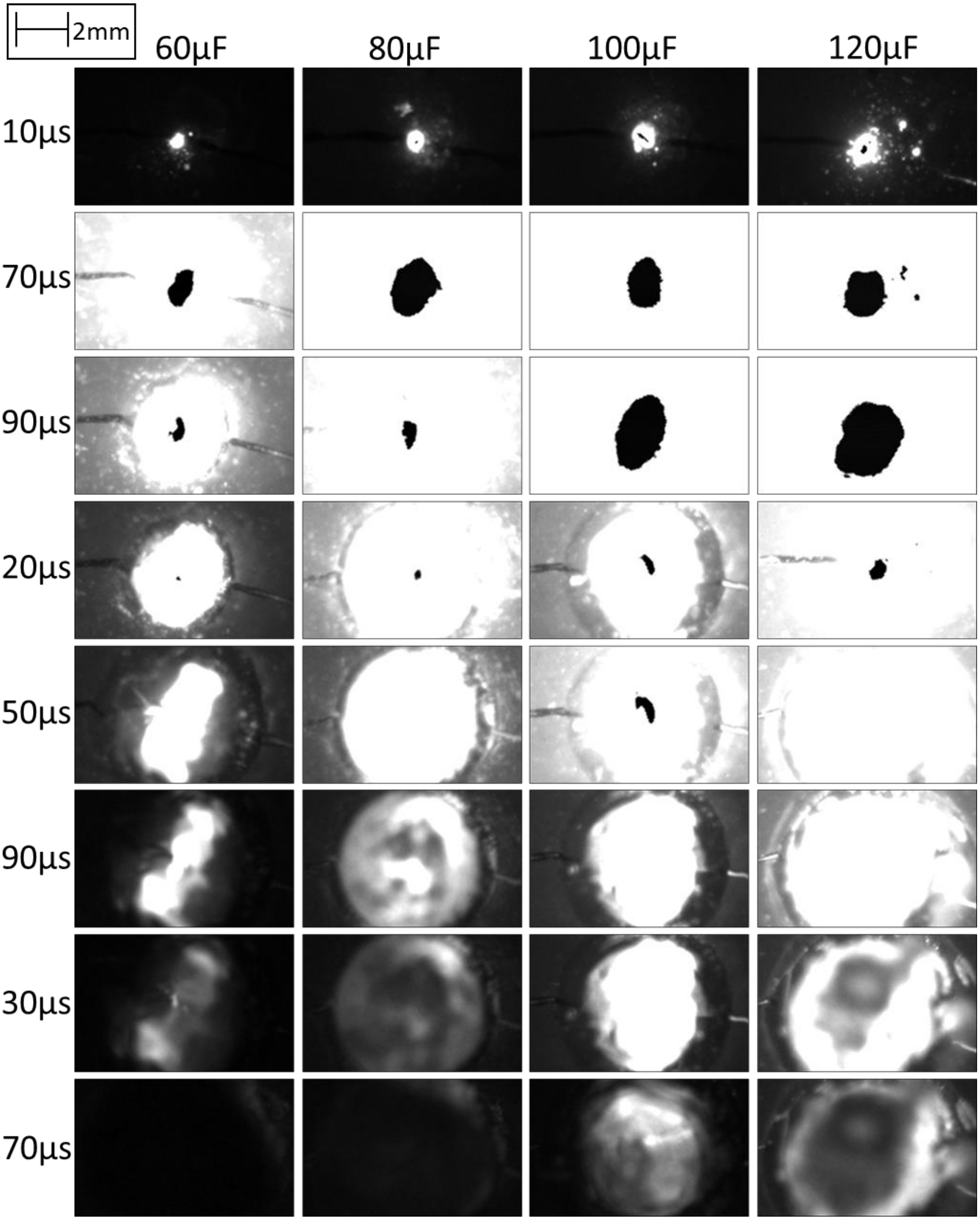

Figure 3.12. Imaging of liquid nitrogen discharges at varied capacitance levels. Images taken at 1000000fps and 500ns exposure with a 25% neutral density transmission filter.

3.3.3 Discussion of Variation in Measured Temperature

During a spark discharge, 15-25% of the initial energy is used to create the surrounding vapor plume and the initial shock wave. The remaining 75-85% is thermal energy that liquefies and vaporizes the electrode material. The specific heat capacity of liquid nitrogen and ethanol differ only slightly (cp,Nitrogen(L)=2.0 KJ/kg-K, cp,Ethanol=2.3 KJ/kg-K), though ethanol has a significantly higher latent heat of vaporization than liquid nitrogen ($\Delta H_{v,Nitrogen}$=199 KJ/kg, $\Delta H_{v,Ethanol}$=841 KJ/kg). Since H_2 gas is the predominant species released during ethanol decomposition, we will assume that that the H_2 gas dominates the thermal response of the ethanol plume. This assumption is also supported by the prominence of the H_α emission peak observed during spectroscopy. An estimation of the energy required to vaporize and heat the plumes can be calculated using the temperature dependent specific heat capacities of N_2 and H_2 gas along with the initial operating and boiling temperature of liquid nitrogen and ethanol ($T_{operate,Nitrogen(L)}$=70K, $T_{B,Nitrogen}$=77K, $T_{operate,Ethanol}$=295K, $T_{B,Ethanol}$=351K). More than 12 times the energy is required to vaporize and heat a 0.5mm radius spherical volume to 5500K in ethanol than liquid nitrogen. Given that we must also consider that ethanol was observed to have a smaller plume radius than liquid nitrogen at the same capacitance, vaporizing and heating a 0.35mm radius spherical volume of ethanol still requires approximately 9 times more energy than the aforementioned volume of liquid nitrogen. While this estimation is not representative of the complex thermal evolution accompanying the discharge, it illustrates that ethanol likely consumes a much higher portion of the initial energy to form the plume than liquid nitrogen. This presumption is supported by the observation of smaller plumes in ethanol discharges and consecutively larger plumes for discharges of increased capacitance. Thus, the remaining initial energy for liquefying and vaporizing the electrode surfaces will be significantly less in an ethanol discharge than a liquid nitrogen discharge of equal capacitance.

The difference in initial energy consumed during vapor plume formation may partially account for the difference in measured plasma hot-zone temperature. Considering the same 0.5mm and 0.35mm plume dimensions used in the previous estimations, roughly 65% of the difference in energy consumption can be explained by assuming the nitrogen plume reaches 12000K and the ethanol plume reaches 5500K. While the extent of increased plasma temperatures in liquid nitrogen discharges cannot be quantitatively confirmed by this study, the experimental findings strongly suggest that the liquid nitrogen discharges achieved higher temperatures than those in ethanol for the same capacitance. Future work is suggested with a dielectric fluid that is more conducive to Saha-Boltzmann temperature measurement. The influence of the dielectric fluid on the hot-zone temperature may prove to be a powerful means of controlling the extent and intensity of surface vaporization.

3.3.5 Discussion of Discharge Parameters on Nanoparticle Formation

Nanoparticle formation during spark erosion begins in the supersaturated metal vapor plume [18,40]. Groups of atoms, or clusters, form spherical particles within the plume. Many of these smaller clusters are unstable because the energy required to create its surface is greater than the energy released by forming its volume – ultimately leading to the dissolution of the particle back into the gas state. If a particle’s size is large enough that the volume energy released is greater than the surface energy cost, then the particle has surpassed the critical radius of nucleation and can become stable. Once stable, particles initially grow by diffusion and relieve the supersaturation of the gas. The early stages of nucleation and condensation primarily introduce small (<20nm) monodisperse particles into the system – and do not account for the larger (>50nm) particles [17,19,41]. Late-stage mechanisms (coagulation, coalescence, etc.) are responsible for the increasing and spreading particle size. Nevertheless, a discussion of nucleation and condensation is necessary to understand the complete evolution of vapor-to-nanoparticle.

Itina *et al.* [18] developed a model for supersaturation and critical radii in a uniform density vapor plume. Itina’s theoretical discussion of spark erosion particle formation accounted for the geometrically spherical and dynamic vapor environment created as a product of the submerged plasma discharge. Simulation of discharges under different spark energies demonstrated that increasing the initial energy increased the critical radii of nuclei. For every additional 100mJ, there was an approximate 1nm increase in the critical radius of stable nuclei. This was decidedly due to the strong dependence of the expansion conditions on the supersaturation degree. Raising the initial energy increased the erosion temperature, which understandably led to an increase in the amount of evaporated material in the plume and the cohesive energy threshold of formation. Additionally, since supersaturation was shown to be strongly dependent on the ratio of the plume size to its initial radius, as the plume rapidly expanded the degree of supersaturation coincidently increased and lowered the critical radius from 3nm to approach a lower limit of 2.5nm within 4µs of the discharge.

Luk’yanchuk *et al.* [41] performed a similar investigation of nuclei production in a supersaturated vapor using modified Zeldovich-Raizer theory to consider a more general inhomogeneous plume. Condensation in this model is driven by a saturation wave that propagates radially with the expansion of the plume. Condensation stops when the plume reaches a free-flight regime, also described as a disparate quenching wave moving radially through the system. The combined movement of the condensation and quenching waves describe varying nucleation time and conditions within the plume. It is shown that the number of clusters and size strongly depend on the velocity of the vapor expansion, which depends on the energy of the discharge, evaporated mass, and the initial size of the vapor. Luk'yanchuk *et al.* [41] demonstrates that by increasing initial energies, and therefore temperatures, at a fixed specific volume one would expect a decrease in cluster size. However, it is also shown that increasing the initial plume density at a fixed temperature increases cluster size. Luk'yanchuk *et al.* [41] notes that since an increase in the initial energy should also evaporate more surface energy and increase plume density – any significant variation in expected cluster size is negated. This example highlights the fact that physical interdependencies (temperature, density, velocity, pressure, etc.) within the plume are exceedingly complex and still not completely understood. This point is conceded by Luk'yanchuk *et al.* [41], who also emphasizes that further work is needed to solve the complete plume vapor condensation problem [41].

A recent investigation of metal vapor condensation by Kozadaev [19] addressed several of the shortcomings in the original Luk'yanchuk *et al.* [41] theory. The Taylor-Sedov expansion model is used to describe radial plume development due to its agreement with experimental data, whereas Luk'yanchuk's model significantly overestimates the radial expansion. Terms were also added to correct for boundary temperature, pressure, and density. Kozadaev [19] constructed a similar expression for the size of supercritical nuclei dependent on the degree of supersaturation, liquid phase density, the heat of vaporization, and atomic mass of the target material. Ultimately, the average cluster size was 2-4nm for simulation under standard experimental conditions and only varied with respect to the target material. However, to extend the model to explain experimental findings of high concentrations of >50nm particles Kozadaev [19] affirmed that it was no longer possible to attribute final particle size-effects to nuclei droplet growth, and nucleation mechanics were even neglected as insignificant in comparison to coalescence effects.

The gas-to-particle nucleation and condensation processes increase the particle mass concentration in the plume but have limited influence on the modification of the particle size distribution. Coalescence, the joining of two or more droplets, has a much more pronounced effect on the modal size distribution [17,19,40,42–46]. In the case of spark erosion, the collision of newly formed spherical clusters encourages rapid particle growth within the gaseous plume. Unlike condensation and nucleation, coalescence does not increase particle mass concentration in the system, but instead decreases the particle number concentration. The reduction in surface area that accompanies the coalescence process coincides with a decrease in Gibbs free energy and an increase in particle temperature. The reduction of free energy in coalescence may assist in complete coalescence and retention of the spherical form - as opposed to partial coalescence resulting in interparticle neck formation [44,45].

It is generally accepted that particle concentration, temperature, and coalescence time are several of the most influential factors for coalescence. Since coalescence requires random collisions between suspended particles, the quantity of particles available in the system understandably has a considerable influence. Smoluchowski coagulation theory is a form of statistical physics used to quantitatively described particle population balance with respect to clumping and coagulation growth over time – and has been successfully applied to similar scenarios of discharge particle formation [17,40,42,43]. According to Smoluchowski's theory, the rate of coalescence is proportional to the square of their number concentration [43]. Temperature is one of the most important factors of coalescence because of its dual effect on particle mobility and threshold particle temperature. A particle's mobility determines its probability of collision, or in other words, its average time between particle collisions [45]. Once the average time between collisions is longer than the time to cool the particle below the threshold coalescence temperature the coalescence process ends. Increased temperature therefore promotes coalescence by increasing particle mobility and transport in the system - quantitatively represented in Stokes-Einstein's expression of collisional frequency that scales proportionally with temperature ($\Omega \propto T$) [17]. Threshold temperature, in this context, is the minimum sufficiency particle temperature to completely fuse two particles into a single spherical particle [43,44]. Below the threshold temperature, particles will incompletely fuse or stick together in globules. For applications of nanoparticle fabrication, these non-specific globules are typically undesirable because size-dependent qualities may vary drastically in comparison to spherical particles of the same size.

Coalescence time is the total duration that particles retain the appropriate threshold temperature and collisional frequency to continue fusion and growth. Thus, coalescence time is primarily a function of cooling time, particle temperature, and number concentration – each of them required at a threshold level for further particle growth. Studies carefully considering reaction conditions have shown that longer coalescence times increase the particle size-average and variance, while still retaining the typical log-normal distribution [43–45]. However, it should be emphasized that these variables are also interconnected, and incremental increases or decreases may have incidental effects. This entanglement was demonstrated by Tabrizi *et al.,*[45] while conducting a study on particle formation under various spark discharge and background gas conditions. When increasing the background gas pressure, a higher breakdown voltage is reached, and therefore a higher temperature discharge is achieved. According to the basic coalescence description previously provided, this should lead to the production of larger particles. Instead, the increased cooling associated with the higher pressures more than compensated for the increased temperature spark and lead to smaller particles.

Spark discharge particle coalescence time is typically limited by cooling of particles through heat exchange with the heated background gas [17]. This has been confirmed by previous electron microscopy observation of large agglomerates of small solid primary particles, indicating that particles continue to collide after solidification [8,17]. Thus, the solidification of coalesced masses is dictated by the rate of heat transfer between the superheated gas and the particles. The thermal conductivity of gaseous N_2 is considerably lower than that of H_2 ($k_{Nitrogen}$=32.3 mW/m-K, $k_{Hydrogen}$=230.4 mW/m-K @ T=400K), suggesting that given equal initial temperatures the ethanol plume would cool the particles at a much faster rate than the nitrogen plume. A slower rate of cooling in the nitrogen plume could explain the difference in measured particle sizes – due to increased coalescence particle growth from increased coalescence times.

Significantly longer (+60μs) plume duration in liquid nitrogen than ethanol may also partially resolve the difference in the measured particle sizes between dielectrics. The increase in plume duration can be qualitatively correlated to an increase in coalescence time, and therefore, an increase in particle size. While observation of the plume itself cannot be correlated to a specific threshold temperature, we can assume that existence of the plume corresponds to endurance of a high-temperature gaseous region that could mediate coalescence. This assumption is also supported by the previous discussion on the possible difference in energy allocation in ethanol and liquid nitrogen discharges. Since considerably more energy may be required to create and sustain the ethanol plume, a lower hot-zone temperature is achieved, and the plume is more rapidly quenched. Conversely, discharges in liquid nitrogen can achieve a much higher temperature when provided the same initial energy, effectively lengthening the plume survival period and coalescence time, and increasing the particle size.

The relation of capacitance on the final particle size is believed to be the result of increased initial energy vaporizing more surface material and leading to higher hot-zone temperatures. Higher concentrations of metal within the plume increases the collision rate, and in turn, furthers the degree of coalescence and particle size. Increases in plume temperature enable the coagulating particles to retain the threshold temperature for longer. Here, increasing capacitance by an additional 20μF lead to a ~20μs increase in plume duration and, therefore, an increase in coalescence time. The concluding relation of capacitance and particle size also agrees with previous findings in gaseous spark discharge synthesis studies [44,45].

Since we are considering particles smaller than 100nm, it is also essential to discuss melting point depression effects [17]. The average cohesive energy of a particle decreases as the ratio of surface area to volume increases. This is due to surface atoms having a reduced number of stabilizing cohesive bonds. When the surface atoms become a larger fraction of the cluster, the effect becomes more pronounced, enabling small particle melting well below the bulk melting temperature. Small particles remain in the liquid state for longer and are therefore available for coalescence for a lengthened duration [17]. Melting point depression is believed to affect both liquid nitrogen and ethanol discharges equivalently and, as a result, would uniformly inflate modal size and deviation.

A more recently proposed form of coalescence is described in Kozadaev [19]. As the plume expands into the medium, the leading edge quickly reaches a point of ‘deceleration’ when its propagation is resisted. Since clusters move outward with the expansion of the vapor, the inner nuclei ‘dash’ or collide against the peripheral clusters as they slow. Colliding particles coalesce to form larger particles that are in turn solidified by the same means previously discussed. The model used by Kozadaev [19] describes coalescence growth dynamics as a function of the difference of pressures inside and outside the plume. The proposed model had good correspondence with experimental data for a range of materials (Pb, Zn, Ni, Cu, Ag, Au, Pt) [19]. However, there is limited understanding of the combined empirical effects of collision-frequency coalescence and propagation front-braking coalescence. Differentiation between particles formed through braking collisions and particles formed through frequency collisions may be near impossible, so the exact interplay of these processes is not yet understood. There is also the possibility that one of the processes dominates the other in terms of mass concentration, rendering the other's effects insignificant. For this study, the influence of braking-collision coalescence will be ignored because the phenomena is not as well understood as Smoluchowski coalescence. Further work is required to discriminate between these mechanisms.

Suspended particles can also significantly affect fundamental plasma behavior. Investigation of so called, "dusty" plasmas has grown to be an exciting subset of plasma physics due complex and unexpected phenomena that occur when small micron-sized, or smaller, charged particles are present [26–29,47]. Initial interest in dusty plasmas originated from studying cosmic environments and planetary/dust rings, however, modern applications of processing plasmas in the semiconductor industry also have a heightened interest in understanding how particulates modify interspecies plasma interactions [26,29]. Charged nanoparticles are also observed as byproducts of arc-driven particle fabrication methods as demonstrated by Anders *et al.* [48,49] and Tabrizi *et al.* [45]. Massive particles tend to tend to acquire a negative charge of several hundred to several thousand electron charges through collision with more rapidly moving electrons. Additional charging is possible through collisions with ions, photoelectron emission, secondary electron emission, and thermionic emission [26,29]. The interaction of these charged particles can have complex, and sometimes unforeseen, consequences on the evolution and equilibrium state of the plasma. If the attractive strength of the charge is comparable, or larger, than the kinetic energy of the individual particles then inter-particle interaction can lead to the formation of self-organized coulomb lattices [26,27,47]. Additionally, if two dust particles carry the same charge they can repel each other and reduce the cross-sectional area of collision [27]. The culmination of these interactions leads exceedingly complex collective particle systems in which multiparticle interaction potentials and shielding are often non-linear [26]. For the application of spark discharge particle formation, non-homogenous particle sizes further obfuscates the mechanics because the initial particle size influences the collisional cross section, which partially determines the total amount of electron charge accumulated per particle. The dynamic expansion of the plume is also a concern because its influence on interparticle separation. The coulomb coupling parameter is proportional to $\Gamma \propto Q^2/dT_d$ where Q is the number of charges on the dust surface, d is the interparticle separation, and T_d is the dust temperature [26]. When $\Gamma \leq 1$ dust particles can be considered weakly coupled, however, when $\Gamma \gg 1$ the charged particles strongly interaction and can form coulomb lattices. It is possible that coulomb self-assembly may play a role in nanoparticle growth, though there is still a limited understanding in the relationship between these attractive forces and the discharge mechanisms. Modification of interparticle attraction potentials could readily affect collision frequency and coalescence. However, there is no trivial solution - extensive knowledge of plasma physics, statistical mechanics, solid state physics, and condensed matter physics is need to fully encapsulate the collective effects of the charged-particle plasmas. Active efforts continue to search for solutions to unresolved issues in dusty plasma physics, and as such, our understanding of spark erosion will similarly mature as researchers fill in the gaps.

3.4 Conclusion

This study investigated the dynamics of submerged Fe capacitive discharge using high-speed imaging and optical emission spectroscopy. High-speed imaging revealed that liquid nitrogen dielectric produced a larger plume that existed for 60-120μs longer than those in ethanol. The shock wave in liquid nitrogen evolved at a faster rate than in ethanol, which was correlated to a higher boundary pressure. Higher capacitance levels increased the rate and duration of the shock front. Optical emission spectroscopy illustrated that increasing capacitance increased the plume temperature. Direct comparison of liquid nitrogen and ethanol plume temperatures was inconclusive – though it is likely that ethanol plume temperatures are reduced due to significant energetic consumption during plume generation. Coalescence of nucleated clusters was decidedly the most important mechanism for increasing the modal particle size and variance. Increased plume temperature, vapor density, and duration with increasing capacitance can be appropriately correlated to a higher degree of coalescence in both liquid nitrogen and ethanol. The significant increase in plume duration (and possibly temperature) during liquid nitrogen discharges suggests a higher degree of coalescence that would also explain the noticeable increases in particle size and deviation when compared to ethanol discharges of equal capacitance.

3.5 Acknowledgements

Part 3, in part is currently being prepared for submission for publication of the material. McElfresh, Cameron; Mellor, William, Thakur, Saikat; Kaufmann, Kevin; Harrington, Tyler; Elliason, Veronica; Tynan, George; Vecchio, Kenneth. The thesis author was the primary investigator and author of this material.

K. Kaufmann was supported by the Department of Defense (DoD) through the National Defense Science & Engineering Graduate Fellowship (NDSEG) Program. Special thanks to

Daisuke Nishijima and other members of George Tynan’s Plasma Physics group for helpful discussion throughout this project.

3.6 References

[1] Z. Lee, V. Radmilovic, B. Ahn, E.J. Lavernia, S.R. Nutt, Tensile Deformation and Fracture Mechanism of Bulk Bimodal Ultrafine-Grained Al-Mg Alloy, Metall. Mater. Trans. A. **41** (2010) 795–801. doi:10.1007/s11661-009-0007-y.

[2] B.O. Han, E.J. Lavernia, Z. Lee, S. Nutt, D. Witkin, Deformation behavior of bimodal nanostructured 5083 Al alloys, Metall. Mater. Trans. A. **36** (2005) 957–965. doi:10.1007/s11661-005-0289-7.

[3] D. Witkin, Z. Lee, R. Rodriguez, S. Nutt, E. Lavernia, Al–Mg alloy engineered with bimodal grain size for high strength and increased ductility, Scr. Mater. **49** (2003) 297–302. doi:10.1016/S1359-6462(03)00283-5.

[4] V.A. Skripnyak, E.G. Skripnyak, N. V. Skripnyak, Mechanical Behavior of Light Alloys with Bimodal Grain Size Distribution, Appl. Mech. Mater. **756** (2015) 205–213. doi:10.4028/www.scientific.net/AMM.756.205.

[5] J.P. Fortin, C. Wilhelm, J. Servais, C. Ménager, J.C. Bacri, F. Gazeau, Size-sorted anionic iron oxide nanomagnets as colloidal mediators for magnetic hyperthermia, J. Am. Chem. Soc. **129** (2007) 2628–2635. doi:10.1021/ja067457e.

[6] S. Laurent, S. Dutz, U.O. Häfeli, M. Mahmoudi, Magnetic fluid hyperthermia: Focus on superparamagnetic iron oxide nanoparticles, Adv. Colloid Interface Sci. **166** (2011) 8–23. doi:10.1016/j.cis.2011.04.003.

[7] M. Gonzales-Weimuller, M. Zeisberger, K.M. Krishnan, Size-dependant heating rates of iron oxide nanoparticles for magnetic fluid hyperthermia, J. Magn. Magn. Mater. **321** (2009) 1947–1950. doi:10.1016/j.jmmm.2008.12.017.

[8] T. Harrington, C. McElfresh, K. Vecchio, Spark Erosion as a High-throughput Method for Producing Bimodal Nanostructured 316L Stainless Steel Powder, Powder Technol. **328** (2018) 156-166. doi: 10.1016/j.powtec.2018.01.012.

[9] J. Carrey, H.B. Radousky, A.E. Berkowitz, Spark-eroded particles: Influence of processing parameters, J. Appl. Phys. **95** (2004) 823–829. doi:10.1063/1.1635973.

[10] A.E. Berkowitz, H. Harper, D.J. Smith, H. Hu, Q. Jiang, V.C. Solomon, H.B. Radousky, Hollow metallic microspheres produced by spark erosion, Appl. Phys. Lett. **85** (2004) 940–942. doi:10.1063/1.1779962.

[11] M.S. Hsu, M.A. Meyers, A.E. Berkowitz, Synthesis of nanocrystalline titanium carbide by

spark erosion, Scr. Metall. Mater. **32** (1995) 805–808. doi:10.1016/0956-716X(95)93205-I.

[12] V.S. Burakov, A.V. Butsen, V. Bruser, F. Harnisch, P.Y. Misakov, E.A. Nevar, M. Rosenbaum, N.A. Savastenko, N.V. Tarasenko, Synthesis of tungsten carbide nanopowder via submerged discharge method, **10** (2008) 881–886. doi:10.1007/s11051-007-9314-7.

[13] C. McElfresh, T. Harrington, K.S. Vecchio, Application of a novel new multispectral nanoparticle tracking technique, Meas. Sci. Technol. **29** (2018) 065002. doi:10.1088/1361-6501/aab940.

[14] J. Carrey, H.B. Radousky, A.E. Berkowitz, Spark-eroded particles: Influence of processing parameters, J. Appl. Phys. **95** (2004) 823–829. doi:10.1063/1.1635973.

[15] A.E. Berkowitz, M.. Hansen, F. Parker, K.S. Vecchio, F.. Spada, E.J. Lavernia, R. Rodriguez, Amorphous soft magnetic particles produced by spark erosion, J. Magn. Magn. Mater. **254** (2003) 1–6. doi:10.1016/S0304-8853(02)00932-0.

[16] T.A. Schmitz, J. Koch, D. Günther, R. Zenobi, J. Koch, D. Gu, Ablation of different matrix-assisted laser ablation matrices Early plume and shock wave dynamics in atmospheric-pressure ultraviolet-laser ablation of different matrix-assisted laser ablation matrices, **109** (2012) 123106. doi:10.1063/1.3592651.

[17] R. Hergenröder, A model for the generation of small particles in laser ablation ICP-MS, J. Anal. At. Spectrom. **21** (2006) 1016–1026. doi:10.1039/B604453K.

[18] T.E. Itina, A. Voloshko, Nanoparticle formation by laser ablation in air and by spark discharges at atmospheric pressure, **113** (2013) 473–478. doi:10.1007/s00340-013-5490-6.

[19] K.V. Kozadaev, Condensation of ablation plumes in the irradiation of metals by high-intensity nanosecond laser pulses at atmospheric pressure Condensation of ablation plumes in the irradiation of metals by high-intensity nanosecond laser pulses at atmospheric pressure, **46** (2016) 16-22. doi:10.1070/QE2016v046n01ABEH015801.

[20] A. Kohut, G. Galbács, Z. Márton, Z. Geretovszky, Characterization of a copper spark discharge plasma in argon atmosphere used for nanoparticle generation, Plasma Sources Sci. Technol. **26** (2017) 045001. doi:10.1088/1361-6596/aa5c2b.

[21] V.K. Unnikrishnan, K. Alti, V.B. Kartha, C. Santhosh, Measurements of plasma temperature and electron density in laser-induced copper plasma by time-resolved spectroscopy, Pramana-J Phys. **74** (2010) 983–993.

[22] C.A. Bye, A. Scheeline, Saha-Boltzmann Statistics for Determination of Electron Temperature and Density in Spark Discharges Using an Echelle / CCD System, Appl. Spectrosc. **47** (1993) 2022-2030.

[23] P. Bruggeman, T. Verreycken, M.Á. González, J.L. Walsh, M.G. Kong, C. Leys, D.C. Schram, Optical emission spectroscopy as a diagnostic for plasmas in liquids: Opportunities and pitfalls, J. Phys. D. Appl. Phys. **43** (2010) 124005. doi:10.1088/0022-3727/43/12/124005.

[24] S.H. Khezri, A. Yazdani, R. Khordad, Pure iron nanoparticles prepared by electric arc discharge method in ethylene glycol, Eur. Phys. J. Appl. Phys. **59** (2012) 30401. doi:10.1051/epjap/2012110303.

[25] S. Karatodorov, V. Mihailov, T. Křenek, M. Grozeva, Optical emission spectroscopy of plasma produced by laser ablation of iron sulfide, J. Phys. Conf. Ser. **700** (2016) 012001. doi:10.1088/1742-6596/700/1/012001.

[26] P.K. Shukla, A survey of dusty plasma physics, Phys. Plasmas. **8** (2001) 1791. doi:10.1063/1.1343087.

[27] C.K. Goertz, Dusty Plasmas in the Solar System, Rev. Geophys. **27** (1989) 271–292.

[28] M. Lampe, G. Joyce, G. Ganguli, V. Gavrishchaka, Interactions between dust grains in a dusty plasma, Phys. Plasmas. **7** (2000) 3851. doi:10.1063/1.1288910.

[29] R.L. Merlino, A. Barkan, C. Thompson, N. D'Angelo, Laboratory studies of waves and instabilities in dusty plasmas, Phys. Plasmas. **5** (1998) 1607–1614. doi:10.1063/1.872828.

[30] J. Bauchire, S. Assarzadeh, M. Ghoreishi, Optical emission spectroscopy of electrical, J. Phys. D: Appl. Phys. **37** (2004) 875. doi:10.1088/0022-3727/37/6/012.

[31] V.S. Burakov, A.V. Busten, N.V. Tarasenko, Laser-Induced Plasmas in Liquids for Nanoparticle Synthesis, Appl. Spectrosc. **77** (2010) 386–393.

[32] P. Muthakarn, N. Sano, T. Charinpanitkul, W. Tanthapanichakoon, T. Kanki, Characteristics of carbon nanoparticles synthesized by a submerged arc in alcohols, alkanes, and aromatics, J. Phys. Chem. B. **110** (2006) 18299–18306. doi:10.1021/jp063443j.

[33] J.-C. Fan, H.-H. Sung, C.-R. Lin, M.-H. Lai, The production of onion-like carbon nanoparticles by heating carbon in a liquid alcohol, J. Mater. Chem. **22** (2012) 9794. doi:10.1039/c2jm13273g.

[34] O. Albert, S. Roger, Y. Glinec, J.C. Loulergue, J. Etchepare, C. Boulmer-Leborgne, J. Perrière, E. Millon, Time-resolved spectroscopy measurements of a titanium plasma induced by nanosecond and femtosecond lasers, Appl. Phys. A Mater. Sci. Process. **76** (2003) 319–323. doi:10.1007/s00339-002-1815-8.

[35] P.G. Reyes, A. Gómez, H. Martínez, O. Flores, C. Torres, J. Vergara, Characterization of Ethanol Plasma Glow Discharge , Decomposition in Several Species and Solid Film

Formation, IEEE T Plasma Sci. **44** (2016) 2995–3000. doi:10.1109/TPS.2016.2628639.

[36] J. Ramkumar, N. Glumac, S.G. Kapoor, R.E. Devor, Characterization of plasma in micro-EDM discharge using optical spectroscopy, J. Manuf. Process. **11** (2009) 82–87. doi:10.1016/j.jmapro.2009.10.002.

[37] B. Verhoff, S.S. Harilal, J.R. Freeman, P.K. Diwakar, A. Hassanein, Dynamics of femto- and nanosecond laser ablation plumes investigated using optical emission spectroscopy, J. Appl. Phys. **112** (2012) 093303. doi:10.1063/1.4764060.

[38] L.D. Swafford, D.M. Surmick, M.J. Witte, A.C. Woods, G. Gautam, C.G. Parigger, Hydrogen Balmer series measurements in laser-induced air plasma, J. Phys. Conf. Ser. **548** (2014) 012049. doi:10.1088/1742-6596/548/1/012049.

[39] A. Descoeudres, C. Hollenstein, G. Wälder, R. Perez, Time-resolved imaging and spatially-resolved spectroscopy of electrical discharge machining plasma, J. Phys. D. Appl. Phys. **38** (2005) 4066–4073. doi:10.1088/0022-3727/38/22/009.

[40] T.E. Itina, Modeling nanoparticle formation by laser ablation and by spark discharges, Proc SPIE Int Soc Opt Eng. **973704** (2018). doi:10.1117/12.2216236.

[41] B.S. Luk, W. Marine, S.I. Anisimov, Condensation of Vapor and Nanoclusters Formation within the Vapor Plume , Produced by ns-Laser Ablation of Si, Laser Phys. **8** (1998) 291–302.

[42] M. Ullmann, S.K. Friedlander, A. Schmidt-ott, Nanoparticle formation by laser ablation, J. Nanopart. Res. **4** (2002) 499–509.

[43] J. Feng, G. Biskos, A. Schmidt-Ott, Toward industrial scale synthesis of ultrapure singlet nanoparticles with controllable sizes in a continuous gas-phase process, Sci. Rep. **5** (2015) 1–9. doi:10.1038/srep15788.

[44] B.O. Meuller, M.E. Messing, D.L.J. Engberg, A.M. Jansson, L.I.M. Johansson, S.M. Norlén, N. Tureson, K. Deppert, Review of spark discharge generators for production of nanoparticle aerosols, Aerosol Sci. Technol. **46** (2012) 1256–1270. doi:10.1080/02786826.2012.705448.

[45] N.S. Tabrizi, M. Ullmann, V.A. Vons, U. Lafont, A. Schmidt-Ott, Generation of nanoparticles by spark discharge, J. Nanoparticle Res. **11** (2009) 315–332. doi:10.1007/s11051-008-9407-y.

[46] W. Zhang, A. Farooq, W. Wang, Generating Silicon Nanoparticles Using Spark Erosion by Flushing High-Pressure Deionized Water, Mater. Manuf. Process. **31** (2016) 113–118. doi:10.1080/10426914.2014.984199.

[47] H. Ikezi, Coulomb solid of small particles in plasmas, Phys. Fluids. **29** (1986) 1764.

doi:10.1063/1.865653.

[48] O.R. Monteiro, Vacuum-arc-generated macroparticles in the nanometer range, IEEE Trans. Plasma Sci. **27** (1999) 1030–1033. doi:10.1109/27.782276.

[49] A. Anders, Approaches to rid cathodic arc plasma of macro and nanoparticles-a review.pdf, Surf. Coatings Technol. **121** (1999) 319–330. http://www.sciencedirect.com/science/article/pii/S0257897299004600.